

Stellar Populations in the Central 0.5 pc of Our Galaxy III: The Dynamical Sub-structures

SIYAO JIA,¹ NINGYUAN XU,¹ JESSICA R. LU,¹ D.S. CHU,² K. KOSMO O'NEIL,² W.B. DRECHSLER,¹
M. W. HOSEK JR.,^{2,*} S. SAKAI,² T. DO,² A. CIURLO,² A. K. GAUTAM,² A. M. GHEZ,² E. BECKLIN,² M. R. MORRIS,²
AND R. O. BENTLEY²

¹*Astronomy Department, University of California, Berkeley, CA 94720, USA*

²*UCLA Department of Physics and Astronomy, Los Angeles, CA 90095-1547, USA*

ABSTRACT

We measure the 3D kinematic structures of the young stars within the central 0.5 parsec of our Galactic Center using the 10 m telescopes of the W. M. Keck Observatory over a time span of 25 years. Using high-precision measurements of positions on the sky, and proper motions and radial velocities from new observations and the literature, we constrain the orbital parameters for each young star. Our results show two statistically significant sub-structures: a clockwise stellar disk with 18 candidate stars, as has been proposed before, but with an improved disk membership; a second, almost edge-on plane of 10 candidate stars oriented East-West on the sky that includes at least one IRS 13 star. We estimate the eccentricity distribution of each sub-structure and find that the clockwise disk has $\langle e \rangle = 0.39$ and the edge-on plane has $\langle e \rangle = 0.68$. We also perform simulations of each disk/plane with incompleteness and spatially-variable extinction to search for asymmetry. Our results show that the clockwise stellar disk is consistent with a uniform azimuthal distribution within the disk. The edge-on plane has an asymmetry that cannot be explained by variable extinction or incompleteness in the field. The orientation, asymmetric stellar distribution, and high eccentricity of the edge-on plane members suggest that this structure may be a stream associated with the IRS 13 group. The complex dynamical structure of the young nuclear cluster indicates that the star formation process involved complex gas structures and dynamics and is inconsistent with a single massive gaseous disk.

Keywords: astrometry - Galaxy: center - infrared: stars - techniques: high angular resolution

1. INTRODUCTION

Nuclear Star Clusters (NSCs) and Supermassive Black Holes (SMBHs) are found to coexist within the central parsec (pc) of many different types of galaxies (Graham & Spitler 2009). Furthermore, there are clear indications that NSCs, SMBHs, and their host galaxies evolve together. For example, Ferrarese et al. (2006) found that the $M-\sigma$ relationship, the empirical correlation between the mass of the SMBH, M , and the stellar velocity dispersion σ of the galaxy's bulge, applies both for SMBHs and NSCs with similar slopes, although at a certain σ , NSCs are 10 times more massive than SMBHs. Addi-

tionally, Kormendy & Ho (2013) showed that the combined mass of the SMBH and NSC scales with a galaxy's bulge mass with much less scatter than either the SMBH or the NSC separately, which suggests a strong dependency between their mutual formation and growth. The formation mechanism for NSCs is still widely debated as the strong tidal force at the Galactic Center will disrupt normal star formation.

Our own Galactic Center provides a unique test bed for understanding star formation around SMBHs since it harbors a population of around 200 young massive stars within 0.5 pc of the central SMBH, SgrA* (Genzel et al. 2000), including OB main-sequence stars, Wolf-Rayet (WR) stars, giants, and supergiants (Paumard et al. 2006; Bartko et al. 2010). Because the age of this population (3 - 8 Myr Lu et al. 2013) is much less than the relaxation timescale in the Galactic Center ($\gtrsim 1$ Gyr, Hopman & Alexander (2006)), the origin of these stars can be constrained through studies of their dynamical

Corresponding author: Jessica Lu
jlu.astro@berkeley.edu

Corresponding author: Ningyuan Xu
alexny0337@berkeley.edu

* Brinson Prize Fellow

structures. Only in the Galactic Center can we resolve individual stars and measure their motion, photometry, and spectroscopy with sufficient precision to constrain their dynamics and therefore constrain theories of star formation around SMBHs.

Observations of young stars at the Galactic Center currently favor *in situ* formation models, meaning that young stars are formed roughly where we see them today, within 0.5 pc of the SMBH (Paumard et al. 2006; Lu et al. 2009; Støstad et al. 2015). *In situ* formation is theoretically possible in an accretion disk around the SMBH, if it is massive enough to collapse vertically under its own self-gravity (Kolykhalov & Syunyaev 1980; Morris & Serabyn 1996; Sanders 1998; Goodman 2003; Levin & Beloborodov 2003; Nayakshin & Sunyaev 2005). When a disk reaches a surface density that is just large enough to initiate star formation, the first protostars form. Feedback from those stars will then heat the disk up to a point where it stabilizes against collapse and shuts off further disk fragmentation. In the meantime, those stars remain embedded in the disk and continue gaining mass at very high rates. As a result, an average star created in such a disk may become very massive. This process happens throughout the disk, from ~ 0.01 pc to a few parsecs, with a peak effect at $R \sim 0.1$ pc (Morris & Serabyn 1996; Vollmer & Duschl 2001; Nayakshin & Sunyaev 2005; Nayakshin 2006). This scenario can explain the existence of the disk of stars and the top-heavy Initial Mass Function (IMF) in our Galactic Center (Lu et al. 2013), although it may not be the only explanation.

However, if the disk is formed through steady accretion of gas, stars with circular orbits are more likely to form, which may contradict the observed eccentricity distribution that peaks at $e=0.27$ (Yelda et al. 2014). Furthermore, only 20% of the young stars are estimated to be in the disk and it is not clear whether 80% of the stars could be scattered from the disk in only 4 - 8 Myr. Modified *in situ* formation scenarios have been proposed, including: (a) the initial gas is not uniformly distributed, (b) stars form in repeated episodes, (c) after the gas disk collapses, the stars that form in it dynamically evolve off the disk. These formation scenarios can be disentangled by comparing the dynamical structures among different dynamical sub-groups. For example, if the initial gas is not uniformly distributed, we should see asymmetric sub-structures in their stellar systems.

Previous studies show that the young stars at the Galactic Center can be divided into three dynamical groups: (1) $\sim 12\%$ of the young stars (within 0.03 pc) are in the innermost region with high eccentricities $\bar{e} = 0.8$ and randomly oriented orbits. (2) $\sim 20\%$

of the young stars are on a well-defined clockwise (CW) rotating disk (0.03 - 0.5 pc) with moderate eccentricities $\bar{e} = 0.3$. (3) $\sim 68\%$ of them are off-disk stars that extend over the same radius but have a more random distribution and eccentricity distribution with higher $\bar{e} = 0.6$ (Lu et al. 2013; Yelda et al. 2014). At smaller radii, dynamical effects will randomize the stellar orbits within 4-6 Myr, which is the case for the first group. The existence of the CW disk has already been verified to be significant ($\sim 20\sigma$) (Paumard et al. 2006; Bartko et al. 2010; Lu et al. 2009; Yelda et al. 2014). More recently, as many as 5 distinct sub-structures, including the CW disk, have been proposed by von Fellenberg et al. (2022). A detailed comparison between our result and previous work is presented in §6.1 and Appendix B.

In this paper, we present improved dynamical measurements of the young stars at the Galactic Center derived from adaptive optics observations from the 10m Keck telescopes. We conduct novel simulations and comparative analyses of the properties of the different dynamical sub-groups of young stars within the central 0.5 pc of our Galaxy. The observational setup and data reduction are presented in Section 2. Orbital parameters are derived in §3 and the disk membership analysis is shown in §4. Results of stellar disk properties and cluster simulations are presented in §5. We discuss our findings in §6 and summarize in §7.

2. OBSERVATIONS AND DATA REDUCTION

The kinematic analysis of the young stars at the Galactic Center requires both proper motion and radial velocity (RV) measurements in order to determine their orbital planes and disk membership probability. Details of the observations, data reduction, and image analysis are presented in Jia et al. (2019) and Do et al. (2009). Here, we briefly summarize the analysis methods most relevant to this work.

The photometry for those young stars is extracted from a deep, wide mosaic image (Lu et al. 2013). We applied the full extinction map from Schödel et al. (2010) to correct extinction with an average value of $A_{k_s} = 2.7$.

2.1. Sample Selection

In this work, we included all spectroscopically identified young (early-type) stars with well measured radial velocities (RV) and proper motions. To get a young star list with well-understood completeness, we combined new Galactic Center OSIRIS Wide-field Survey (GCOWS) observations (§2.2) with previous GCOWS observations (Do et al. 2013) and with other spectral types from the literature.

The GCOWS survey consists of observations with the Keck OSIRIS spectrograph behind the laser-guide-star

adaptive optics system on the W. M. Keck Observatory (Larkin et al. 2006). We obtained diffraction-limited, medium spectral-resolution ($R \sim 4000$) spectra with the Kn3 filter (2.121-2.220 μm). We used two different plate scales: 35 mas in the central fields where the stellar densities are highest and 50 mas for the outer fields having relatively lower stellar density. Details on the GCOWS survey are presented by Do et al. (2009) and Do et al. (2013), who investigated young stars located in the central region and eastern field in the GC (green boxes in Figure 1). In this work, we have added new observations in the South and North (magenta boxes in Figure 1). The new spectroscopic observations are reported in Table 1. Data were reduced using the latest version of the OSIRIS data reduction pipeline (Lyke et al. 2017; Lockhart et al. 2019). This resulted in 7 more young stars with good quality RVs: S10-261, S10-48, S11-176, S11-21, S11-246, S12-76, S5-106 (see §2.2 for reduction details). The sample of GCOWS stars used in this work includes those that are spectroscopically identified as early-type and that have sufficient Signal-to-Noise ratio (SNR) to measure a radial velocity (RV).

Then, we combined our list of young stars with those identified by Paumard, Bartko, and Feldmeier (Paumard et al. 2006; Bartko et al. 2009; Feldmeier-Krause et al. 2015). S2-66 was claimed to be young by Paumard et al. (2006), but later proven to be old by Do et al. (2009), so this star was excluded. From all the sources combined, the sample consisted of RVs for 149 young stars. Unfortunately, Paumard et al. (2006) and Bartko et al. (2009) did not report their spectral completeness curve, so we cannot use stars that are found only in their paper. This is because we require spectroscopic completeness information for each star, which is crucial in §5.3 when comparing observed and simulated stellar distributions. However, we can still use their RV for stars that are identified in GCOWS or Feldmeier-Krause et al. (2015), which leaves us 91 stars with both RV and completeness correction curves.

Among those stars, we are able to extract proper motion for 88 stars from a combination of Keck AO observations in the inner region and HST observations in the outer region (see §2.4 for details). The spatial distribution of our young star sample is plotted in Figure 1. Although seven new young stars were identified from the new GCOWS observations, S10-261 does not have a measured proper motion, so only six new stars are included in our sample, as shown in Figure 1. In summary, we have 88 young stars in our sample, extending out to $14''$ (~ 0.5 pc), down to a 90% limiting magnitude of $K_{\text{lim}} = 15.3$.

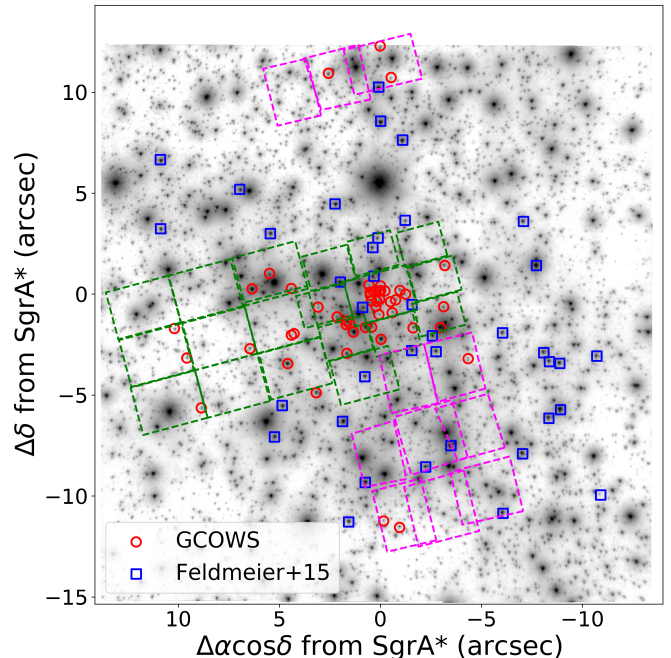


Figure 1. The spatial distribution of our final sample of 88 stars. Red circles are the 50 stars from our GCOWS observations and blue squares are the 38 stars from Feldmeier-Krause et al. (2015). The dashed lines show our GCOWS sky coverage, where the green boxes are fields previously published by Do et al. (2013) and magenta boxes are new areas first published in this paper.

2.2. Radial Velocities

As mentioned in §2.1, RVs used in this work come from two sources: (1) Our GCOWS survey from Keck observations (Do et al. 2009, 2013), and (2) other published RV data for Galactic Center, including Paumard et al. (2006), Bartko et al. (2009), Feldmeier-Krause et al. (2015) and Zhu et al. (2020).

We derive radial velocities for all Keck OSIRIS data (both previously reported and new) using full spectral fitting with a synthetic spectral grid. We use the spectral fitting code StarKit (Kerzendorf & Do 2015) to fit the radial velocity along with physical properties such as effective temperature, surface gravity, metallicity, and rotational velocity. By fitting the physical parameters simultaneously, we can capture the effect of correlations between the parameters. We use the BOSZ spectral grid (Bohlin et al. 2017) to generate the spectra for our Bayesian inference model. Additional discussion of this method is given by Do et al. (2018, 2019). In general, the statistical uncertainties dominate the radial velocity measurement, but for the brightest sources, the systematic uncertainties dominate at the level of about 11 km s^{-1} mainly due to residuals from the OH line subtrac-

Table 1. Summary of New Keck OSIRIS Observations

Field Name	Field Center ^a	Date	$N_{\text{frames}} \times t_{\text{int}}$	Scale	FWHM ^b	Filter	PA
	(")	(UT)	(s)	(mas)	(mas)		(°)
N5-3	-0.37,11.21	2013-05-17	3×900	50	75	Kn3	285
S4-1	-0.87,-11.03	2014-05-20	6×900	50	90	Kn3	195
S4-2	-3.19,-10.41	2014-05-20	8×900	50	89	Kn3	195
S4-3	-5.50,-9.79	2014-06-05	9×900	50	140	Kn3	195
S3-2	-2.35,-7.31	2014-07-18	6×900	50	94	Kn3	195
N5-1	4.40,9.93	2016-07-21	5×900	50	77	Kn3	195
N5-1	4.40,9.93	2016-07-22	3×900	50	61	Kn3	195
N5-2	2.01,10.58	2016-07-22	5×900	50	98	Kn3	195
S2-3	-3.80,-3.59	2019-05-25	5×900	50	89	Kn3	195
S2-2	-1.49,-4.21	2019-05-27	5×900	50	103	Kn3	195
S3-1	-0.03,-7.95	2019-05-27	2×900	50	135	Kn3	195
S3-1	-0.03,-7.95	2019-07-08	3×900	50	145	Kn3	195
S3-3	-4.66,-6.67	2019-07-08	4×900	50	133	Kn3	195

^aR.A. and decl. offset from Sgr A* (R.A. offset is positive to the east).

^bAverage FWHM of a relatively isolated star for the night, found from a two-dimensional Gaussian fit to the source.

tion. See [Do et al. \(2019\)](#) for a complete discussion of radial velocity systematic uncertainties.

Both [Paumard et al. \(2006\)](#) and [Bartko et al. \(2009\)](#) used the AO-assisted, near-infrared integral field spectrometer SPIFFI/SINFONI on ESO VLT. Since [Bartko et al. \(2009\)](#) is claimed to have improved measurements relative to [Paumard et al. \(2006\)](#), we will always adopt the RV from [Bartko et al. \(2009\)](#) if the reported RVs¹ are different between the two papers. [Feldmeier-Krause et al. \(2015\)](#) used the integral-field spectrograph, KMOS, on VLT. For IRS 13E2, IRS 13E3 and IRS 13E4, [Zhu et al. \(2020\)](#) report the latest RVs with smaller uncertainties, so we adopt their measurements for those three stars.

We match the catalogs from the literature with starlists from our high-resolution images based on stars' magnitudes and positions. However, due to different spatial resolutions between our observations and other published observations, not all stars can be matched. For example, star 3308 from [Feldmeier-Krause et al. \(2015\)](#) is matched to a clump of 3 stars in our image, and it is difficult to determine which one produces the RV signal they report. All RVs that are successfully matched to our catalogs are reported in Table 7.

¹ We assume stars are not in binary systems.

For stars detected in GCOWS, we always use the GCOWS RV measurements. Most stars have only one detection, which is adopted as their final RV measurement. Some stars in the central region have multiple detections, which are marked with asterisks in Table 7. For those multiple-detection stars, we will use the weighted mean RV if they are detected less than 5 times or show no significant physical acceleration. However if stars show significant acceleration in either proper motion or RV (S0-1, S0-2, S0-3, S0-4, S0-5, S0-8, S0-16, S0-19, S0-20, see details in [Chu et al. in prep](#)), they will be fit with a full Keplerian orbit in §3.2.

For stars not detected in our GCOWS database, we use their literature RVs. For stars reported multiple times in the literature, we use the weighted mean RV, where the weight, w , is:

$$w = \frac{1}{\sigma_{\text{RV}}^2} \quad (1)$$

All stars with RVs from the literature agree with each other within 2 sigma, except S7-236, for which we adopt the most recent RV from [Feldmeier-Krause et al. \(2015\)](#).

2.3. Spectroscopic Completeness

In order to properly correct for incompleteness in our selection sample, we utilize results from star-planting simulations. The sample was selected from two sources: [Feldmeier-Krause et al. \(2015\)](#) and GCOWS, and we describe the completeness for each below.

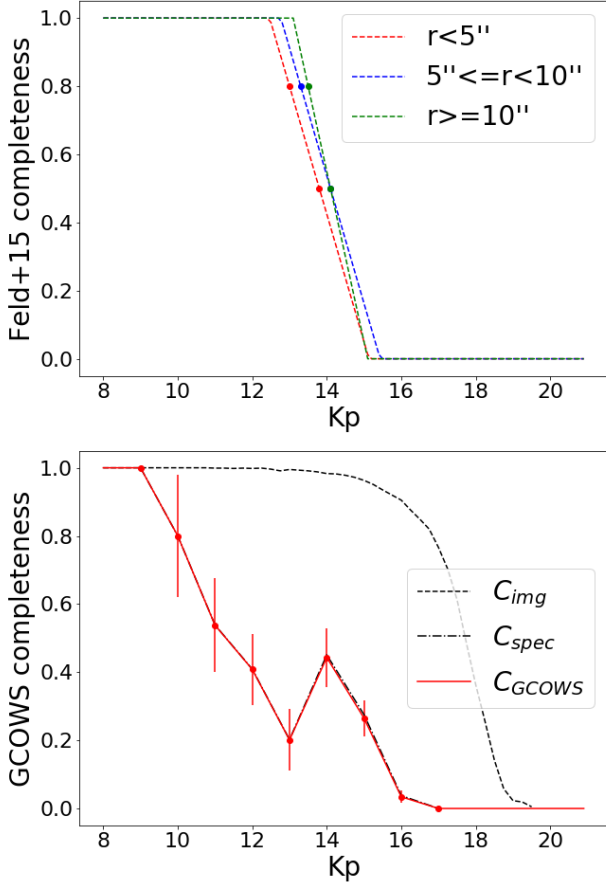


Figure 2. Completeness curve as a function of magnitude K_p for data from Feldmeier-Krause et al. (2015) (top) and for our data (bottom). Completeness for Feldmeier-Krause et al. (2015) is a linear interpolation from the 80% completeness and 50% completeness point they reported in their paper. Completeness also depends on radius; inner regions are less complete because of crowding. Completeness from our observations (red line) is a product of imaging completeness and spectral completeness, but is mostly determined by spectral completeness. The dip in $K_p = 13$ is probably a result of the fact that stars are transitioning to main sequence at that stage, so most spectra we get in that magnitude bin are featureless and are without usable RV.

For stars in the GCOWS observations, the completeness C is a product of imaging completeness, C_{img} , and spectral completeness, C_{spec} . Imaging completeness is estimated using star-planting simulations (see details in Appendix C.1 of Do et al. (2013)), and is 90% complete down to $K_p=16$, as shown in Figure 2. Uncertainties in

the completeness are shown in the lower panel of Figure 2 and are derived from the number of observed stars at given magnitude (see details also in Do et al. (2013)).

For spectral completeness C_{spec} , we follow a process similar to that in Do et al. (2013), where each star from the GCOWS survey is assigned a probability of being young P_E . So for young stars, $P_E = 1$; for old stars, $P_E = 0$; for unknown type stars, P_E is simulated based on the Bayesian evidence for the early-type and late-type hypotheses using the known type stars as a training sample. However, not all young stars have spectra with good enough quality to measure RV. Therefore, the completeness used in this work is defined as "completeness for young stars with measured RV".

Stars are divided into 8 magnitude bins based on extinction-corrected magnitudes, $K_{p,ext}$, from 9 to 17 with 1 magnitude interval, and the spectral completeness curve is a linear interpolation. In each magnitude bin, the completeness C_{spec} is calculated using the following equation:

$$C_{spec} = \frac{N_{yngRV} + N_{yngWR}}{N_{yng} + \sum_{unk} P_E} \quad (2)$$

where N_{yngRV} is the number of young stars with well-measured RV, N_{yngWR} is the number of WR young stars, N_{yng} is the total number of young stars (including all spectrally identified young stars, no matter whether they have well-measured RV or not) and $\sum_{unk} P_E$ is the sum of the probability of being young for all unknown type stars. WR stars are all very bright and have high SNR spectra, but currently we cannot fit their emission lines due to lack of a good model. So we decided to include WR stars in the numerator, since the missing RVs from them are not because of incompleteness. The total completeness for young stars with RV is shown with the red line in Figure 2. Usually completeness will decrease towards fainter magnitudes, but a dip in the completeness curve appears at $K_p = 13$. This is because young stars are at the pre-main sequence turn-off point at this magnitude, so they are partially obscured by dust, making them harder to study.

For stars from Feldmeier-Krause et al. (2015), those authors reported 80% and 50% completeness in different radial bins. A linear interpolation is derived based on those two data points. Notice that their completeness is based on extinction-corrected magnitudes, $K_{p,ext}$, but we assume it is a reasonable approximation to the completeness curve in the observed magnitude system. The completeness curve for Feldmeier-Krause et al. (2015) stars is shown in Figure 2.

When determining which completeness to use for each star, we first need to determine whether this star is

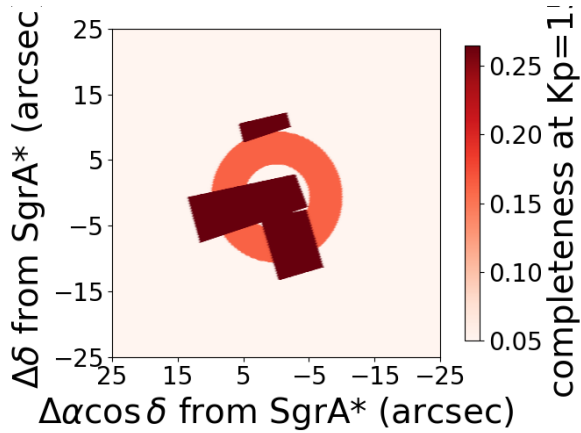


Figure 3. An example of completeness map at $k_p=15$ with color showing the completeness. For stars at this magnitude, completeness is higher in our curve, so GCOWS completeness is adopted for observed GCOWS regions (darker polygons) while completeness from [Feldmeier-Krause et al. \(2015\)](#) is adopted elsewhere (two concentric circles separating regions with radial distances $r < 5''$, $5'' \leq r < 10''$, and $10'' \leq r$).

within our GCOWS field. If a star is within our GCOWS field, we will use the higher completeness fraction between GCOWS and [Feldmeier-Krause et al. \(2015\)](#). Otherwise, completeness from [Feldmeier-Krause et al. \(2015\)](#) will be applied. An example of our completeness map at $K_p = 15$ is shown in Figure 3.

2.4. Position, Proper motion and Acceleration

Projected positions and proper motions on the sky are derived from high-resolution, infrared (IR) images obtained over a 10–25 yr time-baseline. Depending on the distance from Sgr A*, we either use observations from the 10 m telescopes at the W. M. Keck Observatory (WMKO) or the Hubble Space Telescope (HST), as described below.

(1) The central $10'' \times 10''$ region of the GC (approximately centered on Sgr A*) has been monitored with diffraction-limited, near-infrared imaging cameras at WMKO since 1995. For stars in this region, we have the longest time baseline and the highest spatial resolution, which gives precise proper motions and even significant accelerations on the sky plane. The complete catalog of measured positions, proper motions, and accelerations and analysis details is presented in [Jia et al. \(2019\)](#).

(2) To measure the proper motions of the young stars at larger radii, we use a widely dithered mosaic of shallow Keck IR images covering a $22'' \times 22''$ FOV as described in [Sakai et al. \(2019\)](#). The astrometric uncertainties in this mosaicked dataset are typically larger

than in the central $10''$ data, because of the shorter time baseline and lower SNR.

(3) For stars at even larger radii ($R > 7''.5$), we use proper motions measured from the HST WFC3-IR instrument. This dataset consists of 10 epochs of observations centered on Sgr A* that were obtained between 2010 – 2020 in the F153M filter (2010.5: GO 11671/PI Ghez, 2011.6: GO 11671/PI Ghez, 2012.6: GO 12318/PI Ghez, 2014.1: GO 13049/PI Do, 2018.1: GO 15199, PI Do, 2019.2: GO 15498/PI Do, 2019.6: GO 16004/PI Do, 2019.7: GO 16004/PI Do, 2019.8: GO 16004/PI Do, 2020.2: GO 15894/PI Do). While the HST spatial resolution is ~ 2.5 times lower than that achieved with the Keck observations (FWHM $\sim 0.17''$ versus FWHM $\sim 0.06''$), HST’s FOV of $120'' \times 120''$ is much larger than can be realistically achieved with current AO systems. The astrometry from each HST epoch is first transformed into the *Gaia* absolute reference frame ([Mignard & Klioner 2018](#)) and then further transformed into the AO reference frame via 2nd-order bivariate polynomial transformations. The resulting HST catalog achieves an average precision of 0.33 mas and 0.07 mas/yr for the positions and proper motions of the stars in the sample. A detailed description of the HST catalog will be provided in a future paper ([Hosek et al., in prep.](#)).

In summary, among 91 young stars from our sample described in §2.1, we are able to cross-match and measure proper motions for 88 stars. The proper motions for the final sample include 54 stars from data set 1, 20 from data set 2, and 14 from data set 3, as shown in Table 8.

2.5. Photometry and Extinction

To ensure that our final sample shares a common photometric system, we adopt the Kp magnitude for each star from the deep wide mosaic image analysis reported in [Lu et al. \(2013\)](#) which covers all 88 stars in our sample. The Kp magnitude for each star is reported in the Kp column in Table 8. Then we applied the latest extinction map from [Nogueras-Lara et al. \(2018\)](#) to differentially de-redden all stars to a common $A_{K_s} = 2.7$, and the extinction corrected magnitude is reported as Kp_{ext} in Table 8.

3. ORBIT ANALYSIS

For stars with measured $(x_0, y_0, v_x, v_y, v_z, a_R)$, the six Keplerian orbit parameters (inclination i , angle to the ascending node Ω , time of periaapse passage T_0 , longitude of periaapse ω , period P , and eccentricity e) can be analytically determined if the central potential is known ([Lu et al. 2009](#)). §3.1 describes the Monte Carlo process

used to estimate stars' orbital parameters given prior estimates on the central potential. For stars that show significant acceleration (S0-1, S0-2, S0-3, S0-4, S0-5, S0-8, S0-16, S0-19, S0-20), their orbits are best constrained by simultaneously fitting the astrometry and RV measurements as a function of time (Do et al. 2019). §3.2 describes the computationally expensive orbit fitting procedure used for these 9 stars.

3.1. MC analysis for stars with $(x_0, y_0, v_x, v_y, v_z, a_R)$

Orbital parameters are determined for the 79 stars without significant acceleration measurements using a Monte Carlo (MC) analysis as described in detail in Lu et al. (2009) and Yelda et al. (2014). Each star has measurements of the line-of-sight velocity (v_z) as described in §2.2 and proper motion parameters (x_0, y_0, v_x, v_y) as described in §2.4. The absolute value of the line-of-sight distance $|z|$ between the star and Sgr A* can be calculated from the following equation if a_R is known.

$$a_R = -\frac{GM_{tot}(r)R}{r^3}, r = \sqrt{R^2 + z^2} \quad (3)$$

Here, r is the 3D distance and R is the 2D projected sky-plane distance from Sgr A*, where $r^2 = R^2 + z^2$. We note that there is a sign ambiguity in the line-of-sight distance.

We sample the 6 measured position, velocity, and acceleration quantities 10^5 times assuming a Gaussian distribution for each measurement and its uncertainty. For each sample, the 6 Keplerian orbital parameters are analytically determined assuming an enclosed mass and distance to the Galactic Center as described below. The MC simulations produce a joint probability density function (PDFs) for the 6 orbital parameters.

The mass distribution giving rise to the central potential, M_{tot} , is a combination of the SMBH mass and an extended mass profile:

$$M_{tot}(r) = M_{BH} + M_{ext}(r) \quad (4)$$

The adopted SMBH properties include a mass of $M_{BH} = (3.975 \pm 0.058) \times 10^6 M_\odot$ and a distance of $R_0 = (7.959 \pm 0.059)$ kpc, based on the analysis of S0-2's orbit (Do et al. 2019). We used the extended mass profiles from Trippe et al. (2008) and found that adding extended mass has limited impact on the orbit analysis. We nonetheless adopt an extended mass profile with

$$M_{ext}(r) = \int_0^r 4\pi \frac{\rho_0}{1 + (r/R_b)^2} r^2 dr \quad (5)$$

where $\rho_0 \simeq 2.1 \times 10^6 M_\odot$ and the break radius is $R_b = 8.9''$. We have also tried other extended mass profiles,

like that of Schödel et al. (2009), and the results are similar.

Among the 79 stars, 45 have precise and accurate astrometry from Jia et al. (2019) with well-measured proper motions and constraints on the projected acceleration, a_R , as shown in Table 8. However, not all measured a_R values are physically allowed for a single star on a bound orbit around the supermassive black hole and enclosed extended mass. The maximum allowed a_R is set by the gravitational acceleration when $z = 0$ pc and we constrain the minimum allowed a_R to be the acceleration at a distance of $z = 0.8$ pc:

$$\begin{aligned} a_{Rmax}(R) &= -\frac{GM_{tot}(R)}{R^3} \\ a_{Rmin}(R) &= -\frac{GM_{tot}(r)R}{r^3}, r = \sqrt{R^2 + z^2}, z = 0.8pc \end{aligned} \quad (6)$$

The maximum z is chosen to be 0.8 pc because very few young stars are detected outside 0.4 pc and the most distant young star detected in our sample is at 0.6 pc. If the distribution of young stars is approximately spherically symmetric about the black hole, then the maximum line-of-sight distance should not exceed 0.8 pc. If a stars' measured a_R ($\pm 2\sigma_{a_R}$) overlaps with the allowed range, we draw its z in each MC trial from a Gaussian distribution with the mean set to the measured a_R , the standard deviation set to the measured σ_{a_R} , and truncated to the allowed a_R range. This is the case for 35 stars. For the rest of the stars without a significant or physical a_R , we use a uniform distribution in the range of allowed a_R . In Figure 4, we use three stars as an example to show how a_R is simulated in the MC analysis. The last column in that plot shows the distribution of a_R and its limits (a_{Rmax} and a_{Rmin}) in red dashed lines, while the orange histogram is the probability density function for simulated a_R .

The uniform acceleration prior, in the absence of other constraints, may lead to biased results in angular momentum measurements as shown in Yelda et al. (2014). It produces a deficit of stars close to $z=0$ as shown in Figure 4 and von Fellenberg et al. (2022), Fig. 12. However, as discussed above, we only apply this prior for roughly half of the stars that do not have a physically allowed or significant a_R , most of which are located at larger radii where the bias is less apparent. Thus the choice of a uniform acceleration prior does not strongly bias the results.

Even for those 35 stars with measured a_R within the allowed range, the significance of their accelerations varies. This is due to many factors, including the location of the star, the brightness of the star, the number of epochs in which the star is detected, etc. A more

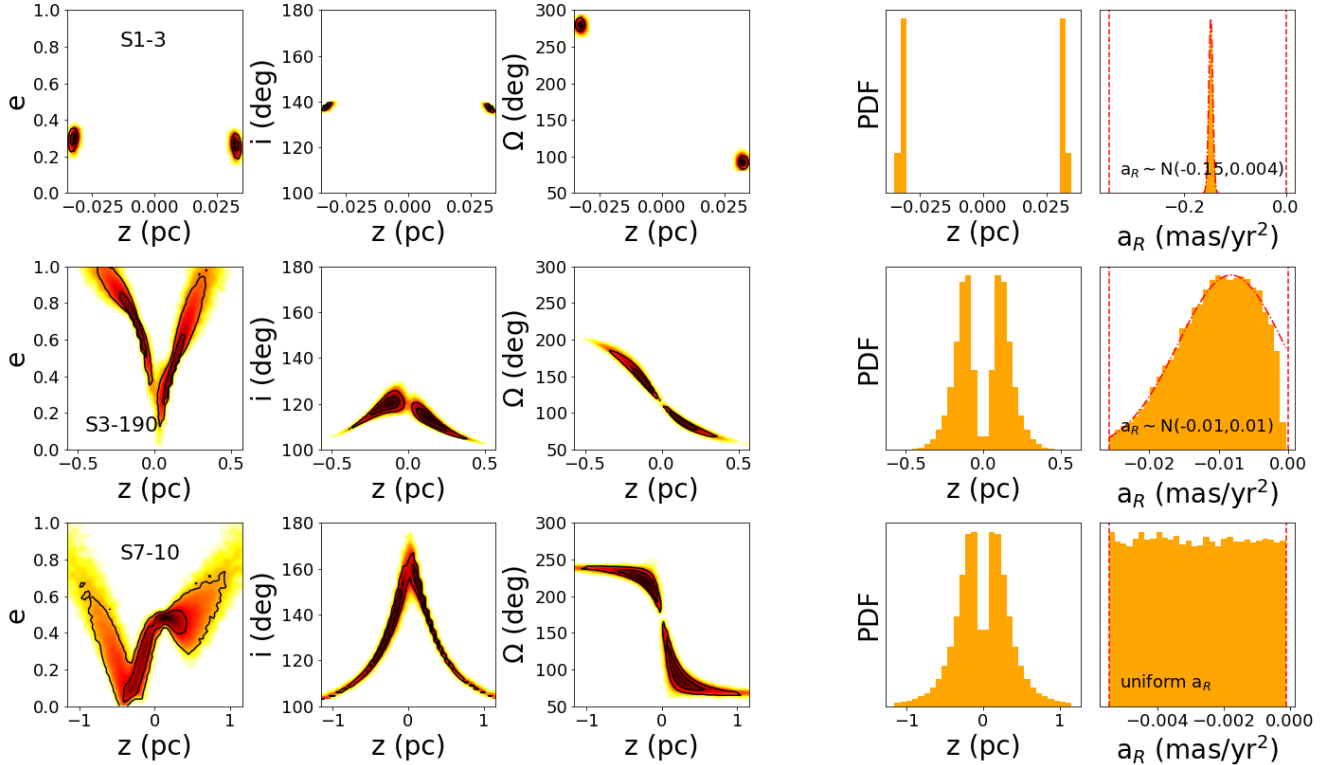


Figure 4. Examples of MC analysis for S1-3 (top), S3-190 (middle) and S7-10 (bottom). The left three columns show the density map for orbital parameters: e , i , Ω . The right two columns show the MC simulation input prior for z and a_R in orange histograms. For S1-3 and S3-190, their measured a_R and σ_{a_R} (red dashed line) are within the upper and lower limits (vertical red dashed lines), so the simulated a_R are drawn from Gaussian distribution $N \sim (a_R, \sigma_{a_R})$. For S7-10, no a_R is measured, so it is drawn from a uniform distribution between a_{Rmin} and a_{Rmax} . Simulated z is then derived from simulated a_R using Equation 3.

precise acceleration will result in more precise orbital parameters. In Figure 4, both S1-3 and S3-190 have a measurement-based a_R prior, while S7-10’s prior is uniform a_R over the allowed range. S1-3 has a $\sim 40\sigma$ significant acceleration, but S3-190 only has 1σ significant acceleration. As a result, S1-3 has much more constrained orbital parameters compared to S3-190. For S7-10 with a uniform a_R prior, its orbital parameters are even less constrained. The z distribution for S7-10 decreases with increasing radius even when a_R is evenly distributed, which agrees with observation and validates the uniform a_R prior.

3.2. Full Keplerian orbit fit for central stars

For stars with time-variable RV, we inferred their orbital parameters by simultaneously fitting spectroscopic and astrometric measurements. We utilized the same orbit-fitting procedure as was used by Do et al. (2019) to test General Relativity using the orbit of S0-2. From the orbit-fit posterior distributions, we drew 10^5 samples in order to match the posterior sample size for stars with a single RV from §3.1. S0-1, S0-2, S0-3, S0-4, S0-5,

S0-8, S0-16, S0-19, S0-20 in our sample are fitted this way. We adopted the observable-based prior paradigm from O’Neil et al. (2019) that is based on uniformity in observables to improve orbital solutions for low-phase-coverage orbits. A full Keplerian orbit fit for S0-2 is shown in Fig 5. All 9 stars’ fitted results are attached in appendix C.

4. DISK MEMBERSHIP ANALYSIS

4.1. Detecting Stellar Disks

Each star’s orbital plane can be uniquely described by a unit normal vector \mathbf{L} that is perpendicular to the orbital plane. This normal vector \mathbf{L} can be expressed in terms of the inclination (i) and the angle to the ascending node (Ω) (see Equation 8 in Lu et al. (2009)). Stars moving in a common plane share a common normal vector. In order to detect a stellar disk or stream, we adopt a nearest-neighbor method similar to that used by Lu et al. (2009) and Yelda et al. (2014). In this method, the sky is divided into 49152 pixels with equal solid angle area and for a given MC simulation the density at each

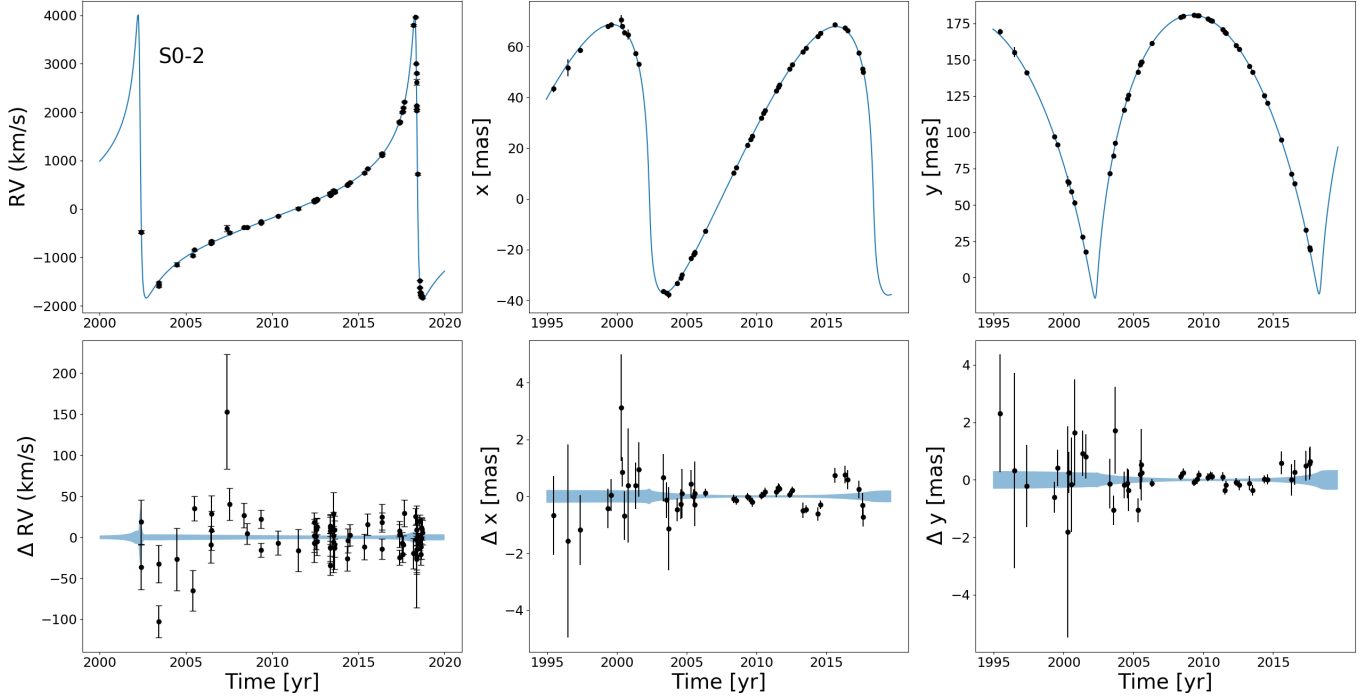


Figure 5. Examples of a full Keplerian orbit analysis for S0-2. The top row shows the line-of-sight velocity v_z and projected position from SgrA*: x , y as a function of time, and our model (blue line) fits both very well. The bottom row shows the offset between data and model as a function of time.

(i, Ω) position is calculated using the following equation:

$$\Sigma = \frac{k}{2\pi(1 - \cos \theta_k)} \text{ stars sr}^{-1} \quad (7)$$

where θ_k is the angle to the k th nearest star and we use $k = 6$. The resulting average density is nearly the same for other choices of $k = 4, 5$, or 7 . Then the combined density map is an average over all 10^5 MC trials from §3. The resulting density maps are presented in §5.

4.2. Disk/Plane Membership Probabilities

With the disk or plane normal-vectors and uncertainties determined from §4.1, the membership probability, L_{disk} , can be estimated for each star following Lu et al. (2009).

$$\begin{aligned} L_{\text{non-disk}} &= 1 - L_{\text{disk}} \\ &= 1 - \left(\frac{\int_{\text{disk}} PDF(i, \Omega) dSA}{\int_{\text{peak}} PDF(i, \Omega) dSA} \right) \end{aligned} \quad (8)$$

$$\int_{\text{disk}} dSA = \int_{\text{peak}} dSA \quad (9)$$

Here SA is the solid angle measured at the contour where the disk density drops to half of the peak value; $\int_{\text{disk}} PDF(i, \Omega) dSA$ is the integration of each

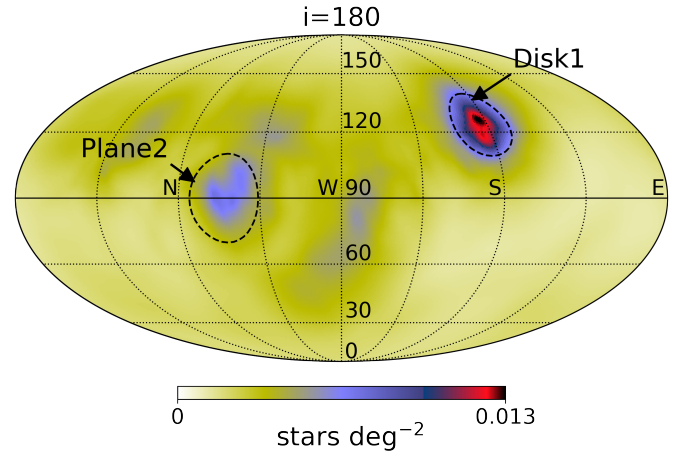


Figure 6. Density of normal vectors (i, Ω) (in stars deg^{-2}) of all 88 stars in our sample. Two significant over-dense region are marked as Disk1 and Plane2. Disk1 has a density of $0.014 \text{ stars deg}^{-2}$ located at $(i, \Omega) = (124^\circ, 94^\circ)$. Plane2 has a density of $0.007 \text{ stars deg}^{-2}$ located at $(i, \Omega) = (90^\circ, 245^\circ)$. The 1 sigma region is defined as the area inside the contour at which the density drops to half of its peak, and is circled by a black dashed line.

star's density map over the stellar disk region, and $\int_{\text{peak}} PDF(i, \Omega) dSA$ is the integration over its own peak region with the same SA.

In summary, each star’s $PDF(i, \Omega)$ is integrated inside the disk or plane area and normalized by the star’s peak probability over a similar area. Thus, stars with large uncertainties in i and Ω will only have high plane membership if they are centered on the plane. The final disk or plane memberships are presented in §5.

5. RESULTS

5.1. Two Stellar Disks

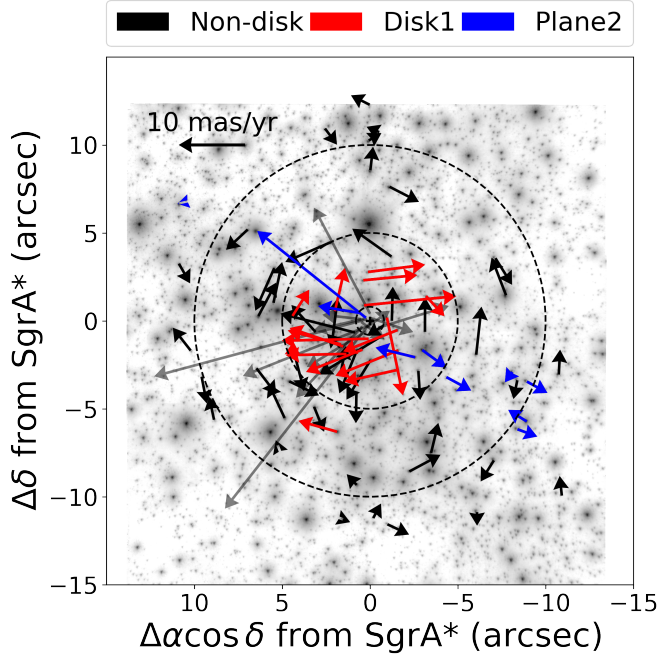


Figure 7. The proper motion direction for each star, where red arrows are Disk1 candidates and blue arrows are Plane2 candidates. The Non-disk stars are shown in black arrows, and the inner region stars are plotted with low opacity due to their large velocity.

The density map of normal vectors, \mathbf{L} , shows two over-dense regions, indicating the presence of at least two distinct populations, each of which consists of stars that share a common orbital plane (Figure 6). We label the two peaks as Disk1 and Plane2. The well-known clockwise (CW) disk is the upper right Disk1 located at $(i_{\text{Disk1}}, \Omega_{i,\text{Disk1}}) = (124^\circ, 94^\circ)$, consistent with the past measurements of the disk location (Levin & Beloborodov 2003; Genzel et al. 2003; Paumard et al. 2006; Lu et al. 2009; Bartko et al. 2009; Yelda et al. 2014; von Fellenberg et al. 2022). We found another almost edge-on plane which we call Plane2, located at $(i_{\text{Plane2}}, \Omega_{i,\text{Plane2}}) = (90^\circ, 245^\circ)$. This may be the same structure identified as F3 in von Fellenberg et al. (2022); Plane2 and F3 have similar eccentricity and semi-major axis distributions, along with $\sim 35\%$ of common members.

However, the two features are $>30^\circ$ apart in terms of Ω : von Fellenberg et al. (2022) found F3 has $(i, \Omega) = (102^\circ, 211^\circ)$ after conversion to our reference frame. A more detailed comparison is presented in Appendix B. The uncertainty in the location of each of the planar features is defined to be where the density drops to 50% of its peak value and it is marked with a black dashed line in Figure 6. The uncertainties for Disk1 and Plane2 are $(\sigma_{i,\text{Disk1}}, \sigma_{\Omega,\text{Disk1}}) = (15^\circ, 17^\circ)$, $(\sigma_{i,\text{Plane2}}, \sigma_{\Omega,\text{Plane2}}) = (20^\circ, 19^\circ)$. We also estimate the fraction of young stars belonging to each structure by calculating the sum of the membership probabilities over the total 88 young stars and found that $\sim 8.4\%$ of our sample belongs to Disk1 while $\sim 6\%$ belongs to Plane2.

To quantify the significance of both disks, we simulated an isotropic population with synthetic $(x_0, y_0, v_x, v_y, v_z)$ and extracted orbits in the same way as on the real data. Each simulated star was first assigned a 2D radius on the sky, R , and a 3D velocity, v_{tot} , drawn from the observed young stars. Then the orientation of the position and velocity vectors were randomly generated (Yelda et al. 2014). Any measurements of a_R were kept fixed in amplitude and uncertainty. For the 9 stars from §3.2 with well-measured orbits, we drew 10^5 samples from randomized i and Ω with their posterior distribution uncertainty. The significance of Disk1 and Plane2 is defined by:

$$S = \frac{\rho_{\text{disk}} - \rho_{\text{iso}}}{\sigma_{\text{iso}}} \quad (10)$$

where ρ_{disk} is the density of the stellar disk at its peak, ρ_{iso} is the density of the isotropic simulation at the same position, and σ_{iso} is the dispersion of the density at the peak among all the isotropic simulations at the same position. A summary of the peak density, significance, and the simulated isotropic density and its dispersion is presented in Table 2.

The significance for Disk1 is 12.4 and Plane2 has a significance of 6.4. The reason we have a slightly lower significance for Disk1 compared to Yelda et al. (2014) is because we have a smaller sample size due to our requirement that only stars from surveys with published completeness curves can be included. As a result, our uncertainty in the isotropic density is slightly larger.

The significance of Plane2 is only slightly higher than previously claimed planar structures and disks that were later shown to be statistically insignificant (Paumard et al. 2006; Bartko et al. 2009; Lu et al. 2009). Thus, we must be cautious in claiming a new dynamical structure. Unlike previous claimed structures, the Plane2 structure is the result of both numerous stars with moderate membership probabilities and at least 5 stars with $P_{\text{plane}} > 0.5$.

Table 2. Disk and Plane Summary

Structure	i ($^{\circ}$)	Ω ($^{\circ}$)	Solid Angle (sr)	ρ_{disk} (stars/deg 2)	ρ_{iso} (stars/deg 2)	Significance	Disk Fraction ^a
Disk1	124 ± 15	94 ± 17	0.20	0.013 ± 0.006	0.003 ± 0.0008	12.4	0.084
Plane2	90 ± 20	245 ± 19	0.37	0.007 ± 0.002	0.002 ± 0.0007	6.4	0.060

^aThis is calculated as sum of membership probabilities of stars belonging to each structure divided by the total 88 young stars.

The probability of each star belonging to Disk1 or Plane2 is given in Table 3. To view stars in Disk1 and Plane2 in a more direct way, we make a quiver plot showing the proper motion of each star in Figure 7. For illustrative purposes, we identify high-probability disk members as those with $P_{disk} > 0.2$; and Disk1 and Plane2 stars are shown as red and blue arrows, respectively. We note that all disk membership probabilities are calculated assuming the existence of only that disk. We choose not to determine disk membership using a more complex mixture model based on two simulated disks plus an isotropic population as it would require a prior knowledge of the disk properties such as the eccentricity and semi-major axis distributions.

Table 3. Disk Membership

Name	P_{Disk1}	P_{Plane2}	SA
S0-1	0.00	0.00	0.001
S0-11	0.00	0.05	0.081
S0-14	0.00	0.00	0.004
S0-15	0.76	0.00	0.004
S0-16	0.00	0.42	0.001
S0-19	0.00	0.00	0.002
S0-2	0.00	0.00	0.000
S0-20	0.00	0.00	0.001
S0-3	0.00	0.00	0.000
S0-30	0.00	0.00	0.106
S0-31	0.00	0.30	0.004
S0-4	0.00	0.00	0.001
S0-5	0.00	0.00	0.001
S0-7	0.00	0.00	0.001
S0-8	0.00	0.00	0.001
S0-9	0.00	0.00	0.003
S1-19	0.43	0.00	0.022
S1-2	0.50	0.00	0.004
S1-22	0.54	0.00	0.189
S1-24	0.00	0.00	0.003
S1-3	0.49	0.00	0.007
S1-33	0.00	0.00	0.122

Table 3 continued

Table 3 (continued)

Name	P_{Disk1}	P_{Plane2}	SA
S1-4	0.02	0.00	0.081
S1-8	0.00	0.00	0.003
S10-185	0.00	0.73	0.132
S10-232	0.00	0.00	0.578
S10-238	0.00	0.78	0.002
S10-32	0.18	0.00	0.119
S10-34	0.00	0.00	0.517
S10-4	0.00	0.00	0.087
S10-48	0.00	0.00	0.037
S10-50	0.00	0.00	0.400
S11-147	0.00	0.00	1.322
S11-176	0.00	0.00	0.237
S11-21	0.04	0.00	0.174
S11-214	0.00	0.00	0.131
S11-246	0.00	0.01	0.209
S11-8	0.00	0.00	0.784
S12-178	0.00	0.03	0.008
S12-5	0.00	1.00	0.003
S12-76	0.00	0.00	0.257
S14-196	0.00	0.00	0.410
S2-17	0.37	0.00	0.009
S2-19	0.24	0.00	0.071
S2-21	0.50	0.00	0.018
S2-4	0.22	0.00	0.007
S2-50	0.00	0.00	0.188
S2-58	0.00	0.00	0.188
S2-6	0.50	0.00	0.009
S2-74	0.50	0.00	0.044
S3-19	0.36	0.00	0.357
S3-190	0.35	0.00	0.084
S3-26	0.24	0.24	0.163
S3-3	0.00	0.00	0.467
S3-30	0.00	0.00	0.012
S3-331	0.00	0.00	0.103
S3-374	0.00	0.00	0.086
S3-96	0.00	0.00	0.351
S4-169	0.40	0.00	0.420

Table 3 continued

Table 3 (*continued*)

Name	P _{Disk1}	P _{Plane2}	SA
S4-262	0.00	0.00	0.117
S4-314	0.47	0.00	0.231
S4-364	0.00	0.00	0.296
S4-71	0.00	0.00	0.012
S5-106	0.00	0.34	0.029
S5-183	0.00	0.00	0.094
S5-191	0.00	0.00	0.612
S5-237	0.00	0.00	0.247
S6-63	0.27	0.00	0.215
S6-81	0.00	0.00	0.086
S6-89	0.00	0.00	0.398
S6-96	0.00	0.00	0.411
S7-10	0.16	0.03	0.285
S7-216	0.00	0.00	0.153
S7-236	0.00	0.00	0.873
S7-30	0.00	0.00	0.592
S7-5	0.05	0.00	0.499
S8-10	0.00	0.00	0.769
S8-126	0.00	0.00	1.139
S8-196	0.00	0.22	0.142
S8-4	0.00	0.00	0.032
S8-5	0.00	0.00	0.370
S8-8	0.01	0.00	0.271
S9-143	0.01	0.00	1.220
S9-221	0.00	0.77	0.044
S9-6	0.04	0.00	0.267
IRS 13E1	0.00	0.50	0.002
IRS 16CC	0.25	0.00	0.070
IRS 33N	0.00	0.00	0.004

5.2. Disk Properties

In this section, we compare the distribution of eccentricities (e), radial distances on the disk plane R_{plane} (derived in §5.2.2) and disk thickness for the different dynamical subgroups. We then use this distribution as the input prior for disk simulations in §5.3.

5.2.1. Eccentricity Distribution

Stars are divided into Disk1, Plane2 and Non-disk stars using membership probabilities as weights rather than through a hard probability cut. We assign a weight to each MC trial among the 10^5 trials for every star (§3). For a particular MC trial with a set of Keplerian orbital parameters (i, Ω, e, a), the weight of being on Disk1 (W_{Disk1}), Plane2 (W_{Plane2}) and Non-disk ($W_{\text{Non-disk}}$)

structures are calculated as:

$$\begin{aligned}
 W_{\text{Disk1}}(i, \Omega, e, a) &= N(i|\mu = i_{\text{Disk1}}, \sigma = \sigma_{i,\text{Disk1}}) \times \\
 &\quad N(\Omega|\mu = \Omega_{\text{disk1}}, \sigma = \sigma_{\Omega,\text{Disk1}}) \\
 W_{\text{Plane2}}(i, \Omega, e, a) &= N(i|\mu = i_{\text{Plane2}}, \sigma = \sigma_{i,\text{Plane2}}) \times \\
 &\quad N(\Omega|\mu = \Omega_{\text{Plane2}}, \sigma = \sigma_{\Omega,\text{Plane2}}) \\
 W_{\text{Non-disk}}(i, \Omega, e, a) &= 1 - W_{\text{Disk1}}(i, \Omega, e, a) \\
 &\quad - W_{\text{Plane2}}(i, \Omega, e, a)
 \end{aligned} \tag{11}$$

where $N(\mu, \sigma)$ is normal distribution with mean of μ and standard deviation of σ .

We modeled the underlying eccentricity distribution for Disk1, Plane2, and the Non-disk populations separately. We used a hierarchical Bayesian inference (HBI) method similar to Hogg et al. (2010) and Bowler et al. (2020) to infer the population-level eccentricity distribution of each sub-structure. This method was proposed first in constraining the population-level eccentricity distribution of exoplanets, where a standard maximum-likelihood estimator of eccentricity is biased to a high value. HBI is especially useful when, as shown in Bowler et al. (2020), the measured eccentricity posteriors for individual stars vary significantly with some well constrained, others poorly determined, and most with asymmetric or non-Gaussian probability distributions (see also Wolfgang et al. 2016; Eyles et al. 2019).

To apply this framework to our case, we first adopted a Beta distribution for the eccentricity distribution for each population,

$$P(e|\alpha, \beta) = \frac{\Gamma(\alpha + \beta)}{\Gamma(\alpha)\Gamma(\beta)} e^{\alpha-1} (1-e)^{\beta-1}. \tag{12}$$

where Γ is the usual Gamma function defined as $\Gamma(z) = \int_0^\infty x^{z-1} e^{-x} dx$. Recall that a Beta function can reproduce distributions that are uniform ($\alpha = 1, \beta = 1$), peaked at low e (small α), peaked at high e (small β), and anything in between, which makes the distribution very flexible. We then used HBI to find the most probable α and β parameters for each population's eccentricity distribution, solving for

$$P(\{\theta_s\}, \mathcal{E}|\{d_s\}) = \frac{P(\{d_s\}|\{\theta_s\})P(\{\theta_s\}|\mathcal{E})P(\mathcal{E})}{P(\{d_s\})} \tag{13}$$

where $\mathcal{E} = (\alpha, \beta)$ describes the population's eccentricity distribution, $\{\theta_s\}$ is the set of orbital parameters for each star, s , and $\{d_s\}$ is the data for each star. This enables us to use posterior samples from an individual star's eccentricity distribution to estimate the population's distribution. As we already have posterior samples for the individual stars' orbital parameters, θ_s , similar to Bowler et al. (2020), we can write the posterior

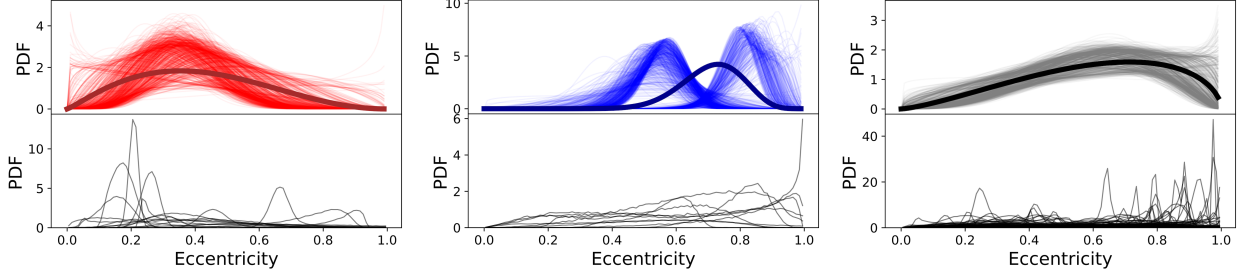


Figure 8. The best-fit (thick line) eccentricity distribution for Disk1 (left), Plane2 (middle), and Non-disk (right) young stars. Fit uncertainties are drawn as thin lines in top plots. We randomly draw 1000 parameters from the posterior probability distributions and plot corresponding Beta distributions. Bottom plots show individual eccentricity posterior distributions of stars belonging to each structure. Disk1 stars peak at lower eccentricities while Plane2 and Non-disk young stars have higher eccentricities. Plane2 has large uncertainties and the drawn 1000 parameters result in distributions that have two prominent peaks. This may imply a bi-modal distribution for Plane2; however, given the small sample size, the bi-modality is not significant.

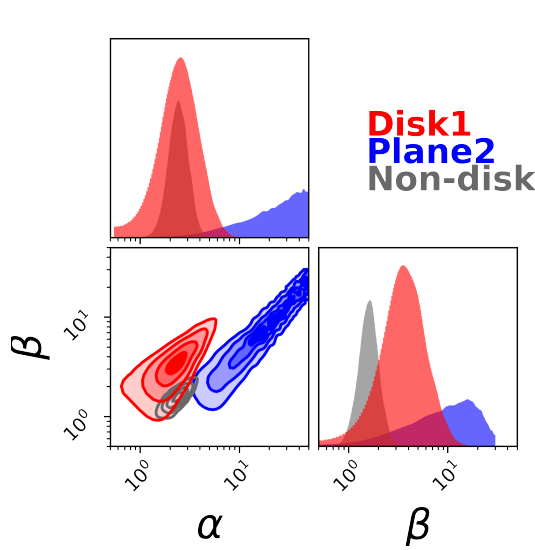


Figure 9. Posterior probability density for the eccentricity distribution parameters, α and β , for all three groups of young stars. Contours show the 0.5, 1, 1.5, and 2 sigma regions.

distribution of hyper-parameters \mathcal{E} as:

$$P(\mathcal{E}|\{d_s\}) \propto \mathcal{L}(\{d_s\}|\mathcal{E}) \pi(\mathcal{E}) \quad (14)$$

where $\pi(\mathcal{E})$ is the prior on the hyper-parameters. Then we can approximate the likelihood $\mathcal{L}(\{d_s\}|\mathcal{E})$ for the population parameters by importance sampling the existing posteriors with

$$\mathcal{L}(\{d_s\}|\mathcal{E}) \approx \prod_{s=1}^{N_{stars}} \frac{c_s}{K} \sum_{k=1}^K \frac{P(e_{sk}|\mathcal{E})}{\pi(e_{sk})} \quad (15)$$

where e_{sk} is the eccentricity of the k -th draw for star s as described in Hogg et al. (2010) and c_s is the membership probability for each star. The orbital parameter posteriors for most stars were generated using a Monte-Carlo sampling method and an explicit eccentricity prior was

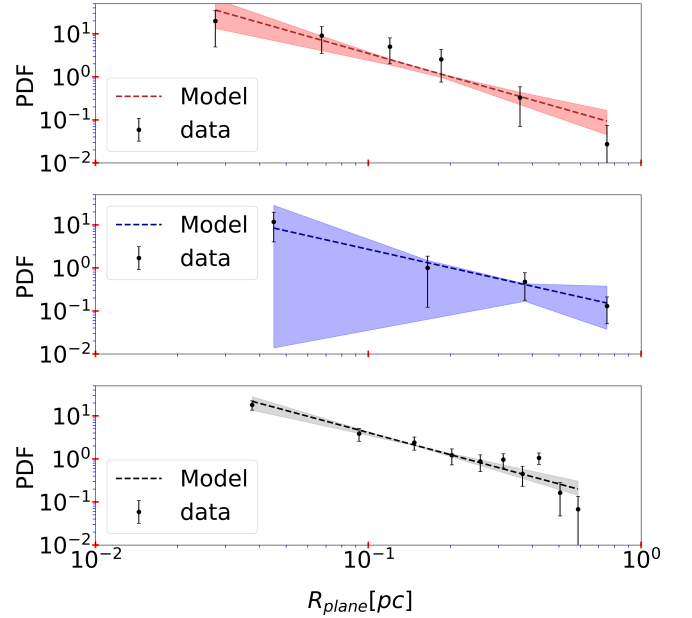


Figure 10. Radial distributions for the three dynamical subgroups and the best-fit model. The top plot is for Disk1 (red), the middle plot is for Plane2 (blue), and the bottom plot is for the Non-disk population (grey). The colored envelope in each plot defines region of uncertainty for the model. We draw 200 samples from the posterior distribution of model parameter and calculate corresponding uncertainty region (plotted as shaded areas).

not utilized. However, the uniform a_R prior produces a fairly uniform eccentricity distribution; thus we assume that $\pi(e_{sk})$ is uniform. Priors on α and β were uniform from $[0, 50]$ and $[0, 30]$, respectively. The final posterior probability distribution on \mathcal{E} was inferred using the nested sampling package, *Dynesty* (Speagle 2020; Skilling 2004, 2006; Feroz et al. 2009; Higson et al. 2019).

The best-fit eccentricity distributions are plotted in Figure 8. For the Disk1 population, we see a peak at $e = 0.36$, which is consistent with the previous de-

termination by Yelda et al. (2014), but with a larger spread, implying more high eccentric orbits in Disk1. For the Plane2 population, the eccentricity distribution is shifted to higher eccentricities, although the uncertainties are large, given the small number of stars. We adopt the maximum-likelihood solution for all three populations, including Plane2, even though the intrinsic eccentricity distribution is uncertain and may have a different functional form. For the Non-disk stars, the distribution is fairly flat, with a slight preference for higher eccentricities. Both the Plane2 and Non-disk populations are consistent, within uncertainties, with a relaxed population, which should scale as $P(e) \propto e$; however, a non-relaxed, but high, eccentricity distribution is preferred (Figure 9). To summarize, we find that the eccentricity distributions are described by:

$$\begin{aligned} P_{\text{Disk1}}(e) &= \text{Beta}(\alpha = 3.2 \pm 1.4, \beta = 5.0 \pm 2.4) \\ P_{\text{Plane2}}(e) &= \text{Beta}(\alpha = 31.9 \pm 11.9, \beta = 15.2 \pm 6.8) \\ P_{\text{Non-disk}}(e) &= \text{Beta}(\alpha = 2.6 \pm 0.6, \beta = 1.7 \pm 0.4). \end{aligned} \quad (16)$$

5.2.2. Radial Profile

In order to calculate a star's radial position on the disk, we first need to find its projected position vector on the disk plane. We have the x_{sky} and y_{sky} positions for each star and thus we need to calculate z_{plane} on the disk plane. To do this, we begin by finding the normal vector to the disk, \mathbf{L} , from its i and Ω :

$$\mathbf{L} = \begin{pmatrix} L_x \\ L_y \\ L_z \end{pmatrix} = \begin{pmatrix} \sin i \cos \Omega \\ -\sin i \sin \Omega \\ -\cos i \end{pmatrix} \quad (17)$$

After calculating the normal vector $\hat{\mathbf{L}}$, combined with known x_{sky} and y_{sky} positions of stars, we find z_{plane} by projecting stars onto the disk plane:

$$z_{plane} = \frac{-(L_x x_{sky} + L_y y_{sky})}{L_z} \quad (18)$$

then the radial distances R_{plane} are calculated by Pythagorean Theorem.

To create the PDFs of the R_{plane} distributions for both Disk1 and Plane2, we sample both stars and structures simultaneously. First, a sample of i_{star} and Ω_{star} is drawn for each star from its MC result $5 \cdot 10^4$ times. Second, another sample of each structure's i_{disk} and Ω_{disk} is created by drawing $5 \cdot 10^4$ times from a Gaussian distribution defined by the means and uncertainties of i and Ω shown in Table 2. We randomly match elements of these two samples to create a new data set, where

each data set contains one combination of a star's i_{star} and Ω_{star} and a disk's i_{disk} and Ω_{disk} . From this new data set, we calculate R_{plane} values for each combination using Eqs. 17 and 18. Additionally, we imposed a cut of 20 parsecs on our values of R_{plane} because these dynamical sub-structures, especially Plane2, are close to edge-on.. Without this cut, we would obtain values of R_{plane} approaching infinity.

We also calculate a weight associated with each data in the following way, assuming no change in uncertainty of disk parameters and a normal distribution.

$$\begin{aligned} W(i_{star}, \Omega_{star} | i_{disk}, \Omega_{disk}, \sigma_{i,disk}, \sigma_{\Omega,disk}) &= \\ N(i_{star} | \mu = i_{disk}, \sigma = \sigma_{i,disk}) \times & \quad (19) \\ N(\Omega_{star} | \mu = \Omega_{disk}, \sigma = \sigma_{\Omega,disk}) & \end{aligned}$$

This is the probability of each sampled star being located on the sampled disk. We do not use membership probability because it is an integrated result and could not reflect details of sampled data. Then a weighted histogram of 88 stars is created for each sampled disk's i_{disk} and Ω_{disk} . Each histogram is normalized by 2D bin widths (i.e. annular area between each bin) to account for the 2D geometry of disk structure. The final PDF of R_{plane} for each structure is obtained by taking the mean across these histograms and the uncertainties are estimated by the standard deviation. For the off-disk population, there is no disk to project the stars onto, so the stars' radial positions on the plane of the sky are considered. An R_{sky} distribution is then created through a normalized distribution of the data. The uncertainties of these data points are estimated by the Poisson error on each data point.

The data were fit using Bayesian inference with multi-nested sampling by the Dynesty python package. From inspection, we decided to fit the R_{plane} distribution by a truncated single power-law for all three structures. Thus we only need to fit for the slope parameter α .

To estimate the uncertainty of the model, we sampled the posterior distributions of the model parameters 200 times, each time recalculating the model. We estimate the uncertainty by taking the standard deviation of all these calculated models. The radial distributions and best-fit models for the three subgroups are shown in Figure 10.

We find that that the radial position distribution in the disk and the sky are described by:

$$\begin{aligned} P_{\text{Disk1}}(R_{plane}) &= \text{Plaw}(\alpha = -1.80 \pm 0.17) \\ P_{\text{Plane2}}(R_{plane}) &= \text{Plaw}(\alpha = -1.43 \pm 0.47) \\ P_{\text{Non-disk}}(R_{sky}) &= \text{Plaw}(\alpha = -1.71 \pm 0.10). \end{aligned} \quad (20)$$

We initially fit the R_{plane} distribution of Disk1 by the truncated broken power law with model parameters α_1 , α_2 , and r_{break} . However, this results in huge uncertainties on model parameters. To justify our choice of a single power law, we compare values of both the Bayesian Information Criterion (BIC) and Akaike Information Criterion with small sample modification (AICc) for these two models. The results are shown in Table 4. From this table, the difference between BIC values of Disk1 for different models is ~ 2 , which suggests moderate evidence against single power law. However, the AICc strongly prefers a single power law with difference of about 10. Thus we conclude that there is no preference between these two models for Disk1 and we choose to present the single power-law result because it has well constrained parameters. Similar reasoning applies to the off-disk population. For the Plane2 population, we prefer a single power law due to its few data points compared to the number of parameters.

Table 4. BIC and AICc

Model	Structure	BIC	AICc
Single Power Law	Disk 1	20.72	21.93
Broken Power Law	Disk 1	19.85	32.48
Single Power Law	Plane 2	5.45	8.07
Broken Power Law	Plane 2	8.08	N/A ^a
Single Power Law	Non-disk	15.78	15.98
Broken Power Law	Non-disk	12.99	16.08

^aAICc does not apply to Plane2 because the number of data points equals to the number of parameters plus one, which rejects Broken Power Law model (overfitting).

The thickness of the disk can be estimated using the velocity dispersion perpendicular to the disk plane. Here we follow the process described by Lu et al. (2009). First, each potential disk candidate’s three-dimensional velocity, \vec{v} , is projected into the direction of \hat{L} . The uncertainty of both \vec{v} and \hat{L} are taken into consideration when calculating intrinsic velocity dispersion σ_{v_n} , where $v_n = \vec{v} \cdot \hat{L}$. Then the disk’s scale height (h/r) can be derived from the ratio of σ_{v_n} and $\langle \vec{v} \rangle$, where σ_{v_n} is the intrinsic velocity dispersion, and $\langle \vec{v} \rangle$ is the average magnitude of the 3D velocity of disk candidates, weighted their by disk membership probability. Finally, this scale height can be related to disk thickness described in terms of disk-opening angle $h/r \propto \sqrt{1/2\Delta\theta}$. For Disk1, we find $\sigma_{v_n} = 33 \text{ km s}^{-1}$, giving a scale height of 0.09 ± 0.01 and a disk-opening angle of $7.0^\circ \pm 0.9^\circ$, consistent with previous results (Lu et al. 2009; Yelda

et al. 2014). For Plane2, we find $\sigma_{v_n} = 58 \text{ km s}^{-1}$, giving a scale height of 0.23 ± 0.07 and a disk-opening angle of $18.6^\circ \pm 6.2^\circ$.

5.3. Simulations

From Figure 7, we can see the spatial distribution within each disk plane does not appear symmetric, especially for Plane2 stars. Intrinsic asymmetry is important in understanding and constraining the subgroup’s dynamical history. However, there are many reasons that can lead to this observed asymmetry: extinction, incomplete observation, and intrinsic asymmetry. In order to characterize this asymmetry, we simulate the whole cluster and each dynamical sub-structure using properties determined in §5.2. We also take inverse-completeness (see §2.3) and the full extinction map from (Schödel et al. 2010) into account when doing the simulation in order to diminish the effects from these two factors. Then we compare the simulated stellar distribution to the observed one to explore whether the structure is intrinsically asymmetric or not.

Table 5 summarizes the input simulation parameters. First, we use an open-source python package *SPISEA* (Hosek et al. 2020) to generate a single age (6 Myr) star cluster with solar metallicity, located 8 kpc away. The total mass of the simulated cluster is $10^5 M_\odot$, with minimum mass of $1 M_\odot$, maximum mass of $100 M_\odot$, and a power-law IMF with a slope of -2.35 (Salpeter 1955). While the IMF for the YNC has been shown to be top-heavy (Bartko et al. 2009; Lu et al. 2013), the analysis of the kinematic and spatial sub-structure is relatively insensitive to the choice of IMF and total cluster mass as we re-scale the simulated clusters to match observed stellar densities. We generate the synthetic photometry for each star in the NIRC2 Kp filter, assuming a fixed extinction value of $A_{K_s} = 2.7 \text{ mag}$, for easy comparison to the observed $K_{p_{ext}}$ shown in Table 8. In this step, we assume the three dynamical subgroups have the same age, IMF, and extinction.

The cluster generated by *SPISEA* gives mass and $K_{p_{ext}}$ for every star in the system. However, our analysis excludes all WR stars because the generated values of mass and $K_{p_{ext}}$ are less trustworthy compared to non-WR stars. The next step is to assign a position for each star based on their dynamical subgroup. We use the disk properties from §5.2 to simulate positions for Disk1, Plane2 and Non-disk stars. To account for differential extinction over the field of view, which introduces asymmetric features in the observed distributions, we redden the $K_{p_{ext}}$ back to observed Kp using the full extinction map from Schödel et al. (2010) and then apply an inverse completeness map from §2.3 to account for stars

Table 5. Characteristics of the Simulated Cluster Subgroups

Parameters	Disk1	Plane2	Non-disk
i	$N \propto (i_{\text{Disk1}} = 124^\circ, \sigma_{i,\text{Disk1}} = 15^\circ)$	$N \propto (i_{\text{Plane2}} = 90^\circ, \sigma_{i,\text{Plane2}} = 20^\circ)$	$P(i) \propto \cos(i)$
Ω	$N \propto (\Omega_{\text{Disk1}} = 94^\circ, \sigma_{\Omega,\text{Disk1}} = 17^\circ)$	$N \propto (\Omega_{\text{Plane2}} = 245^\circ, \sigma_{\Omega,\text{Plane2}} = 19^\circ)$	Uniform($0^\circ, 360^\circ$)
ω	Uniform($0^\circ, 360^\circ$)	Uniform($0^\circ, 360^\circ$)	Uniform($0^\circ, 360^\circ$)
e	Beta($\alpha = 3.2 \pm 1.4, \beta = 5.0 \pm 2.4$) ^b	Beta($\alpha = 31.9 \pm 11.9, \beta = 15.2 \pm 6.8$)	Beta($\alpha = 2.6 \pm 0.6, \beta = 1.7 \pm 0.4$)
a ^c	Plaw($\alpha = -1.80 \pm 0.17$) ^b	Plaw($\alpha = -1.43 \pm 0.47$)	Plaw($\alpha = -1.71 \pm 0.10$)
t_0	Uniform(1995, 1995+period)	Uniform(1995, 1995+period)	Uniform(1995, 1995+period)
M_{\min}	$1M_\odot$	$1M_\odot$	$1M_\odot$
M_{\max}	$150M_\odot$	$150M_\odot$	$150M_\odot$
M_{cluster}	$10^5 M_\odot$	$10^5 M_\odot$	$10^5 M_\odot$
Age	6Myr	6Myr	6Myr
IMF	$\xi(m) \propto m^{-2.35}$	$\xi(m) \propto m^{-2.35}$	$\xi(m) \propto m^{-2.35}$
distance	8kpc	8kpc	8kpc

^aEqu 16.

^bFor simulated cluster, we choose to only use peak parameters corresponding to max likelihood.

^cEqu 20. Here we use a to represent the radial distance r_{plane} . For each broken power law, we choose $a_{\min} = 0.01\text{pc}$ and $a_{\max} = 1.0\text{pc}$.

that would not be observable. This approximates how the simulated cluster would appear in observations. The comparison of the observed stellar density profile with the simulated density profile is shown in Figure 11. We present the density profile in polar coordinates, where North is at 90° and West is at 0° , so that it is easier to see the azimuthal structure in each dynamical subgroup. These plots have the same orientation as they appear on the sky.

For the Non-disk group, the sub-structure is mainly caused by the differential extinction, and our simulation reproduces the observation well within uncertainties. This indicates that the Non-disk group is nearly isotropic. For Disk1 and Plane2, we expect an overdensity in their disk plane, which can be seen in both the observed and simulated maps. However, for Plane2, the observed density on the Southwest side is significantly more dense than the observed density on the Northeast side (left plot of (c) in Figure 11), which is less significant in the simulated stellar distribution (right plot of (c) in Figure 11). Because we have taken both completeness and extinction into account when doing the simulation, this difference between observed and simulated stellar distribution should be explained by reasons other than these two factors. Thus, we think this difference implies that Plane2 is intrinsically asymmetric and may be a stream rather than a plane.

6. DISCUSSION

The presence of multiple sub-structures in the young nuclear cluster implies that star formation occurred in dynamically complex gas structures around the SMBH. We can infer that the structures that are observed today are related, but not identical, to the initial gas structure since the two-body relaxation timescale is longer (≥ 30 Myr – 1 Gyr Kocsis & Tremaine (2011)) than the age of the YNC (3 – 8 Myr Lu et al. (2013)). However, some dynamical evolution is expected due to vector resonant relaxation at radii $< 1''$ (0.04 pc) and resonant friction at larger radii. In particular, Levin (2022) notes that resonant friction can take a single disk and smear it into transient streams with different orientations in only a few Myrs. Note, the asymmetric gravitational potential due to the surrounding circum-nuclear disk at a few pc may dampen these resonant dynamical processes. More precise theoretical simulations are needed to run back the clock from the sub-structures observed today to the initial configuration at the time of star formation. More detailed discussion is presented below.

6.1. Comparisons to Previous Work

While the CW disk has been verified many times in previous work (Levin & Beloborodov 2003; Genzel et al.

2003; Paumard et al. 2006; Lu et al. 2009; Yelda et al. 2014; von Fellenberg et al. 2022), other kinematic structures in the young nuclear cluster have been controversial. A counter-clockwise (CCW) disk was originally reported in Genzel et al. (2003) and confirmed in Paumard et al. (2006). Later work (Bartko et al. 2009; von Fellenberg et al. 2022) found that the CCW disk was highly extended, anisotropic, and showed evidence for a warped disk on large scales. However, this CCW disk was not detected by Lu et al. (2009) and Yelda et al. (2014) in an independent analysis with different observations for RVs and proper motions. In the work presented here, we confirm the existence of the CW disk, with properties consistent with previous analyses, and we also do not detect the CCW disk. Instead, we detect a second edge-on disk called Plane2 (c.f., §6.4), which might be the same as the F3 structure reported in von Fellenberg et al. (2022) (c.f., §5.1, Appendix B.2).

A comparison of the locations of the CW disk, CCW disk and Plane2 on the density map is presented in Figure 12, from which we conclude that the position of Plane2 is clearly very different from that of the previously claimed CCW disk.

There are small discrepancies between our work and that of vF22 for the significance and locations of Disk1 and Plane2. These are likely due to significant differences in proper motions at small radii and large, but not statistically significant, differences in radial velocities. In addition, our requirement of spectroscopic completeness information for stars to be included in our sample yields an overall smaller number of young stars. Lastly, our use of a uniform acceleration prior (c.f., §3.1) on $\sim 50\%$ of the stars at large radii may also influence structure detection.

The stars within $0.8''$ are more randomized by dynamical effects like vector resonant relaxation (Rauch & Tremaine 1996; Hopman & Alexander 2006; Alexander 2007), so the inner edge of the CW disk is roughly at $0.8''$ as reported in (Schödel et al. 2003; Ghez et al. 2005; Gillessen et al. 2009). This agrees with our analysis. In our sample, we have 14 young stars within $0.8''$ and all of them have zero probability of being on Disk1.

6.2. CW Disk1 Properties

The stars in Disk1 are found to have non-circular orbits. Bartko et al. (2009) combined their results with those of Gillessen et al. (2009) and reported an eccentricity distribution with $\langle e \rangle = 0.36 \pm 0.06$. Yelda et al. (2014) divided stars into accelerating sources and non-

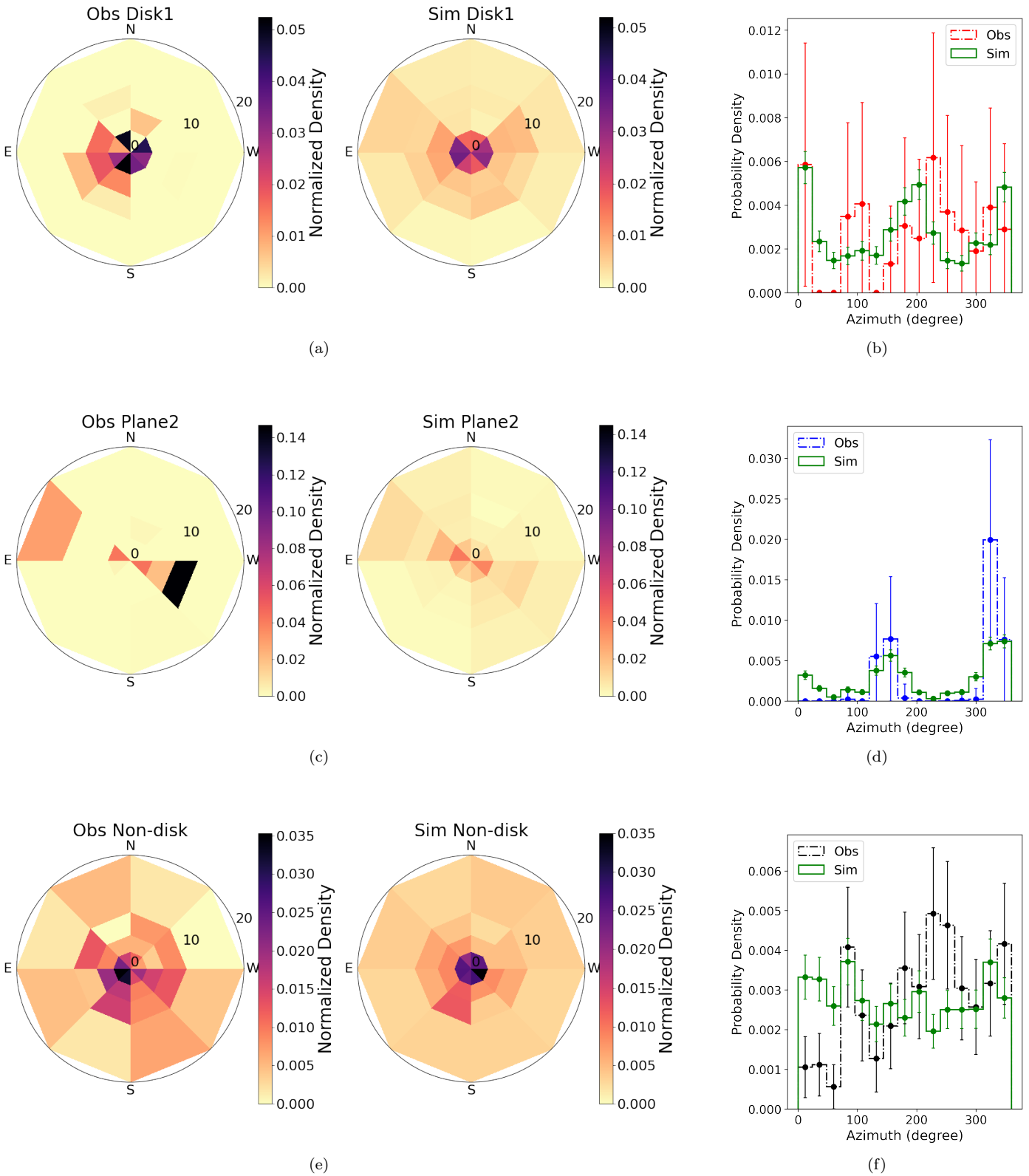


Figure 11. Stellar density map comparison between observation and simulation for Disk1 (top), Plane2 (middle) and Non-disk (bottom) subgroups. The first two columns are the stellar density map in polar system for observation (left) and simulation (middle), in which North is at 90° and West is 0° . We choose this coordinate system to be consistent with how Ω is defined. The right column is the 1D histogram of azimuth. For the Disk1 and Plane2 groups, the over-dense regions are mostly attributable to the orientation of the disk, while for the Non-disk group, the asymmetry is less significant, resulting from the differential reddening map. Within uncertainties, the 1D azimuthal distribution is consistent between the observation and simulation for Disk1 and Non-disk group. However for Plane2, the paucity of stars in the northeast sector of the observed map cannot be explained by the simulation itself.

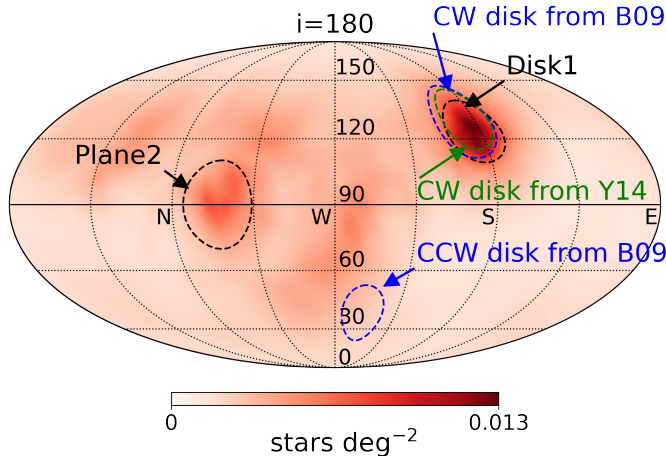


Figure 12. Proposed stellar disk from previous work and our work. Here we plot the CW disk and CCW disk from Bartko et al. (2009) (shortened as B09) in blue and the CW disk from Yelda et al. (2014) in green. The stellar disk reported in our work is shown in black. The CW disk, on the other hand, is very consistent between different analyses.

accelerating ² sources, having $\langle e \rangle = 0.27 \pm 0.09$ and $\langle e \rangle = 0.43 \pm 0.24$, respectively. Our eccentricity distribution for Disk1 is shown in Figure 8 and has a peak at $e = 0.36$ and $\langle e \rangle = 0.39 \pm 0.16$. Our result has a much larger uncertainty due to our requirement of only using data with completeness information, which results in a smaller overall sample. We performed an analysis similar to that of Yelda et al. (2014), dividing stars into accelerating and non-accelerating moving stars. The accelerating sources are defined in Jia et al. (2019), including 4 stars in our sample: S1-2, S1-3, S2-6 and S4-169. The comparison of e distribution between accelerating and non-accelerating sources in Disk1 are plotted in Figure 13, which agrees with the conclusion from Yelda et al. (2014) - accelerating sources have a well constrained e peaking at 0.2, while the e distribution of non-accelerating sources has a much larger dispersion. Specifically, accelerating sources have $\langle e \rangle = 0.25 \pm 0.12$ while non-accelerating sources have $\langle e \rangle = 0.45 \pm 0.24$. The difference is likely due to accelerating sources having better constraints on their orbital parameters (see Figure 4).

Disk1 has a significant intrinsic thickness as was shown by Paumard et al. (2006); Lu et al. (2009) and Yelda et al. (2014). For example, Paumard et al. (2006) reported a disk opening angle of $\Delta_\theta = 14^\circ \pm 4^\circ$ and Lu

² These stars also have accelerations but are insignificant that we cannot detect.

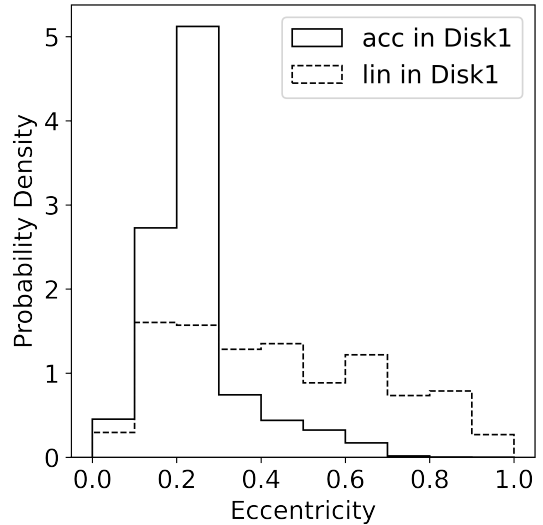


Figure 13. The eccentricity distribution for accelerating sources and non-accelerating sources on Disk1.

et al. (2009) reported a disk thickness of $\Delta_\theta = 7^\circ \pm 2^\circ$. Our intrinsic disk thickness of $\Delta_\theta = 7^\circ \pm 1^\circ$ is consistent with that found in previous work, only with smaller uncertainty.

The surface density profile in the plane of Disk1 is predicted to be $\Sigma(r) \propto r^{-2}$ for *in-situ* formation scenarios (Lin & Pringle 1987; Levin 2007) and has been verified in many observations (Paumard et al. 2006; Bartko et al. 2009; Lu et al. 2009; Yelda et al. 2014). In our paper, the semi-major axis a distribution was initially fit with methods similar to the eccentricity distribution as discussed in §5.2.1. However, the fit results were extremely uncertain and no significant constraint could be placed on the a distribution in the disk plane. We instead explore the distributions of projected radial distances on the disk plane. The slope of the radial profile (-1.80 ± 0.17 from Eq.20) is in agreement with the predicted -2 .

6.3. Plane2 Properties

In addition to the CW Disk1, we found a new CCW structure Plane2, which has 10 stars out of the total 88 young stars in our sample. We estimated that Plane2 has $(i, \Omega) = (90 \pm 20^\circ, 245 \pm 19^\circ)$, which is similar to the F3 structure reported in von Fellenberg et al. (2022). A more detailed comparison between these two structures is discussed in Appendix B.2 and B.3. As presented in §5.2.1, stars in Plane2 have relatively high eccentricities, with $\langle e \rangle = 0.68$. We also estimated the intrinsic disk thickness of Plane2 to be $\Delta_\theta = 18.6^\circ \pm 6.2^\circ$. The radial profile of Plane2 has a power law index of -1.43 ± 0.47 from Eq.20, which is inconsistent with the predicted -2 . This might be caused by the complex dynamical evo-

lution experienced by Plane2 stars such that they have high eccentricities with less steep radial profile. One of the most prominent feature of Plane2 is its spatial asymmetry. As discussed in §5.3, this asymmetric feature cannot be explained by differential extinction or incompleteness and is likely intrinsic to the structure.

6.4. Is Plane2 Related to the IRS 13 Group or G sources?

IRS 13 is a group of nearly co-moving massive young stars, clustered together at $3.5''$ to the West of the SMBH (Maillard et al. 2004; Paumard et al. 2006; Martins et al. 2007). It has been proposed to lie within the previously claimed CCW disk (Maillard et al. 2004; Schödel et al. 2005), but later works did not detect the CCW disk (Lu et al. 2009; Yelda et al. 2014), nor do we detect it in this work. Interestingly, one of IRS 13 group stars, IRS 13E1, is a potential Plane2 star, with a 50% probability being on Plane2. The remaining IRS 13 sources E2, E3, and E4, are currently not in our sample as they were excluded either due to their Wolf-Rayet star nature or the lack of published completeness information. Here we relax our requirement for a complete sample in order to identify other candidate Plane2 members; although we note that we cannot infer structural properties of Plane2 from this analysis.

Since all the IRS 13 stars are moving in approximately the similar direction, we run the same orbital and disk membership analysis for three other IRS 13 stars in addition to IRS 13E1. They are IRS 13E2, IRS 13E3, IRS 13E4. We use the most up-to-date radial velocities reported in Zhu et al. (2020). Note that using RV measurements from Paumard et al. (2006) and Bartko et al. (2009) generates similar results. The proper motions for IRS 13 stars are plotted in Figure 14 and the (i, Ω) density map is shown in Figure 15. Note that the nature of IRS 13E3 is not entirely clear – it may be a dusty star or a gas clump at the intersection of colliding winds (Zhu et al. 2020; Wang et al. 2019; Fritz et al. 2010) and the proper motion is quite uncertain (Tsuboi et al. 2022; Fritz et al. 2010). Nevertheless, we find that IRS 13E3 is a potential Plane2 star, with a disk membership probability $P_{\text{Plane2}} = 0.34$, but IRS 13E2 and IRS 13E4 are not on Plane2 with $P_{\text{Plane2}} < 10^{-2}$. Based on the posterior contours of IRS 13E2 and IRS13 E4 in the (i, Ω) plane, we think they are close to F1/CCW feature reported in von Fellenberg et al. (2022); however, they did not classify these two IRS13 stars as belonging to F1/CCW feature.

Even though all four IRS 13 stars are approximately moving in a similar direction on the sky, the dispersion in the proper motions of the stars is significant. Recent

studies of E1’s proper motion propose that this star may not be bound to the IRS13 group, while E2 and E4 are most likely bound to the group (Wang et al. 2019; Mužić et al. 2008). Additionally, studies of the spectrum of IRS 13E1 and E2 do not show signs of binarity (Fritz et al. 2010). The two different pairs (E1 & E3 and E2 & E4) are discrepant enough that they may not be associated with each other. Thus it is unclear whether Plane2 is related to the potentially bound IRS13 group given the low Plane2 membership probability for E2 & E4. Further study, including higher-resolution images and continued astrometric and RV monitoring will be needed to resolve the relationship between the apparently bound IRS 13 group and Plane2.

In order to include as many Plane2 stars as possible, we report all potential Plane2 stars based on our analysis of all 146 stars with reported RVs and proper motions, listed in Table 7. The potential Plane2 stars and their disk membership is reported in Table 6. A quiver plot showing the proper motion and RV for those potential Plane2 stars ($P_{\text{Plane2}} > 0.2$) is shown in Figure 16.

Table 6. Plane2 Summary

Name	P_{Plane2}	SA
S0-31	0.30	0.004
IRS 16NW	0.38	0.046
IRS 13E1	0.50	0.002
IRS 13E3	0.34	0.265
S4-258	0.40	0.093
S5-34	0.36	0.034
S5-106	0.34	0.029
S5-236	0.71	0.024
S9-114	0.52	0.063
S9-221	0.77	0.044
S10-185	0.73	0.132
S10-238	0.78	0.002
S12-5	1.00	0.003
S13-3	0.27	0.133
S0-16	0.42	0.001
S3-26	0.24	0.163
S8-196	0.22	0.142

A population of dust enshrouded objects are found to orbit around the SMBH: the so-called G sources. The most famous G source is G2, which first looked like a pure gas cloud (Gillessen et al. 2013; Eckart et al. 2013; Phifer et al. 2013), yet survived through closest approach to SgrA* in early 2014 (Gillessen et al. 2013; Abarca et al. 2014; Shcherbakov 2014; Witzel et al. 2014; Valencia-S. et al. 2015). This implies that G2 must con-

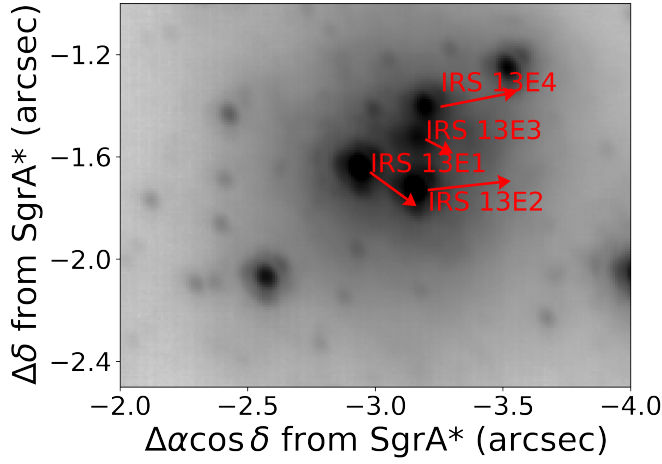


Figure 14. The proper motion for IRS 13 sources, where IRS 13E1 and IRS 13E3 are likely to be on Plane2 while IRS 13E2 and IRS 13E4 are not.

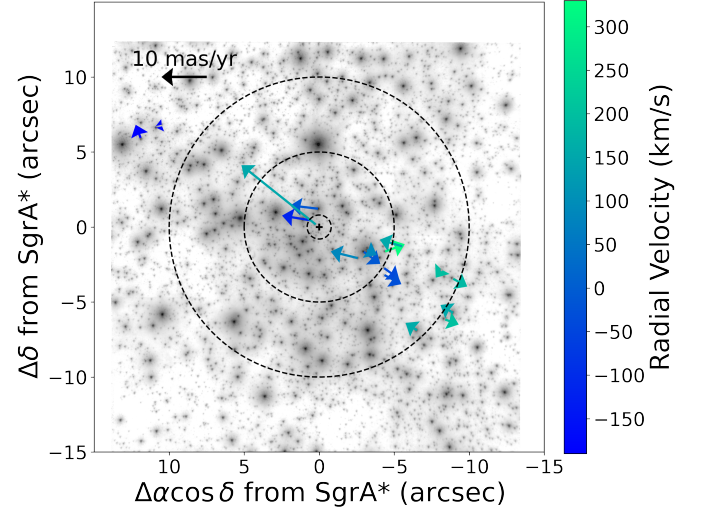


Figure 16. The quiver plot of all potential Plane2 stars, with color showing the RV.

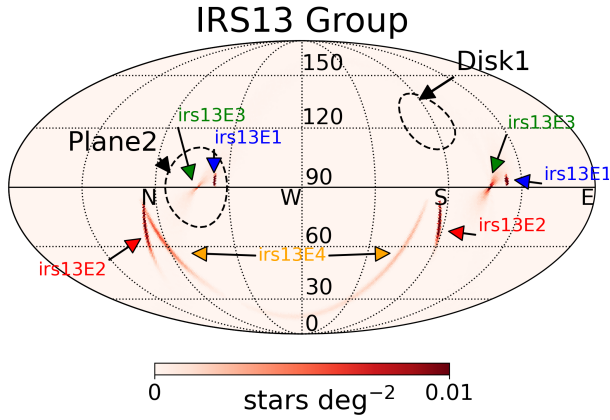


Figure 15. The (i, Ω) density map for IRS 13E1, IRS 13E2, IRS 13E3, IRS 13E4.

tain a stellar-like object and is perhaps a binary merge product. However, there is still no broad consensus as to the origin and nature of the G sources. Using the near-infrared (NIR) spectro-imaging data obtained over 13 years at the W. M. Keck Observatory with the

OSIRIS integral field spectrometer, Ciurlo et al. (2020) reported four more additional G sources, making the total number of G sources to six. Ciurlo et al. (2020) found the six G sources (G1, G2, G3, G4, G5 and G6) have widely varying orbits, suggesting G sources are formed separately. We compare the orbital plane direction for G sources with stellar disk plane and the individual G source (i, Ω) density map is plotted in Figure 17. The conclusion is that none of the G sources are likely to be on either Disk1 or Plane2. However G5 is also edge-on, and has almost exactly 180° difference in Ω compared to Plane2. In fact, there is a small probability of $P_{\text{Plane2}} = 0.08$ for G5 for its degenerate solution. In other words, G5 lies in the edge-on Plane2; but is counter-rotating in the plane.

6.5. The Star Formation Process

Besides the widely accepted *in-situ* formation theory, it has been suggested that an inspiraling star cluster to explain the formation of young stars in our GC, where a massive young cluster migrate towards the center of the galaxy under dynamical friction (Gerhard 2001). However, this scenario will deposit stars with a profile of $r^{-0.75}$, which is inconsistent with the observed density profile. So the fact that radial profile from §5.2 follows $P(r) \propto r^{-1.80}$ supports *in-situ* formation scenario.

Although we did not detect the counter-clockwise disk claimed in (Genzel et al. 2003; Paumard et al. 2006; Bartko et al. 2009), we found another almost edge-on

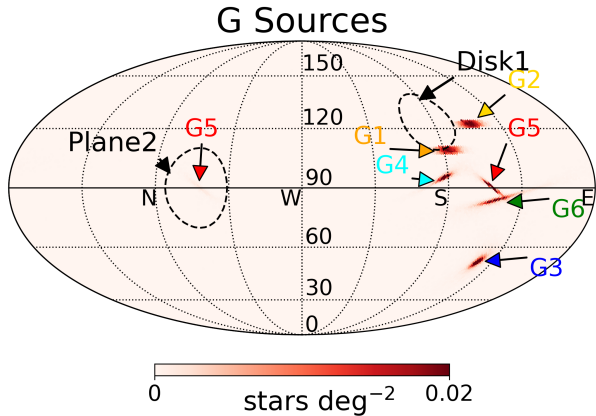


Figure 17. The (i, Ω) density map for G1, G2, G3, G4, G5, and G6. We do not have full posterior samples for G1 and G2 so we use their i , Ω , and associated uncertainty from (Witzel et al. 2017; Gillessen et al. 2019) to generate the 2D Gaussian distribution.

disk (Plane2 in this paper) with highly asymmetric stellar distribution. This edge-on disk is mostly determined by stars on the southwest side and very few stars on the northeast side are found in this disk. While the uneven distribution of stars on Plane2 is not fully understood, possible explanations include: (1) The young stellar population is not uniformly distributed within Plane2, with more stars in the southwest region compared to northeast region (see §5.3). One possible situation that could explain this asymmetry is the non-uniform initial gas distribution, leading to uneven star formation. (2) If Plane2 is indeed related to the IRS13 group, the possible explanations for the formation of IRS13 group can also be used to explain Plane2. For example, Plane2 might be a remnant stream from the disruption of an IRS 13 cluster that may or may not contain an intermediate-mass black hole (IMBH) (Maillard et al. 2004).

6.6. Biases Induced by Binaries

In our analysis of disk membership and disk properties, we assume that stars are not in binary systems. However, this may lead to biases in our results as presented by Naoz et al. (2018): if we ignore binaries, the disk memberships and disk fractions are likely to be biased to lower values; observed eccentricity and dispersion angle are likely to be biased to higher values.

Here we present an analysis of the influence of ignoring binaries on disk membership on each sub-structure, Disk1 and Plane2. We simulate a sample of stars drawn from each structure and generate 3D positions and velocities for each star based on the radial profile and eccentricity distribution presented in §5.2.1 and §5.2.2. Then we randomly assign each star as a binary or not based on the binary fraction of 70% as is appropriate for massive stars (Raghavan et al. 2010; Stephan et al. 2016). If a star is assigned to be in a binary system, we assign its binary properties, such as binary eccentricity, mass ratio, and inclination, drawn from distributions of massive star binary properties described in Sana et al. (2012). The primary stellar masses are sampled based on the IMF described in Lu et al. (2013).

These binary properties, combined with position and velocity data of stars, are used to calculate a proxy parameter β defined by Naoz et al. (2018), Eq 5. β is the apparent deflection angle from the true orbital plane around the SMBH if the binary RV is ignored. We follow a similar criterion used in Naoz et al. (2018) §3, where a star with $\beta > 11.2^\circ$ is considered as an on-disk star misidentified as an off-disk star. We simulate each structure 1000 times and calculate the mean fraction for $\beta > 11.2^\circ$, as shown in Figure 18.

We find that for Disk1, the misclassified disk fraction is 0.13 ± 0.08 and for Plane2 is 0.14 ± 0.1 . This implies that the presence of binaries should make $\sim 14\%$ of the on-disk stars appear as off-disk stars. Because we are ignoring binaries in our analysis, taking them into account would increase the Disk1 sample size from 18 stars to ~ 21 stars and Plane2 sample size from 10 stars to ~ 11 stars. Given this relatively small change in sample size, we think the bias induced by ignoring binaries is not significant if the binary fraction is 70%. However, binary RV surveys are needed to fully quantify the true binary fraction and the size of the bias.

In this section, we only calculate the bias on disk membership. Further analysis could be done to quantifying biases on eccentricity and disk dispersion angle, which can provide a more realistic set of disk properties.

7. SUMMARY

We analysed the dynamical structure of 88 young stars at the Galactic Center with projected radii from $0''$ to $15''$ with well measured proper motions, radial velocities and spectroscopic completeness information. This is the largest sample of GC young stars published with proper motion, radial velocity and completeness correction. We also simulate star clusters with different dynamical sub-structure to directly compare with what is actually observed on sky. We detect the well known

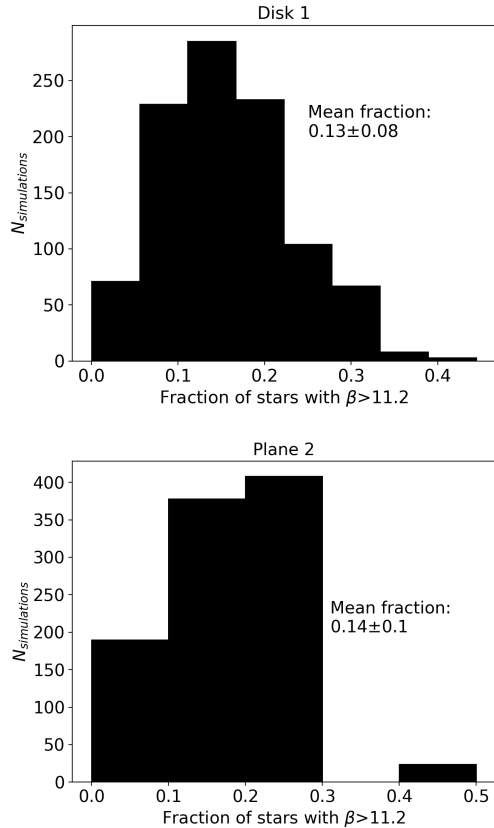


Figure 18. The fraction of misidentified off-disk stars when binaries are neglected. The histogram shows the fraction of stars with an angular difference in the input vs. output orbital plane (β) exceeding expected measurement errors, averaged over 1000 simulations, for Disk1 (top) and Plane2 (bottom). 10-20% of stars are likely misclassified as off-disk due to their binary nature.

clockwise disk (Disk1 in this paper), consistent with what has been previously published. We also find a second, almost edge-on, counter-clockwise disk (Plane2 in this paper). Plane2 is asymmetric with stars concentrated in the southwest direction, and two IRS 13 stars are found to potentially reside in this plane. By applying a hierarchical Bayesian inference framework, we calculate that Disk1 has an eccentricity peaking at 0.2 for sources with well-measured accelerations, consistent with previous analysis, but Plane2 is even more eccentric than Disk1, with $P(e) \propto e$. By simulating Disk1, Plane2 and Non-disk stars using the observed disk properties, we are able to reproduce observed density maps for Disk1 and the Non-disk stars, but the highly asymmetric structure in Plane2 can not be explained with a uniform disk and extinction alone. In the future, we will use this sample with known completeness correction to constrain the IMF for different dynamical subgroups,

which will greatly help us understand their formation history.

8. ACKNOWLEDGEMENTS

We thank the referee for a very quick, yet thorough report which helped to improve the paper. We also thank the staff of the W.M. Keck Observatory for all their help in obtaining observations. We acknowledge support from the W. M. Keck Foundation, the Heising Simons Foundation, and the National Science Foundation (AST-1412615, AST-1518273). M. W. Hosek Jr. also acknowledges support by Brinson Prize Fellowship. The W.M. Keck Observatory is operated as a scientific partnership among the California Institute of Technology, the University of California and the National Aeronautics and Space Administration. The Observatory was made possible by the generous financial support of the W. M. Keck Foundation. The authors wish to recognize and acknowledge the very significant cultural role and reverence that the summit of Maunakea has always had within the indigenous Hawaiian community. We are most fortunate to have the opportunity to conduct observations from this mountain.

Facilities: Keck Observatory

Software: AstroPy (Astropy Collaboration et al. 2013), Matplotlib (Hunter 2007), SciPy (Eric et al. 2001–)

APPENDIX

A. RADIAL VELOCITIES & PROPER MOTION DATA

Table 7. RVs Summary

Name	RV _{GCOWS} ^a (km s ⁻¹)	t _{0GCOWS}	ID _{P06}	RV _{P06} ^b (km s ⁻¹)	RV _{B09} ^c (km s ⁻¹)	ID _{F15}	RV _{F15} ^d (km s ⁻¹)	RV _{use} (km s ⁻¹)	ref ^e	WR	Data Available ^f
S0-20	261 ± 25*	2008.4	E3	-280 ± 50	–	–	–	multiple RVs	1	–	RV + C + PM
S0-2	-473 ± 27*	2002.4	E1	-1060 ± 25	–	–	–	multiple RVs	1	–	RV + C + PM
S0-1	-1054 ± 19*	2005.5	E4	-1033 ± 25	–	–	–	multiple RVs	1	–	RV + C + PM
S0-8	-389 ± 40*	2006.5	E7	-390 ± 70	–	–	–	multiple RVs	1	–	RV + C + PM
S0-16	139 ± 28*	2011.5	E2	300 ± 80	–	–	–	multiple RVs	1	–	RV + C + PM
S0-3	-709 ± 15*	2006.5	E6	-570 ± 40	–	–	–	multiple RVs	1	–	RV + C + PM
S0-5	631 ± 14*	2005.5	E9	610 ± 40	–	–	–	multiple RVs	1	–	RV + C + PM
S0-19	164 ± 46*	2006.5	E5	280 ± 50	–	–	–	multiple RVs	1	–	RV + C + PM
S0-11	-59 ± 29*	2006.5	E12	-20 ± 150	–	–	–	-22 ± 4	1	–	RV + C + PM
S0-7	72 ± 72*	2006.5	E11	160 ± 60	–	–	–	98 ± 5	1	–	RV + C + PM
S0-4	-2 ± 19*	2006.5	E10	15 ± 30	–	–	–	multiple RVs	1	–	RV + C + PM
S0-30	-16 ± 71	2008.4	–	–	–	–	–	-16 ± 71	1	–	RV + C + PM
S0-9	135 ± 20*	2005.5	–	–	–	–	–	95 ± 4	1	–	RV + C + PM
S0-31	-132 ± 30*	2006.5	E13	-890 ± 31	–	–	–	-120 ± 10	1	–	RV + C + PM
S0-14	-82 ± 21*	2006.5	E14	-14 ± 40	-75 ± 25	2233	-28 ± 104	-32 ± 2	1	–	RV + C + PM
S1-3	–	–	E15	68 ± 40	1 ± 33	562	110 ± 72	20 ± 30	3,4	–	RV + C + PM
S0-15	-738 ± 33*	2006.5	E16	-424 ± 70	-557 ± 26	–	–	-542 ± 4	1	–	RV + C + PM
S1-2	39 ± 32*	2006.5	E17	26 ± 30	–	–	–	-65 ± 8	1	–	RV + C + PM
S1-8	57 ± 48*	2006.5	E18	-364 ± 40	–	1619	102 ± 94	-112 ± 7	1	–	RV + C + PM
S1-4	–	–	–	–	–	668	-221 ± 179	-221 ± 179	4	–	RV + C + PM
S1-33	44 ± 23*	2006.5	–	–	–	–	–	26 ± 7	1	–	RV + C + PM
S1-22	–	–	E25	-224 ± 50	-235 ± 100	900	-229 ± 35	-230 ± 33	3,4	–	RV + C + PM
S1-19	-169 ± 16	2007.5	–	–	–	–	–	-169 ± 16	1	–	RV + C + PM
S1-24	125 ± 10	2008.4	E26	206 ± 30	206 ± 30	331	221 ± 45	125 ± 10	1	–	RV + C + PM
IRS 16CC	–	–	E27	241 ± 25	241 ± 25	64	256 ± 12	253 ± 11	2,3,4	–	RV + C + PM
S2-4	218 ± 6	2008.4	E28	286 ± 20	286 ± 20	443	229 ± 36	218 ± 6	1	–	RV + C + PM
S2-6	152 ± 8	2008.4	E30	216 ± 20	216 ± 20	–	–	152 ± 8	1	–	RV + C + PM
IRS 33N	23 ± 5	2007.5	E33	68 ± 20	63 ± 20	294	105 ± 61	23 ± 5	1	–	RV + C + PM
S2-50	-135 ± 32	2008.4	–	–	–	–	–	-135 ± 32	1	–	RV + C + PM
S2-17	57 ± 4	2008.4	E34	100 ± 20	100 ± 20	109	149 ± 27	57 ± 4	1	–	RV + C + PM
S2-21	-92 ± 12	2007.5	–	–	–	1534	-83 ± 42	-92 ± 12	1	–	RV + C + PM
S2-19	–	–	E36	41 ± 20	41 ± 20	941	157 ± 55	54 ± 19	2,3,4	–	RV + C + PM
S2-58	77 ± 16	2007.5	–	–	–	–	–	77 ± 16	1	–	RV + C + PM
S2-74	–	–	E38	36 ± 20	36 ± 20	1474	145 ± 72	44 ± 19	2,3,4	–	RV + C + PM
S3-3	23 ± 32	2015.6	–	–	–	–	–	23 ± 32	1	–	RV + C + PM
S3-96	-3 ± 24	2009.4	E42	40 ± 40	40 ± 40	–	–	-3 ± 24	1	–	RV + C + PM
S3-19	–	–	E43	-114 ± 50	-114 ± 50	507	-46 ± 57	-84 ± 38	2,3,4	–	RV + C + PM
S3-26	–	–	E45	63 ± 30	63 ± 30	725	117 ± 37	84 ± 23	2,3,4	–	RV + C + PM
S3-30	10 ± 17*	2008.4	E47	91 ± 30	56 ± 20	–	–	6 ± 15	1	–	RV + C + PM

Table 7 continued

Table 7 (continued)

Name	RV _{GCOWS} ^a (km s ⁻¹)	t _{0GCOWS}	ID _{P06}	RV _{P06} ^b (km s ⁻¹)	RV _{B09} ^c (km s ⁻¹)	ID _{F15}	RV _{F15} ^d (km s ⁻¹)	RV _{use} (km s ⁻¹)	ref ^e	WR	Data Available ^f
IRS 13E1	-10 ± 4	2009.4	E46	71 ± 20	71 ± 20	-	-	-10 ± 4	1	-	RV + C + PM
S3-190	-263 ± 22	2007.5	-	-	-	-	-	-262 ± 22	1	-	RV + C + PM
S3-331	-	-	E52	-167 ± 20	-167 ± 20	1892	-153 ± 60	-166 ± 19	2,3,4	-	RV + C + PM
S3-374	-	-	E53	29 ± 20	20 ± 20	847	52 ± 23	34 ± 15	3,4	-	RV + C + PM
S4-71	-	-	E55	76 ± 20	60 ± 50	785	104 ± 170	64 ± 48	3,4	-	RV + C + PM
S4-169	158 ± 44	2010.3	E57	196 ± 40	196 ± 40	-	-	158 ± 44	1	-	RV + C + PM
S4-262	41 ± 22	2010.3	-	-	-	-	-	41 ± 22	1	-	RV + C + PM
S4-314	154 ± 51	2010.3	-	-	-	-	-	154 ± 51	1	-	RV + C + PM
S4-364	-	-	E62	-134 ± 40	-134 ± 40	516	-46 ± 64	-109 ± 34	2,3,4	-	RV + C + PM
S5-106	-29 ± 17	2019.4	-	-	-	-	-	-29 ± 17	1	-	RV + C + PM
S5-237	42 ± 18	2010.3	-	-	-	-	-	42 ± 18	1	-	RV + C + PM
S5-183	-146 ± 17	2010.6	-	-	-135 ± 30	372	-148 ± 23	-146 ± 17	1	-	RV + C + PM
S5-191	127 ± 56	2010.6	-	-	140 ± 50	-	-	127 ± 56	1	-	RV + C + PM
S6-89	-	-	-	-	-135 ± 70	567	-120 ± 77	-128 ± 52	3,4	-	RV + C + PM
S6-96	-	-	-	-	-35 ± 50	973	133 ± 70	22 ± 41	3,4	-	RV + C + PM
S6-81	-22 ± 5	2010.3	E67	8 ± 20	8 ± 20	205	32 ± 16	-22 ± 5	1	-	RV + C + PM
S6-63	-	-	E69	153 ± 50	110 ± 50	227	154 ± 28	144 ± 24	3,4	-	RV + C + PM
S7-30	-35 ± 37	2010.4	-	-	-	-	-	-35 ± 37	1	-	RV + C + PM
S7-5	-	-	-	-	-	596	120 ± 52	120 ± 52	4	-	RV + C + PM
S7-10	-	-	E73	-92 ± 40	-92 ± 40	445	-61 ± 21	-68 ± 19	2,3,4	-	RV + C + PM
S7-216	-	-	-	-	60 ± 50	96	136 ± 17	128 ± 16	3,4	-	RV + C + PM
S7-236	-	-	-	-	-170 ± 70	838	78 ± 64	78 ± 64	4	-	RV + C + PM
S8-5	-	-	-	-	-	209	87 ± 31	87 ± 31	4	-	RV + C + PM
S8-4	-	-	E75	-138 ± 40	-138 ± 40	230	-114 ± 20	-119 ± 18	2,3,4	-	RV + C + PM
S8-196	-	-	-	-	190 ± 50	728	277 ± 166	197 ± 48	3,4	-	RV + C + PM
S8-10	-	-	-	-	-	721	-22 ± 44	-22 ± 44	4	-	RV + C + PM
S8-8	-	-	-	-	-	610	-217 ± 211	-217 ± 211	4	-	RV + C + PM
S8-126	-	-	-	-	-	718	9 ± 88	9 ± 88	4	-	RV + C + PM
S9-143	-	-	-	-	40 ± 100	958	46 ± 68	44 ± 56	3,4	-	RV + C + PM
S9-6	-	-	-	-	-	366	257 ± 135	257 ± 135	4	-	RV + C + PM
S9-221	-	-	-	-	-	757	184 ± 89	184 ± 89	4	-	RV + C + PM
S10-50	35 ± 43*	2010.4	-	-	-	-	-	70 ± 23	1	-	RV + C + PM
S10-4	-	-	E84	-250 ± 40	-250 ± 40	273	-165 ± 25	-189 ± 21	2,3,4	-	RV + C + PM
S10-32	146 ± 11	2010.4	-	-	-	-	-	146 ± 11	1	-	RV + C + PM
S10-185	-	-	-	-	-	617	202 ± 102	202 ± 102	4	-	RV + C + PM
S10-34	-107 ± 38	2010.6	-	-	-	-	-	-107 ± 38	1	-	RV + C + PM
S10-232	-	-	-	-	-	511	231 ± 124	231 ± 124	4	-	RV + C + PM
S10-238	-	-	-	-	-	166	154 ± 102	154 ± 102	4	-	RV + C + PM
S10-48	-285 ± 45	2013.4	E86	-205 ± 50	-	-	-	-285 ± 45	1	-	RV + C + PM
S11-147	-	-	-	-	-	1103	53 ± 92	53 ± 92	4	-	RV + C + PM
S11-21	-81 ± 13	2016.6	E87	-120 ± 30	-160 ± 70	-	-	-81 ± 13	1	-	RV + C + PM
S11-176	148 ± 69	2014.4	-	-	-	-	-	148 ± 69	1	-	RV + C + PM
S11-8	-	-	-	-	-	890	31 ± 45	31 ± 45	4	-	RV + C + PM
S11-214	-	-	-	-	-	853	257 ± 124	257 ± 124	4	-	RV + C + PM
S11-246	132 ± 18	2014.4	-	-	-	-	-	132 ± 18	1	-	RV + C + PM
S12-76	-159 ± 32	2013.4	E89	-100 ± 40	-	-	-	-159 ± 32	1	-	RV + C + PM

Table 7 continued

Table 7 (continued)

Name	RV _{GCOWS} ^a (km s ⁻¹)	t0 _{GCOWS}	ID _{P06}	RV _{P06} ^b (km s ⁻¹)	RV _{B09} ^c (km s ⁻¹)	ID _{F15}	RV _{F15} ^d (km s ⁻¹)	RV _{use} (km s ⁻¹)	ref ^e	WR	Data Available ^f
S12-178	-	-	-	-	-	722	268 ± 30	268 ± 30	4	-	RV + C + PM
S12-5	-	-	-	-	-	483	-180 ± 42	-180 ± 42	4	-	RV + C + PM
S14-196	-	-	-	-	-	2048	130 ± 52	130 ± 52	4	-	RV + C + PM
S7-180	-	-	-	-	120 ± 70	1554	222 ± 31	205 ± 28	3,4	-	RV + C
S8-70	-137 ± 66	2010.4	-	-	-	-	-	-137 ± 66	1	-	RV + C
S10-261	77 ± 19	2014.4	-	-	-	-	-	77 ± 19	1	-	RV + C
S0-26	-	-	E8	30 ± 90	-	-	-	30 ± 90	2	-	RV + PM
S1-1	-	-	-	-	536 ± 30	-	-	536 ± 30	3	-	RV + PM
IRS 16C	-	-	E20	125 ± 30	158 ± 40	-	-	158 ± 40	3	Y	RV + PM
IRS 16NW	-	-	E19	-44 ± 20	-15 ± 50	-	-	-15 ± 50	3	Y	RV + PM
S1-12	-	-	E21	-24 ± 30	8 ± 22	-	-	8 ± 22	3	-	RV + PM
S1-14	-	-	E22	-434 ± 50	-400 ± 100	-	-	-400 ± 100	3	-	RV + PM
IRS 16SW	-	-	E23	320 ± 40	470 ± 50	-	-	470 ± 50	3	Y	RV + PM
S1-21	-	-	E24	-344 ± 50	-277 ± 50	-	-	-277 ± 50	3	-	RV + PM
IRS 29N	-	-	E31	-190 ± 90	-190 ± 90	-	-	-190 ± 90	2,3	Y	RV + PM
S2-7	-	-	E29	-94 ± 50	-	-	-	-94 ± 50	2	-	RV + PM
IRS 16SW-E	-	-	E32	366 ± 70	366 ± 70	-	-	366 ± 70	2,3	Y	RV + PM
S2-22	-	-	-	-	49 ± 50	-	-	49 ± 50	3	-	RV + PM
S2-16	-	-	E35	-100 ± 70	-100 ± 70	-	-	-100 ± 70	2,3	Y	RV + PM
IRS 16NE	-	-	E39	-10 ± 20	-10 ± 20	-	-	-10 ± 20	2,3	Y	RV + PM
S3-5	-	-	E40	327 ± 100	327 ± 100	-	-	327 ± 100	2,3	Y	RV + PM
IRS 33E	-	-	E41	170 ± 20	170 ± 20	-	-	170 ± 20	2,3	Y	RV + PM
S3-25	-	-	E44	-114 ± 40	-84 ± 6	-	-	-84 ± 6	3	-	RV + PM
S3-10	-	-	E50	281 ± 20	305 ± 70	-	-	305 ± 70	3	-	RV + PM
IRS 13E4	-	-	E48	56 ± 70	56 ± 70	-	-	71 ± 6	5	Y	RV + PM
IRS 13E3	-	-	E49	87 ± 20	-	-	-	-34 ± 3	5	Y	RV + PM
IRS 13E2	-	-	E51	40 ± 40	40 ± 40	-	-	-46 ± 5	5	Y	RV + PM
S4-36	-	-	E54	-154 ± 25	-154 ± 25	-	-	-154 ± 25	2,3	-	RV + PM
IRS 34W	-	-	E56	-290 ± 30	-290 ± 30	-	-	-290 ± 30	2,3	Y	RV + PM
IRS 7SE	-	-	E59	-150 ± 100	-150 ± 100	-	-	-150 ± 100	2,3	Y	RV + PM
S4-258	-	-	E60	330 ± 80	330 ± 80	-	-	330 ± 80	2,3	Y	RV + PM
IRS 34NW	-	-	E61	-150 ± 30	-150 ± 30	-	-	-150 ± 30	2,3	Y	RV + PM
S5-34	-	-	-	-	-40 ± 70	-	-	-40 ± 70	3	-	RV + PM
IRS 1W	-	-	E63	35 ± 20	35 ± 20	-	-	35 ± 20	2,3	-	RV + PM
S5-235	-	-	-	-	-115 ± 50	-	-	-115 ± 50	3	-	RV + PM
S5-236	-	-	-	-	155 ± 50	-	-	155 ± 50	3	-	RV + PM
S5-187	-	-	-	-	10 ± 50	-	-	10 ± 50	3	-	RV + PM
S5-231	-	-	E64	40 ± 25	24 ± 25	-	-	24 ± 25	3	-	RV + PM
IRS 9W	-	-	E65	140 ± 50	140 ± 50	-	-	140 ± 50	2,3	Y	RV + PM
S6-90	-	-	E66	-350 ± 50	-350 ± 50	-	-	-350 ± 50	2,3	Y	RV + PM
S6-95	-	-	E68	-305 ± 100	-305 ± 100	-	-	-305 ± 100	2,3	Y	RV + PM
S6-93	-	-	E70	-80 ± 100	-80 ± 100	-	-	-80 ± 100	2,3	Y	RV + PM
S6-100	-	-	E71	-300 ± 150	-	-	-	-300 ± 150	2	Y	RV + PM
S6-82	-	-	E72	86 ± 100	86 ± 100	-	-	86 ± 100	2,3	-	RV + PM
S7-161	-	-	-	-	-120 ± 50	-	-	-120 ± 50	3	-	RV + PM
S7-16	-	-	-	-	160 ± 50	-	-	160 ± 50	3	-	RV + PM

Table 7 continued

Table 7 (*continued*)

Name	RV _{GCOWS} ^a (km s ⁻¹)	t0 _{GCOWS}	ID _{P06}	RV _{P06} ^b (km s ⁻¹)	RV _{B09} ^c (km s ⁻¹)	ID _{F15}	RV _{F15} ^d (km s ⁻¹)	RV _{use} (km s ⁻¹)	ref ^e	WR	Data Available ^f
S7-19	-	-	-	-	-65 ± 50	-	-	-65 ± 50	3	-	RV + PM
S7-20	-	-	-	-	-45 ± 50	-	-	-45 ± 50	3	-	RV + PM
S7-228	-	-	-	-	150 ± 30	-	-	150 ± 30	3	-	RV + PM
S8-15	-	-	-	-	-130 ± 50	-	-	-130 ± 50	3	-	RV + PM
S8-7	-	-	-	-	30 ± 100	-	-	30 ± 100	3	-	RV + PM
S8-181	-	-	E74	70 ± 70	70 ± 70	-	-	70 ± 70	2,3	Y	RV + PM
S9-20	-	-	E76	180 ± 80	180 ± 80	-	-	180 ± 80	2,3	Y	RV + PM
S9-23	-	-	E77	-155 ± 50	-185 ± 50	-	-	-185 ± 50	3	-	RV + PM
S9-13	-	-	-	-	-160 ± 50	-	-	-160 ± 50	3	-	RV + PM
S9-1	-	-	E78	-230 ± 100	-230 ± 100	-	-	-230 ± 100	2,3	Y	RV + PM
S9-114	-	-	E79	160 ± 30	160 ± 50	-	-	160 ± 50	3	Y	RV + PM
S9-283	-	-	E81	30 ± 70	30 ± 70	-	-	30 ± 70	2,3	Y	RV + PM
S9-9	-	-	E80	130 ± 100	130 ± 100	-	-	130 ± 100	2,3	Y	RV + PM
S10-136	-	-	E82	-70 ± 70	-70 ± 70	-	-	-70 ± 70	2,3	Y	RV + PM
S10-5	-	-	E83	-180 ± 70	-180 ± 70	-	-	-180 ± 70	2,3	Y	RV + PM
S10-7	-	-	E85	-150 ± 40	-150 ± 40	-	-	-150 ± 40	2,3	-	RV + PM
S11-5	-	-	E88	-65 ± 40	-65 ± 40	-	-	-65 ± 40	2,3	Y	RV + PM
S13-3	-	-	E90	-190 ± 40	-	-	-	-190 ± 40	2	-	RV + PM

^aRV measurements from our database.

Stars with multiple measurements in our database are marked with asterisks and only one of their measurements is shown here.

^bRV measurements from [Paumard et al. \(2006\)](#)

^cRV measurements from [Bartko et al. \(2009\)](#)

^dRV measurements from [Feldmeier-Krause et al. \(2015\)](#)

^eReference for final RV_{use} : 1 - database, 2 - P06([Paumard et al. 2006](#)), 3 - B09([Bartko et al. 2009](#)), 4 - F15([Feldmeier-Krause et al. 2015](#)), 5 - Z20([Zhu et al. 2020](#))

^fThe available data for each star: RV - Radial Velocity, C - spectral completeness, PM - proper motion. See details in 2.1. Our final sample of 88 stars has measurements of RV, proper motion and spectral completeness.

Table 8. Proper Motions Summary

Name	Kp	K _{pext} ^a	ar (km s ⁻¹ yr ⁻¹)	x0 ($''$)	y0 ($''$)	vx (mas yr ⁻¹)	vy (mas yr ⁻¹)	t0	source ^b
S0-20	15.7	16.1	-167.68 ± 17.25	0.162 ± 0.00665	0.096 ± 0.00824	32.32 ± 2.17	-8.66 ± 2.22	2011.3	1
S0-2	14.1	14.5	-111.17 ± 12.27	-0.029 ± 0.00213	0.160 ± 0.00390	-6.50 ± 0.91	-2.13 ± 1.54	2010.2	1
S0-1	14.7	15.2	-103.22 ± 2.09	0.111 ± 0.00076	-0.294 ± 0.00296	19.00 ± 0.32	-7.58 ± 1.39	2009.9	1
S0-8	15.8	16.1	-77.39 ± 2.75	-0.179 ± 0.00153	0.099 ± 0.00065	22.49 ± 1.02	-28.73 ± 0.34	2010.3	1
S0-16	15.3	15.8	-41.50 ± 15.75	0.230 ± 0.00586	0.171 ± 0.00234	16.51 ± 2.12	13.17 ± 1.63	2008.0	1
S0-3	14.5	14.9	-43.15 ± 1.09	0.340 ± 0.00115	0.114 ± 0.00034	7.62 ± 0.58	-1.71 ± 0.16	2009.8	1
S0-5	15.1	15.6	-62.51 ± 0.82	0.170 ± 0.00083	-0.359 ± 0.00175	-3.48 ± 0.39	2.49 ± 0.80	2009.8	1
S0-19	15.5	15.9	-59.35 ± 1.77	-0.007 ± 0.00037	0.400 ± 0.00201	8.52 ± 0.10	16.10 ± 0.98	2009.7	1

Table 8 continued

Table 8 (continued)

Name	Kp	Kp _{ext} ^a	ar (km s ⁻¹ yr ⁻¹)	x0 ($''$)	y0 ($''$)	vx (mas yr ⁻¹)	vy (mas yr ⁻¹)	t0	source ^b
S0-11	15.1	15.5	0.50 ± 0.25	0.490 ± 0.00006	-0.066 ± 0.00010	-3.53 ± 0.02	-2.66 ± 0.05	2011.3	1
S0-7	15.4	15.8	-1.47 ± 0.46	0.516 ± 0.00007	0.099 ± 0.00006	5.86 ± 0.02	0.66 ± 0.02	2010.6	1
S0-4	14.3	14.7	-26.62 ± 0.29	0.442 ± 0.00068	-0.329 ± 0.00052	10.06 ± 0.33	-10.77 ± 0.22	2009.7	1
S0-30	16.1	16.7	3.19 ± 4.84	-0.513 ± 0.00012	-0.379 ± 0.00009	-10.61 ± 0.06	3.27 ± 0.09	2009.1	1
S0-9	14.2	14.8	-0.33 ± 0.22	0.226 ± 0.00005	-0.605 ± 0.00006	8.99 ± 0.02	-5.39 ± 0.02	2010.1	1
S0-31	15.1	15.5	-0.31 ± 0.36	0.565 ± 0.00007	0.445 ± 0.00006	6.37 ± 0.02	1.05 ± 0.02	2009.7	1
S0-14	13.7	14.3	0.09 ± 0.11	-0.756 ± 0.00003	-0.287 ± 0.00003	2.45 ± 0.01	-1.47 ± 0.01	2010.4	1
S1-3	12.1	12.5	-5.57 ± 0.14	0.339 ± 0.00008	0.882 ± 0.00019	-14.01 ± 0.03	1.40 ± 0.08	2009.1	1
S0-15	13.6	14.1	-11.81 ± 0.39	-0.965 ± 0.00043	0.182 ± 0.00007	-2.43 ± 0.15	-11.76 ± 0.03	2009.8	1
S1-2	14.8	15.4	-3.38 ± 0.21	0.077 ± 0.00005	-1.019 ± 0.00009	13.17 ± 0.02	-0.29 ± 0.04	2010.1	1
S1-8	14.2	14.7	-0.70 ± 0.13	-0.581 ± 0.00003	-0.920 ± 0.00003	9.26 ± 0.01	-5.69 ± 0.01	2010.3	1
S1-4	12.6	13.0	-6.53 ± 0.23	0.858 ± 0.00019	-0.664 ± 0.00014	11.31 ± 0.06	2.87 ± 0.08	2007.7	1
S1-33	14.9	15.5	0.65 ± 0.26	-1.245 ± 0.00005	0.002 ± 0.00005	-0.15 ± 0.02	5.17 ± 0.01	2011.0	1
S1-22	12.6	13.1	0.42 ± 0.18	-1.567 ± 0.00004	-0.524 ± 0.00003	8.25 ± 0.01	-3.26 ± 0.01	2010.2	1
S1-19	13.6	14.3	-0.41 ± 0.26	0.435 ± 0.00007	-1.639 ± 0.00008	8.54 ± 0.02	-3.38 ± 0.02	2010.3	1
S1-24	11.5	12.1	0.69 ± 0.08	0.736 ± 0.00002	-1.655 ± 0.00002	2.69 ± 0.01	-6.58 ± 0.01	2010.3	1
IRS 16CC	10.7	11.0	-3.64 ± 2.44	1.996 ± 0.00016	0.548 ± 0.00023	-1.51 ± 0.09	6.53 ± 0.07	2002.2	1
S2-4	12.1	12.6	-0.24 ± 0.11	1.521 ± 0.00004	-1.458 ± 0.00003	8.14 ± 0.01	2.80 ± 0.01	2010.3	1
S2-6	12.0	12.5	-0.83 ± 0.10	1.663 ± 0.00004	-1.334 ± 0.00004	8.04 ± 0.01	2.10 ± 0.01	2010.2	1
IRS 33N	11.3	12.0	0.19 ± 0.13	-0.026 ± 0.00002	-2.245 ± 0.00002	3.64 ± 0.01	-5.97 ± 0.01	2010.6	1
S2-50	15.4	15.9	-2.46 ± 0.70	1.701 ± 0.00020	-1.506 ± 0.00021	1.98 ± 0.05	2.04 ± 0.05	2010.0	1
S2-17	10.7	11.4	0.01 ± 0.30	1.340 ± 0.00004	-1.878 ± 0.00003	9.19 ± 0.01	-0.20 ± 0.01	2009.6	1
S2-21	13.4	13.9	-0.47 ± 0.15	-1.612 ± 0.00004	-1.676 ± 0.00003	9.54 ± 0.01	-3.85 ± 0.01	2010.7	1
S2-19	12.6	13.0	-0.90 ± 0.26	0.377 ± 0.00003	2.307 ± 0.00004	-8.18 ± 0.01	0.78 ± 0.01	2010.5	1
S2-58	14.1	14.4	0.50 ± 0.20	2.145 ± 0.00007	-1.125 ± 0.00006	-0.81 ± 0.02	6.43 ± 0.02	2010.4	1
S2-74	13.2	13.6	-0.07 ± 0.17	0.111 ± 0.00001	2.779 ± 0.00003	-8.67 ± 0.01	1.10 ± 0.01	2010.6	1
S3-3	15.1	15.4	0.52 ± 0.15	3.093 ± 0.00002	-0.640 ± 0.00005	3.68 ± 0.01	4.11 ± 0.02	2010.9	1
S3-96	14.3	14.9	1.62 ± 1.56	-3.131 ± 0.00016	-0.625 ± 0.00012	-0.02 ± 0.06	5.20 ± 0.07	2010.5	1
S3-19	11.9	12.8	-1.62 ± 1.05	-1.555 ± 0.00005	-2.795 ± 0.00004	8.00 ± 0.02	-1.76 ± 0.02	2009.0	1
S3-26	12.3	13.0	0.42 ± 0.17	-2.569 ± 0.00003	-2.071 ± 0.00002	5.99 ± 0.01	1.47 ± 0.01	2010.7	1
S3-30	12.4	13.3	0.08 ± 0.17	1.660 ± 0.00003	-2.933 ± 0.00003	-0.80 ± 0.01	4.00 ± 0.01	2010.7	1
IRS 13E1	10.6	11.3	0.27 ± 0.17	-2.979 ± 0.00003	-1.660 ± 0.00002	-3.65 ± 0.01	-2.66 ± 0.01	2010.5	1
S3-190	14.0	14.5	-0.32 ± 0.28	-3.191 ± 0.00004	1.410 ± 0.00005	-2.80 ± 0.01	-3.06 ± 0.02	2010.6	1
S3-331	13.5	13.8	0.71 ± 0.55	-1.224 ± 0.00005	3.655 ± 0.00008	5.96 ± 0.02	4.23 ± 0.02	2010.4	1
S3-374	12.3	12.9	-0.14 ± 0.15	-2.756 ± 0.00004	-2.855 ± 0.00002	-0.28 ± 0.01	-4.39 ± 0.01	2010.8	1
S4-71	12.3	13.2	0.27 ± 0.20	0.771 ± 0.00003	-4.095 ± 0.00004	0.08 ± 0.01	-4.60 ± 0.01	2010.8	1
S4-169	13.5	13.7	-1.11 ± 0.19	4.411 ± 0.00004	0.278 ± 0.00004	-2.53 ± 0.01	3.97 ± 0.01	2010.4	1
S4-262	16.2	16.7	0.35 ± 0.21	4.276 ± 0.00002	-1.964 ± 0.00004	-1.40 ± 0.01	-5.44 ± 0.01	2011.4	1
S4-314	15.3	15.8	-0.64 ± 0.29	4.409 ± 0.00004	-2.031 ± 0.00005	-0.13 ± 0.02	2.26 ± 0.02	2010.5	1
S4-364	11.7	12.1	–	2.248 ± 0.00016	4.464 ± 0.00021	6.86 ± 0.04	-2.97 ± 0.06	2011.1	2
S5-106	15.5	16.2	-1.51 ± 0.53	-4.351 ± 0.00008	-3.200 ± 0.00008	-3.77 ± 0.02	-2.04 ± 0.02	2011.5	1
S5-237	13.2	13.6	-3.92 ± 2.66	5.493 ± 0.00025	1.022 ± 0.00031	-1.31 ± 0.14	6.19 ± 0.12	2012.2	1
S5-183	11.6	12.2	-0.46 ± 0.11	4.591 ± 0.00002	-3.444 ± 0.00002	-4.52 ± 0.01	-2.13 ± 0.01	2010.4	1
S5-191	12.8	13.6	0.42 ± 0.18	3.181 ± 0.00002	-4.889 ± 0.00003	-1.52 ± 0.01	-3.78 ± 0.01	2010.7	1
S6-89	12.0	12.8	-3.43 ± 2.14	5.450 ± 0.00031	2.994 ± 0.00016	2.88 ± 0.10	-6.45 ± 0.06	2011.3	1
S6-96	12.8	13.1	–	-6.049 ± 0.00050	-1.923 ± 0.00052	-0.80 ± 0.12	7.28 ± 0.15	2010.3	2

Table 8 continued

Table 8 (continued)

Name	Kp	K _{Pext} ^a	ar (km s ⁻¹ yr ⁻¹)	x0 ($''$)	y0 ($''$)	vx (mas yr ⁻¹)	vy (mas yr ⁻¹)	t0	source ^b
S6-81	11.0	11.6	–	6.353 ± 0.00020	0.272 ± 0.00023	-2.69 ± 0.05	5.06 ± 0.05	2010.3	2
S6-63	11.2	12.1	1.53 ± 1.11	1.872 ± 0.00007	-6.305 ± 0.00014	5.85 ± 0.02	1.66 ± 0.04	2011.1	1
S7-30	13.9	14.7	–	6.460 ± 0.00020	-2.702 ± 0.00024	-3.01 ± 0.04	-3.92 ± 0.06	2011.5	2
S7-5	12.2	12.9	0.16 ± 1.01	4.860 ± 0.00010	-5.522 ± 0.00008	2.45 ± 0.05	5.24 ± 0.04	2010.5	1
S7-10	11.4	11.7	–	-1.117 ± 0.00024	7.622 ± 0.00031	-4.47 ± 0.04	-2.30 ± 0.07	2011.3	2
S7-216	10.7	11.0	–	-7.747 ± 0.00031	1.456 ± 0.00039	2.20 ± 0.08	5.71 ± 0.10	2015.5	3
S7-236	12.5	12.8	–	-7.142 ± 0.00018	3.562 ± 0.00021	-2.54 ± 0.04	-4.04 ± 0.02	2015.5	3
S8-5	11.1	11.9	–	-3.480 ± 0.00018	-7.506 ± 0.00025	-1.10 ± 0.06	4.55 ± 0.07	2011.1	2
S8-4	11.0	11.3	–	-0.021 ± 0.00024	8.564 ± 0.00025	-0.42 ± 0.06	3.56 ± 0.06	2011.3	2
S8-196	12.4	12.7	–	-8.111 ± 0.00021	-2.914 ± 0.00031	1.14 ± 0.05	-1.55 ± 0.07	2015.5	3
S8-10	12.2	12.5	–	6.962 ± 0.00018	5.190 ± 0.00025	3.28 ± 0.04	-3.07 ± 0.08	2011.1	2
S8-8	12.1	12.8	–	5.257 ± 0.00023	-7.069 ± 0.00017	0.29 ± 0.08	0.75 ± 0.06	2011.5	2
S8-126	12.5	13.2	–	-2.240 ± 0.00034	-8.564 ± 0.00024	-4.73 ± 0.15	2.53 ± 0.08	2011.1	2
S9-143	12.6	12.8	–	-8.389 ± 0.00018	-3.378 ± 0.00030	0.59 ± 0.04	-2.85 ± 0.07	2015.5	3
S9-6	11.4	12.2	–	0.760 ± 0.00028	-9.326 ± 0.00033	1.50 ± 0.10	1.62 ± 0.10	2010.8	2
S9-221	12.1	12.3	–	-8.936 ± 0.00014	-3.453 ± 0.00029	-3.12 ± 0.02	-1.72 ± 0.06	2015.5	3
S10-50	14.7	15.6	–	9.583 ± 0.00052	-3.182 ± 0.00034	-0.78 ± 0.13	-4.04 ± 0.08	2011.8	2
S10-4	11.2	11.5	–	0.071 ± 0.00032	10.251 ± 0.00029	-1.93 ± 0.07	1.13 ± 0.07	2011.3	2
S10-32	14.4	14.9	–	10.208 ± 0.00023	-1.689 ± 0.00031	2.72 ± 0.07	3.47 ± 0.07	2011.6	2
S10-185	12.2	12.4	–	-8.399 ± 0.00054	-6.164 ± 0.00023	-3.01 ± 0.15	-1.11 ± 0.03	2015.5	3
S10-34	14.5	15.4	–	8.878 ± 0.00039	-5.622 ± 0.00034	0.74 ± 0.10	3.47 ± 0.07	2011.2	2
S10-232	11.9	12.4	–	-7.056 ± 0.00026	-7.934 ± 0.00029	2.01 ± 0.06	-3.20 ± 0.06	2015.5	3
S10-238	10.9	11.3	–	-8.927 ± 0.00017	-5.720 ± 0.00022	2.81 ± 0.03	1.75 ± 0.03	2015.5	3
S10-48	15.1	15.3	–	-0.525 ± 0.00042	10.729 ± 0.00048	1.92 ± 0.08	0.81 ± 0.13	2011.5	2
S11-147	12.8	13.2	–	-10.751 ± 0.00038	-3.053 ± 0.00059	-0.20 ± 0.09	3.79 ± 0.15	2015.5	3
S11-21	13.5	13.8	–	2.559 ± 0.00022	10.932 ± 0.00034	-1.82 ± 0.05	-2.45 ± 0.08	2011.4	2
S11-176	15.3	16.0	–	-0.185 ± 0.00034	-11.214 ± 0.00053	-1.19 ± 0.09	2.21 ± 0.13	2015.5	3
S11-8	12.6	12.8	–	10.876 ± 0.00014	3.246 ± 0.00021	-1.70 ± 0.03	-2.98 ± 0.05	2010.7	2
S11-214	12.4	13.1	–	1.539 ± 0.00018	-11.284 ± 0.00022	-1.10 ± 0.04	-0.43 ± 0.03	2015.5	3
S11-246	14.2	14.9	–	-0.992 ± 0.00024	-11.567 ± 0.00029	-3.30 ± 0.06	-1.56 ± 0.06	2015.5	3
S12-76	14.5	15.1	–	0.018 ± 0.00049	12.285 ± 0.00101	2.84 ± 0.11	1.43 ± 0.28	2011.3	2
S12-178	12.2	13.0	–	-6.096 ± 0.00016	-10.875 ± 0.00021	-0.01 ± 0.03	-2.06 ± 0.02	2015.5	3
S12-5	11.6	11.9	–	10.891 ± 0.00014	6.671 ± 0.00029	0.17 ± 0.04	-0.04 ± 0.09	2011.3	2
S14-196	15.8	16.5	–	-10.924 ± 0.00073	-9.937 ± 0.00105	0.33 ± 0.19	2.98 ± 0.26	2015.5	3
S7-180	13.4	13.5	–	–	–	–	–	–	–
S8-70	15.3	15.7	–	–	–	–	–	–	–
S10-261	14.6	15.4	–	–	–	–	–	–	–
S0-26	15.3	15.7	21.29 ± 17.59	0.334 ± 0.00152	0.217 ± 0.00034	-3.08 ± 1.10	9.02 ± 0.26	2007.9	1
S1-1	13.1	13.3	-0.20 ± 0.09	1.038 ± 0.00004	0.032 ± 0.00003	5.90 ± 0.01	1.24 ± 0.01	2009.5	1
IRS 16C	9.9	10.3	-2.45 ± 0.22	1.050 ± 0.00013	0.549 ± 0.00012	-8.85 ± 0.04	7.49 ± 0.03	2009.6	1
IRS 16NW	10.1	10.6	–	0.078 ± 0.00005	1.219 ± 0.00004	6.16 ± 0.01	0.74 ± 0.01	2009.8	1
S1-12	13.6	14.0	-0.16 ± 0.11	-0.744 ± 0.00003	-1.031 ± 0.00002	11.44 ± 0.01	-2.97 ± 0.01	2010.6	1
S1-14	12.7	13.4	-1.48 ± 0.11	-1.308 ± 0.00005	-0.389 ± 0.00004	5.58 ± 0.02	-8.03 ± 0.02	2011.8	1
IRS 16SW	10.1	10.6	-3.73 ± 0.17	1.116 ± 0.00016	-0.949 ± 0.00016	7.61 ± 0.06	2.84 ± 0.05	2010.5	1
S1-21	13.2	13.7	-0.15 ± 0.24	-1.638 ± 0.00004	0.089 ± 0.00003	4.30 ± 0.01	-5.37 ± 0.01	2010.5	1
IRS 29N	10.5	11.1	1.33 ± 0.84	-1.548 ± 0.00011	1.361 ± 0.00011	4.99 ± 0.04	-5.53 ± 0.04	2011.3	1

Table 8 continued

Table 8 (continued)

Name	Kp	Kp _{ext} ^a	ar (km s ⁻¹ yr ⁻¹)	x0 (")	y0 (")	vx (mas yr ⁻¹)	vy (mas yr ⁻¹)	t0	source ^b
S2-7	14.2	14.6	0.14 ± 0.26	0.926 ± 0.00003	1.851 ± 0.00003	-6.72 ± 0.01	1.48 ± 0.01	2010.4	1
IRS 16SW-E	11.1	11.5	-1.37 ± 0.26	1.903 ± 0.00005	-1.113 ± 0.00010	5.95 ± 0.02	3.76 ± 0.03	2011.3	1
S2-22	12.9	13.2	-2.26 ± 0.28	2.306 ± 0.00010	-0.225 ± 0.00005	-1.60 ± 0.05	6.10 ± 0.03	2007.0	1
S2-16	12.0	12.4	0.44 ± 0.38	-1.074 ± 0.00004	2.057 ± 0.00005	-8.89 ± 0.01	-1.16 ± 0.02	2010.5	1
IRS 16NE	9.1	9.2	-0.62 ± 1.54	2.895 ± 0.00028	0.953 ± 0.00030	2.92 ± 0.08	-9.30 ± 0.10	2010.3	1
S3-5	12.0	12.4	-0.60 ± 0.11	2.961 ± 0.00002	-1.149 ± 0.00003	2.74 ± 0.01	4.59 ± 0.01	2010.5	1
IRS 33E	10.2	11.0	-0.38 ± 0.31	0.710 ± 0.00004	-3.138 ± 0.00005	6.84 ± 0.01	-1.31 ± 0.02	2010.7	1
S3-25	13.9	14.2	-0.36 ± 0.18	1.405 ± 0.00003	2.954 ± 0.00003	-7.02 ± 0.01	0.35 ± 0.01	2010.3	1
S3-10	12.1	12.6	-0.78 ± 0.14	3.339 ± 0.00003	-1.106 ± 0.00002	-0.33 ± 0.01	5.16 ± 0.01	2010.5	1
IRS 13E4	11.7	12.4	1.82 ± 0.71	-3.256 ± 0.00026	-1.404 ± 0.00027	-5.94 ± 0.06	1.16 ± 0.07	2012.5	1
IRS 13E3	12.4	13.1	-2.96 ± 8.22	-3.196 ± 0.00120	-1.531 ± 0.00177	-2.16 ± 0.32	-1.11 ± 0.46	2009.9	1
IRS 13E2	10.7	11.3	-0.03 ± 0.18	-3.206 ± 0.00003	-1.730 ± 0.00002	-6.49 ± 0.01	0.71 ± 0.01	2010.4	1
S4-36	12.6	12.8	0.39 ± 0.36	-3.695 ± 0.00005	1.777 ± 0.00007	-4.88 ± 0.02	-4.65 ± 0.02	2010.1	1
IRS 34W	11.4	11.6	0.64 ± 0.42	-4.070 ± 0.00006	1.551 ± 0.00006	-2.14 ± 0.02	-5.65 ± 0.02	2010.2	1
IRS 7SE	13.1	13.5	2.26 ± 0.83	2.991 ± 0.00007	3.464 ± 0.00016	5.94 ± 0.02	-0.11 ± 0.05	2009.8	1
S4-258	12.6	13.0	-0.29 ± 0.26	-4.402 ± 0.00005	-1.632 ± 0.00002	-4.34 ± 0.02	1.62 ± 0.01	2010.1	1
IRS 34NW	13.3	13.6	-0.75 ± 0.70	-3.780 ± 0.00006	2.823 ± 0.00008	-5.43 ± 0.02	-4.04 ± 0.03	2010.4	1
S5-34	13.6	14.3	-0.49 ± 0.32	-4.336 ± 0.00005	-2.744 ± 0.00005	-3.31 ± 0.02	-2.40 ± 0.01	2010.5	1
IRS 1W	10.9	11.3	6.99 ± 5.12	5.252 ± 0.00066	0.636 ± 0.00252	-1.22 ± 0.41	6.66 ± 0.85	2012.8	1
S5-235	13.2	13.6	–	2.779 ± 0.00020	4.532 ± 0.00020	-0.79 ± 0.04	-4.06 ± 0.05	2011.5	2
S5-236	13.1	13.4	–	-5.535 ± 0.00036	-1.287 ± 0.00041	4.97 ± 0.11	1.48 ± 0.14	2010.7	2
S5-187	13.2	14.1	-0.62 ± 0.64	-1.711 ± 0.00008	-5.546 ± 0.00011	-0.92 ± 0.03	-4.11 ± 0.04	2009.7	1
S5-231	12.0	12.4	–	5.813 ± 0.00018	0.115 ± 0.00018	-0.14 ± 0.04	6.51 ± 0.04	2012.0	2
IRS 9W	12.1	12.9	-0.25 ± 0.40	2.899 ± 0.00003	-5.589 ± 0.00004	5.40 ± 0.01	3.45 ± 0.02	2010.3	1
S6-90	12.3	12.6	–	-3.951 ± 0.00026	4.906 ± 0.00027	0.28 ± 0.06	-3.80 ± 0.07	2011.3	2
S6-95	13.2	13.1	–	-2.401 ± 0.00023	5.998 ± 0.00035	5.34 ± 0.05	0.07 ± 0.09	2011.3	2
S6-93	12.8	13.4	–	4.467 ± 0.00020	4.960 ± 0.00022	5.08 ± 0.04	-1.31 ± 0.06	2011.6	2
S6-100	13.9	14.1	–	1.548 ± 0.00036	6.525 ± 0.00125	-4.46 ± 0.11	3.20 ± 0.50	2010.8	2
S6-82	13.5	14.1	–	6.722 ± 0.00022	-0.458 ± 0.00047	1.67 ± 0.07	4.90 ± 0.16	2011.3	2
S7-161	13.6	13.8	–	-7.420 ± 0.00018	0.033 ± 0.00070	-2.08 ± 0.04	-3.61 ± 0.19	2015.5	3
S7-16	12.5	13.4	–	1.629 ± 0.00019	-7.227 ± 0.00019	2.08 ± 0.06	3.62 ± 0.06	2011.3	2
S7-19	13.2	13.6	–	-3.774 ± 0.00022	6.512 ± 0.00033	5.27 ± 0.06	3.04 ± 0.08	2011.3	2
S7-20	13.3	13.6	–	-3.683 ± 0.00025	6.956 ± 0.00036	5.10 ± 0.05	2.40 ± 0.09	2011.2	2
S7-228	11.8	12.2	–	-7.756 ± 0.00018	1.721 ± 0.00055	2.68 ± 0.04	2.67 ± 0.15	2015.5	3
S8-15	13.0	13.2	–	-1.611 ± 0.00026	8.027 ± 0.00033	-2.91 ± 0.05	-3.12 ± 0.09	2011.3	2
S8-7	11.9	12.7	–	-3.673 ± 0.00019	-7.422 ± 0.00025	4.55 ± 0.05	-0.44 ± 0.07	2011.1	2
S8-181	11.6	11.8	–	-7.660 ± 0.00020	-3.613 ± 0.00029	-1.41 ± 0.05	-3.47 ± 0.06	2015.5	3
S9-20	13.2	14.0	–	4.315 ± 0.00036	-8.032 ± 0.00023	2.35 ± 0.13	0.84 ± 0.07	2011.7	2
S9-23	13.6	13.7	–	-1.285 ± 0.00037	9.134 ± 0.00052	-2.64 ± 0.11	-2.84 ± 0.17	2011.6	2
S9-13	13.1	13.1	–	-3.012 ± 0.00022	8.823 ± 0.00040	2.67 ± 0.05	3.27 ± 0.09	2011.0	2
S9-1	12.7	12.9	–	9.444 ± 0.00017	0.269 ± 0.00018	-2.55 ± 0.03	-2.99 ± 0.09	2010.4	2
S9-114	10.8	11.2	–	-6.519 ± 0.00016	-6.882 ± 0.00024	2.54 ± 0.03	1.64 ± 0.04	2015.5	3
S9-283	12.5	12.9	–	-9.622 ± 0.00064	-2.555 ± 0.00030	1.91 ± 0.19	-1.14 ± 0.07	2015.5	3
S9-9	11.7	12.5	–	5.649 ± 0.00016	-8.192 ± 0.00018	-1.11 ± 0.04	-2.00 ± 0.06	2010.7	2
S10-136	13.0	13.1	–	-8.665 ± 0.00037	-5.268 ± 0.00046	-1.79 ± 0.10	4.04 ± 0.12	2015.5	3
S10-5	11.9	12.2	–	-1.578 ± 0.00030	10.027 ± 0.00040	-1.17 ± 0.07	-1.73 ± 0.10	2011.3	2

Table 8 continued

Table 8 (*continued*)

Name	Kp	K _{Pext} ^a	ar	x0	y0	vx	vy	t0	source ^b
			(km s ⁻¹ yr ⁻¹)	($''$)	($''$)	(mas yr ⁻¹)	(mas yr ⁻¹)		
S10-7	12.7	13.1	–	9.709 ± 0.00016	4.409 ± 0.00037	-0.56 ± 0.04	-4.34 ± 0.12	2010.8	2
S11-5	11.8	12.4	–	1.367 ± 0.00023	11.695 ± 0.00029	-0.52 ± 0.04	2.22 ± 0.07	2011.4	2
S13-3	11.9	12.2	–	11.902 ± 0.00012	5.936 ± 0.00029	1.09 ± 0.02	2.93 ± 0.09	2011.4	2

^aExtinction corrected Kp to Aks=2.7

^bReference for final proper motion: 1 - central 10 $''$, 2 - maser mosaic, 3 - HST

B. COMPARISON TO THE VON FELLEBERG ET AL. 2022 WORK

In following sections, we compare our data set with the one used in von Fellenberg et al. (2022), where they reported a total of 5 dynamical structures, including the CCW feature that we consider insignificant. In total, their work includes a sample of 195 stars from a $\sim 30'' \times 30''$ spectroscopic survey of the GC, and they report 95 stars belonging to 5 features: Inner Clockwise Disk (CW1), Outer Clockwise Disk (CW2), Counterclockwise Disk/Filament (CCW/F1), Outer Filament 2 (F2), and Outer Filament 3 (F3). Our data set has a total of 88 stars extending to $\sim 14''$, where we find 28 stars belonging to Disk1 and Plane2.

While the two works agree on the clockwise disk (CW1_{F22} = Disk1) and nearly agree on a new filament (F3_{F22} = Plane2), we do not find the other structural features rise to significance in our data set. As explained in Appendix B.2, the discrepancy is likely caused by several factors such as differences in the measured proper motions, radial velocities, and sample of stars used.

In Appendix B.1 we compare proper motions, in Appendix B.2 we discuss differences between how the significance of dynamical features are calculated, and finally in Appendix B.3 we analyze membership to different structures of individual star.

B.1. Velocity Comparison

For the common 48 stars that have reported proper motions and radial velocities from both data sets, we analyze the data consistency for each star. We first calculate the combined uncertainty for each star’s velocity data as the quadratic sum of uncertainties from both data sets (eg: $\sigma_x = \sqrt{\sigma_{x,curr}^2 + \sigma_{x,F22}^2}$), where $\sigma_{x,curr}$ is the uncertainty in x direction in our data set while $\sigma_{x,F22}$ is the uncertainty in von Felleberg’s data set). Velocity data are considered to be inconsistent with one

another if $|\Delta v_x| = |v_{x,curr} - v_{x,F22}| > 3\sigma_x$. The comparison of v_x , v_y , and v_z for each star is shown in Table 9. We compare velocities (km s⁻¹) rather than direct measurements of proper motion (mas yr⁻¹) since von Fellenberg et al. (2022) does not report the distance used for conversion. Even though Δv_x and Δv_y are usually small compared to Δv_z , the uncertainties on the proper motions are significantly smaller than that of the radial velocities. Thus, $\sim 73\%$ of stars classified as having inconsistent velocity data in either x or y direction while only one star, namely S4-169, has inconsistent v_z with opposite signs.

To assess whether there are differences in the astrometric reference frames of the two papers, we analyze the mean proper motion offsets. We calculate the weighted mean velocity and error on weighted mean velocity to find that $\langle \Delta v_x \rangle = 2.25 \pm 0.50$ km s⁻¹, $\langle \Delta v_y \rangle = 4.31 \pm 0.49$ km s⁻¹. To search for scale or rotation differences in the reference frames, we also convert the proper motions into their projected radial and tangential components, v_r and v_t . Following the same procedures we find that $\langle \Delta v_r \rangle = -1.94 \pm 0.50$ km s⁻¹ and $\langle \Delta v_t \rangle = 3.23 \pm 0.48$ km s⁻¹. This suggests there are linear, scale, and rotation differences in the reference frames (Figure 19). Figure 20 shows a map on the sky of the orientation and significance of the proper motion difference vectors. We find that there is not an obvious relation between σ and stars’ angular position in the sky, but stars within the inner 5 $''$ (orange line) are more likely to have inconsistent proper motion data. The proper motion measurements in von Fellenberg et al. (2022) come from several previous papers and the astrometric reference frame is likely not consistent between them. The inconsistencies we find may originate from systematic reference frame errors. Sakai et al. (2019) reports typical reference frame errors in proper motion of ~ 1.2 km s⁻¹ and rotation of $\sim 2^\circ$ per decade, which largely explain the discrepancies above.

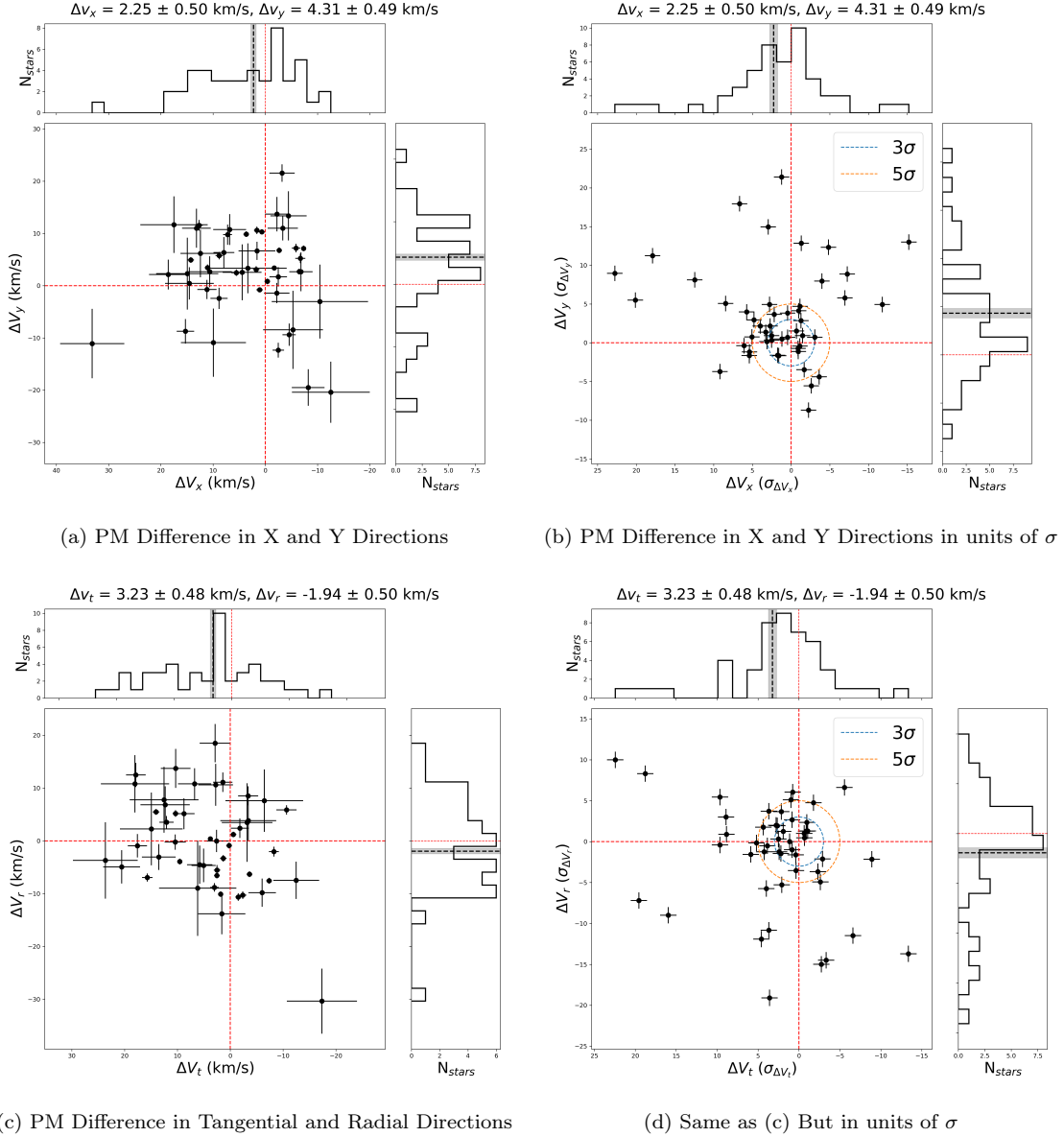


Figure 19. Comparison of proper motions from the current work with that of [von Fellenberg et al. \(2022\)](#). The upper left panel shows differences in x and y directions, plotted in unit of km s^{-1} . The upper right panel shows the same differences, plotted in units of star’s corresponding σ . Similar comparisons in the radial and tangential directions are shown in the lower two panels. For the two σ -plots (right), we also draw 2 circles showing 3σ (blue) and 5σ (orange) regions to illustrate our criterion of consistency.

Table 9. Comparison of Star Velocity

Name	$v_{x,curr}$	$v_{x,F22}$	$\Delta v_x/\sigma v_x$	$v_{y,curr}$	$v_{y,F22}$	$\Delta v_y/\sigma v_y$	$v_{z,curr}$	$v_{z,F22}$	$\Delta v_z/\sigma v_z$
	(km s^{-1})	(km s^{-1})		(km s^{-1})	(km s^{-1})		(km s^{-1})	(km s^{-1})	
S0-11	-133.27	-140.50	8.46	-100.43	-110.20	5.06	-21.50	-41.60	0.30
S0-9	339.41	345.30	-7.25	-203.50	-210.70	8.87	95.30	156.70	-1.13
S0-31	240.50	247.20	-6.95	39.64	34.40	5.79	-119.60	-262.70	1.42

Table 9 continued

Table 9 (continued)

Name	$v_{x,curr}$	$v_{x,F22}$	$\Delta v_x/\sigma v_x$	$v_{y,curr}$	$v_{y,F22}$	$\Delta v_y/\sigma v_y$	$v_{z,curr}$	$v_{z,F22}$	$\Delta v_z/\sigma v_z$
	(km s ⁻¹)	(km s ⁻¹)		(km s ⁻¹)	(km s ⁻¹)		(km s ⁻¹)	(km s ⁻¹)	
S0-14	92.50	94.20	-3.98	-55.50	-58.90	7.96	-31.50	-57.00	1.14
S1-33	-5.66	-11.20	5.74	195.19	192.70	3.97	26.20	3.20	1.28
S1-22	311.47	310.80	1.22	-123.08	-133.40	21.40	-229.70	-293.60	0.63
S1-24	101.56	97.90	6.65	-248.42	-258.30	17.96	125.20	153.50	-0.68
S2-4	307.32	313.80	-11.78	105.71	103.00	4.93	217.60	208.20	0.33
S2-6	303.55	306.20	-4.83	79.28	72.50	12.33	152.40	179.90	-1.02
S2-50	74.75	78.10	-1.15	77.02	66.00	4.69	-135.20	-52.10	-0.71
S2-17	346.96	354.30	-15.22	-7.55	-14.70	13.00	56.90	64.50	-0.17
S2-19	-308.83	-319.90	20.12	29.45	26.00	5.50	54.50	41.20	0.50
S2-58	-30.58	-28.10	-2.26	242.76	255.10	-8.70	77.30	61.90	0.44
S2-74	-327.33	-341.60	22.78	41.53	36.60	8.96	43.80	35.20	0.29
S3-3	138.94	134.50	1.19	155.17	152.60	0.48	23.30	45.40	-0.51
S3-96	-0.76	-33.90	5.40	196.32	207.40	-1.67	-3.00	41.80	-0.88
S3-19	302.03	287.50	3.12	-66.45	-66.90	0.15	-84.40	-122.50	0.63
S3-26	226.15	224.40	2.79	55.50	52.40	4.95	84.40	60.10	0.64
S3-30	-30.20	-31.30	1.75	151.02	151.80	-1.62	6.50	31.90	-0.45
S3-190	-105.71	-118.40	17.90	-115.53	-127.10	11.24	-262.50	-249.80	-0.14
S3-331	225.02	227.50	-1.48	159.70	158.00	0.91	-165.60	-154.30	-0.24
S3-374	-10.57	-19.40	12.45	-165.74	-171.50	8.12	33.80	17.80	0.60
S4-71	3.02	3.40	-0.69	-173.67	-174.50	1.51	63.50	63.60	-0.00
S4-169	-95.52	-106.70	6.08	149.88	150.60	-0.39	157.70	-84.20	3.60
S4-262	-52.86	-48.30	-3.62	-205.38	-196.00	-4.40	41.00	39.90	0.02
S4-364	258.99	243.70	9.19	-112.13	-103.40	-3.73	-109.30	-150.90	0.84
S5-237	-49.46	-59.40	1.60	233.70	244.60	-1.67	42.00	34.50	0.31
S5-183	-170.65	-179.50	5.38	-80.42	-78.00	-1.19	-146.30	-187.00	0.96
S5-191	-57.39	-55.20	-0.90	-142.71	-141.30	-0.73	127.00	107.00	0.29
S6-89	108.73	98.10	2.52	-243.52	-246.20	0.91	-128.20	-128.50	0.00
S6-96	-30.20	-24.90	-0.93	274.85	283.30	-1.13	21.80	-20.10	0.64
S6-81	-101.56	-104.90	0.45	191.04	187.70	0.70	-21.80	9.90	-1.06
S6-63	220.86	227.70	-3.06	62.67	60.00	0.72	143.50	140.80	0.06
S7-30	-113.64	-101.10	-1.68	-148.00	-127.60	-3.48	-35.40	-27.40	-0.13
S7-10	-168.76	-176.70	3.98	-86.84	-93.20	2.16	-67.70	-143.50	2.11
S7-216	83.06	87.50	-1.28	215.58	202.20	2.85	128.10	71.00	1.42
S7-236	-95.90	-92.70	-1.32	-152.53	-174.10	12.85	78.00	-90.60	1.72
S8-4	-15.86	-30.80	2.51	134.41	132.10	0.33	-118.80	-209.00	1.58
S8-196	43.04	30.60	3.27	-58.52	-64.70	1.36	197.20	208.90	-0.17
S9-143	22.28	24.50	-0.98	-107.60	-121.30	4.13	44.10	190.80	-1.31
S10-50	-29.45	-19.00	-1.13	-152.53	-149.50	-0.43	69.90	88.50	-0.21
S10-4	-72.87	-79.70	2.17	42.66	31.90	3.65	-188.90	-278.30	2.02
S10-32	102.69	110.90	-2.61	131.01	150.50	-5.56	146.30	214.80	-0.92
S10-48	72.49	55.00	2.71	30.58	18.90	2.16	-285.30	-208.10	-1.16
S11-21	-68.71	-81.90	4.79	-92.50	-103.50	2.94	-81.40	-199.40	2.34
IRS13E1	-137.80	-139.40	0.45	-100.43	-107.10	3.83	-10.40	34.90	-1.51
IRS16CC	-57.01	-75.60	5.06	246.54	244.40	0.75	253.20	246.20	0.22
IRS33N	137.43	135.80	2.96	-225.39	-236.00	14.96	23.00	39.00	-0.35

Even though the differences between each proper motion component are small in amplitude, we believe this inconsistency may lead to different membership probabilities to dynamical structures for stars (Appendix B.3). This emphasizes the importance of using position and proper motion data extracted from a common data set. Additionally, the v_z differences are large in amplitude; but small in statistical significance. This will also impact the disk membership probabilities for individual stars, especially when $\Delta v_z \gtrsim 90$ km/s. The fraction of stars with discrepant velocities is fairly consistent across the kinematic sub-structures detected in this paper and those from vF22 and does not depend on radius. This is likely due to the fact that v_x and v_y discrepancies dominate at small radii while large differences and uncertainties in v_z dominate at large radii.

B.2. Significance and Structure Comparison

In von Fellenberg et al. (2022), they detect structures through an over-density of angular momentum vectors (their §3), which is similar to what we use in §4. However, when quantifying the significance of each structure, they use a different definition (vF22 Eq 6) compared to ours (Eq 10). The main difference is that von Fellenberg et al. (2022) uses mean values of density while we use peak density in the (i, Ω) map (for a detailed comparison, see their Appendix C).

They report (i, Ω) ³ locations of 5 structures in their Table 1. However, there is no reported uncertainty in the location of each structure. To calculate the significance of their structures using our definition, we assign an uncertainty of 20° for the position of each structure (eg: CW1 will have $i = 124.5 \pm 20$, $\Omega = 106.9 \pm 20$). We choose 20° because this is the largest uncertainty our structures have and this covers regions of structures shown in von Fellenberg et al. (2022, Figure 7). Then we search for the peak density of the normal vector in the assigned region of each structure and calculate the corresponding significance shown in Table 10.

We find that CW1 and F3 have comparable significance with our Disk1 and Plane2 while the significance of other structures do not exceed our criterion of 6σ . The conflicting results are likely due to sample differences (FOV size, stars included, reference frame, velocity measurement differences), different definitions of significance, and perhaps our choice of uniform-acceleration prior (c.f. §3.1). For example, we do not detect the CW2 feature because for the total 13 CW2 stars, only 6 have completeness information and are

thus included in our sample. The locations of CW1 and F3 are within the uncertainties of our Disk1 and Plane2, which supports the definitive existence of these two structures. The eccentricity distributions within these two structures are also similar. For Disk1, we report the $\langle e \rangle = 0.39 \pm 0.16$ (§5.2.1) while they find CW1 has a median eccentricity of 0.5, which is consistent within the uncertainty. For Plane2, we calculate that it has $\langle e \rangle = 0.68 \pm 0.07$ while they report F3 has a median eccentricity of 0.7.

We also notice that we detect an asymmetry in Plane2, which is not detected by vF22 in their F3 structure analysis. We note that vF22 has incomplete azimuthal coverage for stars outside of $10''$, where as both papers have relatively uniform coverage inside of $10''$. This, combined with variable completeness and reddening, which is not modeled in vF22, may explain why we detect asymmetry while vF22 does not.

Table 10. Comparison of Significance

Structure	N_{stars}	$i(^{\circ})$	$\Omega(^{\circ})$	σ_i^a	σ_{Ω}^a	Significance
CW1	33	124.5	106.9	20	20	12.40
CW2	13	145.6	156.7	20	20	0.64
CCW(F1)	33	60.0	227.0	20	20	2.04
F2	37	106.0	180.0	20	20	3.31
F3	36	101.5	224.2	20	20	5.99
Disk1	18	124.0	94.0	15	17	12.40
Plane2	10	90.0	245.0	20	19	6.45

^aFor 5 structures reported in von Fellenberg et al. (2022), we assign an uncertainty of 20° on their locations, which is similar to our data.

B.3. Membership Comparison

We compare the membership for 18 stars that we think belong to Disk1 and 10 stars to Plane2 to the structures assigned to these stars in von Fellenberg et al. (2022). The results are shown in Table 11 and Table 12, where 'Curr P_{Disk1} ' is the probability membership for a star being on Disk1 reported in our paper and 'F22 Structure' is the structure assigned to this star in von Fellenberg et al. (2022). We classify a star as belonging to a structure if its membership probability exceeds $P_{threshold} = 0.2$. Even though von Fellenberg et al. (2022) reports two CW features, only CW1 is consistent with (i, Ω) of our Disk1. There are 13 out of 18 stars that both of us agree to be on the CW disk, which enhances our conclusion of the same structure.

For Plane2 structure, we choose to compare all potential Plane2 stars shown in Table 6 to better match

³ von Fellenberg et al. (2022) reports (θ, ϕ) and we convert to (i, Ω) for direct comparison.

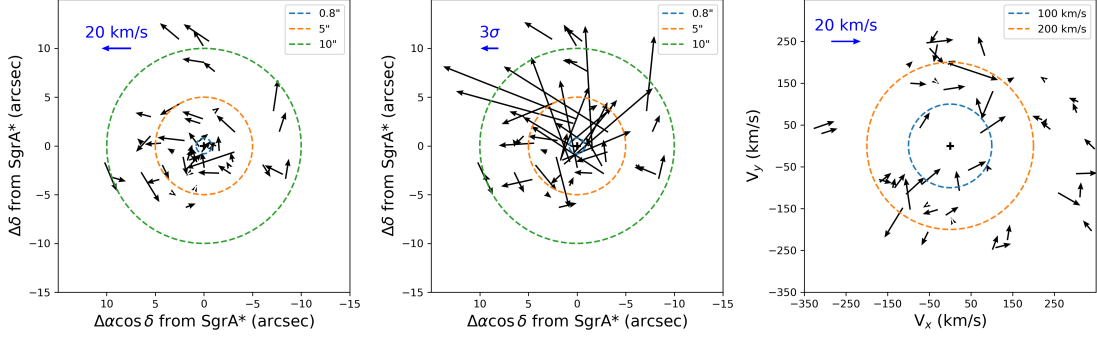


Figure 20. A sky map showing the orientation and significance of the proper motion differences for the 45 common stars with reported radial velocities in this work and in (von Fellenberg et al. 2022). The arrow indicates the proper motion difference in units of km s^{-1} (left) and in units of each star’s corresponding σ (middle). The left and middle plots have (x, y) position of each star from our data set; the three circles show $0.8''$ (blue), $5''$ (orange), and $10''$ (green) regions from SgrA*. The right figure plots the differential proper motion vectors over (v_x, v_y) from our data set; the two circles represent contours of 100 km s^{-1} (blue) and 200 km s^{-1} (orange). The upper right blue arrow is plotted as reference, indicating a length of 20 km/s (left and right) and 3σ (middle). Notice that for illustration purposes, arrows in the right figure do not have the same scale as the x and y axes.

the data used by Fellenberg where they do not exclude stars without completeness. From Table 12, there are only 6 out of 17 stars that are belonging to Plane2 and F3. We identify one particular star, S0-31, which they report belonging to CCW disk while we think it is on Plane2. This might be caused by the inconsistent v_x and v_y for this star (see Table 9). These comparisons show that Plane2 and F3 differ in their exact memberships, but other properties such as the orientation and eccentricity distribution support the conclusion that these are similar structure.

As we discussed above, inconsistent velocities may lead to differences in membership and conflicting conclusions for individual stars (Appendix B.1). For the total 47 common stars that have reported structures in both paper, we identify 11 conflicted stars, as shown in Table 13. Through checking Table 9, we find that 8 of them have at least one inconsistent proper motion data. For the remaining 3 stars, S0-3 and S0-8 have full orbital solutions while S3-3 has consistent $v_x, v_y,$ and v_z . We also identify one particular star, S10-32, which is reported to be a CW1 star. S10-32 has $P_{\text{Disk1}} = 0.18$, which is slightly lower than our threshold probability of 0.2 and thus we classify it as an off-disk star. However, we think these two classifications are consistent given this tiny difference in probability.

In summary, through comparisons and analysis of velocity data, significance calculation, disk properties, and disk membership, we think that our Disk1 is consistent with CW1 structure reported in von Fellenberg’s work. Plane2 has $\sim 35\%$ members classified as belonging to F3, but the difference in Ω between these two structures is greater than $1 - \sigma$ (34° compared to 27.6°). Thus, we

think these two structures may be the same; but further analysis is needed to confirm. For the other 3 structures (CW2, CCW, and F2), we do not find these features because they do not exceed our 6σ criterion (Appendix B.2).

Table 11. Comparison of Disk1 Star Membership

Name	Curr P_{Disk1}	F22 Structure
S1-3	0.49	CW1
S0-15	0.76	CW1
S1-2	0.50	CW1
S1-22	0.54	CW1
S1-19	0.43	-
IRS16CC	0.25	-
S2-4	0.22	CW1
S2-6	0.50	CW1
S2-17	0.37	CW1
S2-21	0.50	CW1
S2-19	0.24	CW1
S2-74	0.50	CW1
S3-19	0.36	CW1
S3-26	0.24	CW1
S3-190	0.35	CW1/F2
S4-169	0.40	CW2/F2
S4-314	0.47	-
S6-63	0.27	CW2

Table 12. Comparison of Plane2 Star Membership

Name	Curr P_{Plane2}	F22 Structure
S0-31	0.30	CCW(F1)
IRS 16NW	0.38	-
IRS 13E1	0.50	-
IRS 13E3	0.34	-
S4-258	0.40	CCW(F1)
S5-34	0.36	F3
S5-106	0.34	-
S5-236	0.71	F3
S9-114	0.52	F3
S9-221	0.77	-
S10-185	0.73	-
S10-238	0.78	-
S12-5	1.00	-
S13-3	0.27	-
S0-16	0.42	-
S3-26	0.24	F3/CW1
S8-196	0.22	F3

Table 13. Conflicted Stars

Name	P_{Disk1}	P_{Plane2}	$P_{\text{Non-disk}}$	F22 Structure
S0-8	0.00	0.00	1.00	CW1
S0-3	0.00	0.00	1.00	F3
S0-11	0.00	0.05	0.95	CCW(F1)/F3
S0-9	0.00	0.00	1.00	CW1
S0-31	0.00	0.30	0.70	CCW(F1)
S2-50	0.00	0.00	1.00	F3
S3-3	0.00	0.00	1.00	F3
S4-169	0.40	0.00	0.60	CW2/F2
S6-63	0.27	0.00	0.73	CW2
S7-10	0.16	0.03	0.81	CW2/F3
S9-143	0.01	0.00	0.99	F3
S10-32 ^a	0.18	0.00	0.82	CW1

^aSee Appendix B.3 for a detailed discussion on S10-32.

C. FULL KEPLERIAN ORBIT ANALYSIS

In Figure Figures 21 to 26, we plot the full Keplerian orbit fit for the other 6 orbit stars in our sample: S0-1, S0-3, S0-8, S0-15, S0-19, S1-2, in the same format as in Figure 5.

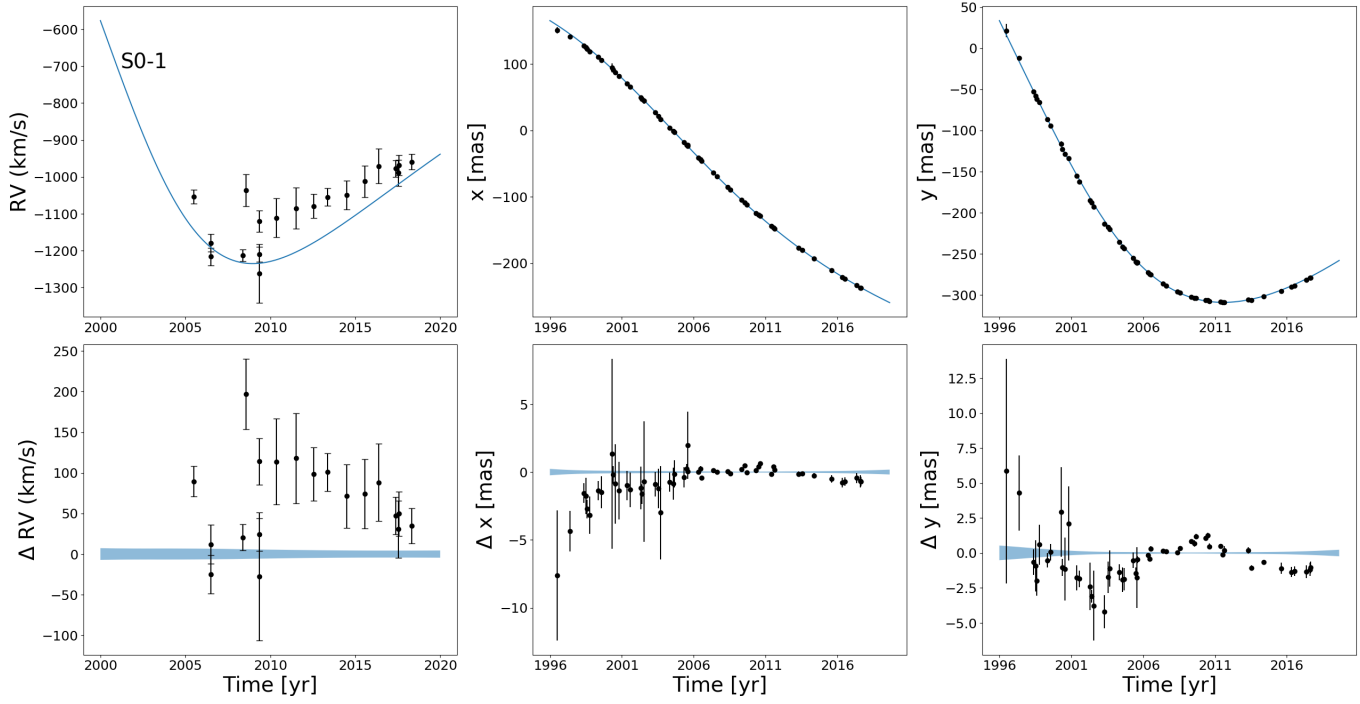


Figure 21. Examples of full Keplerian orbit analysis for S0-1.

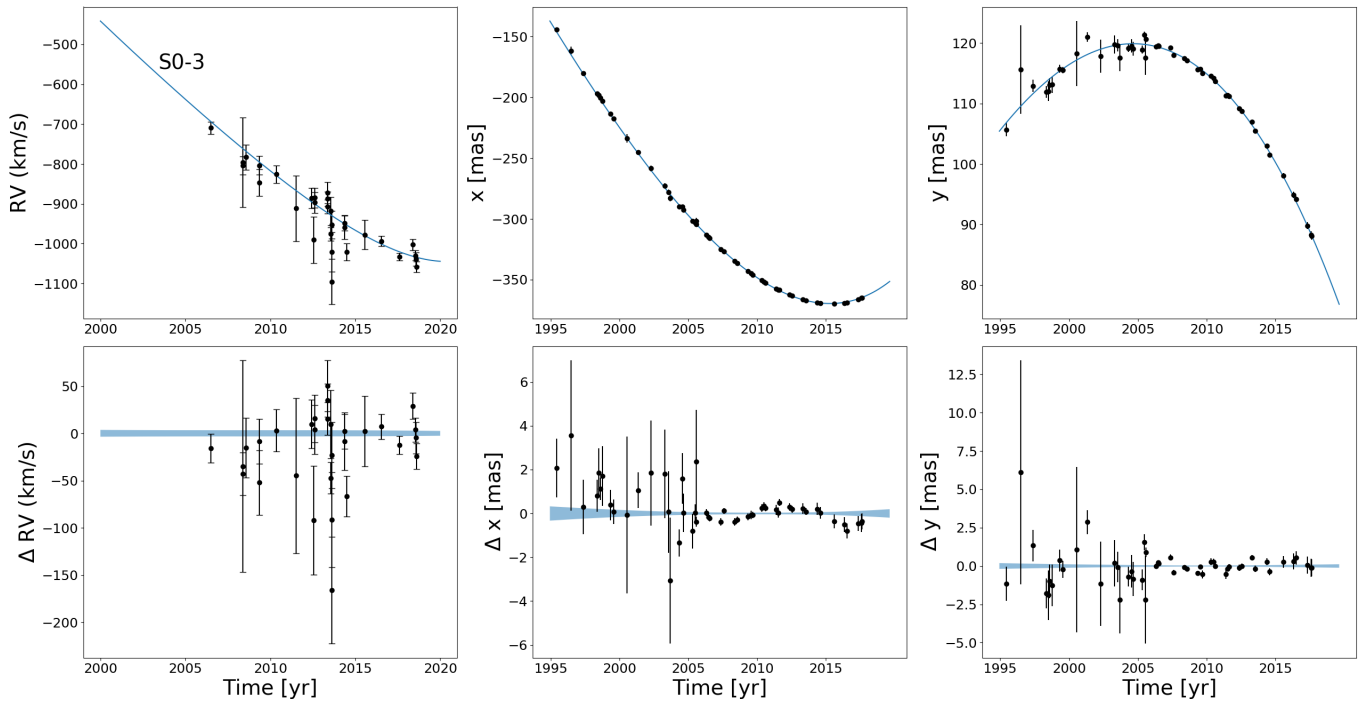


Figure 22. Examples of full Keplerian orbit analysis for S0-3.

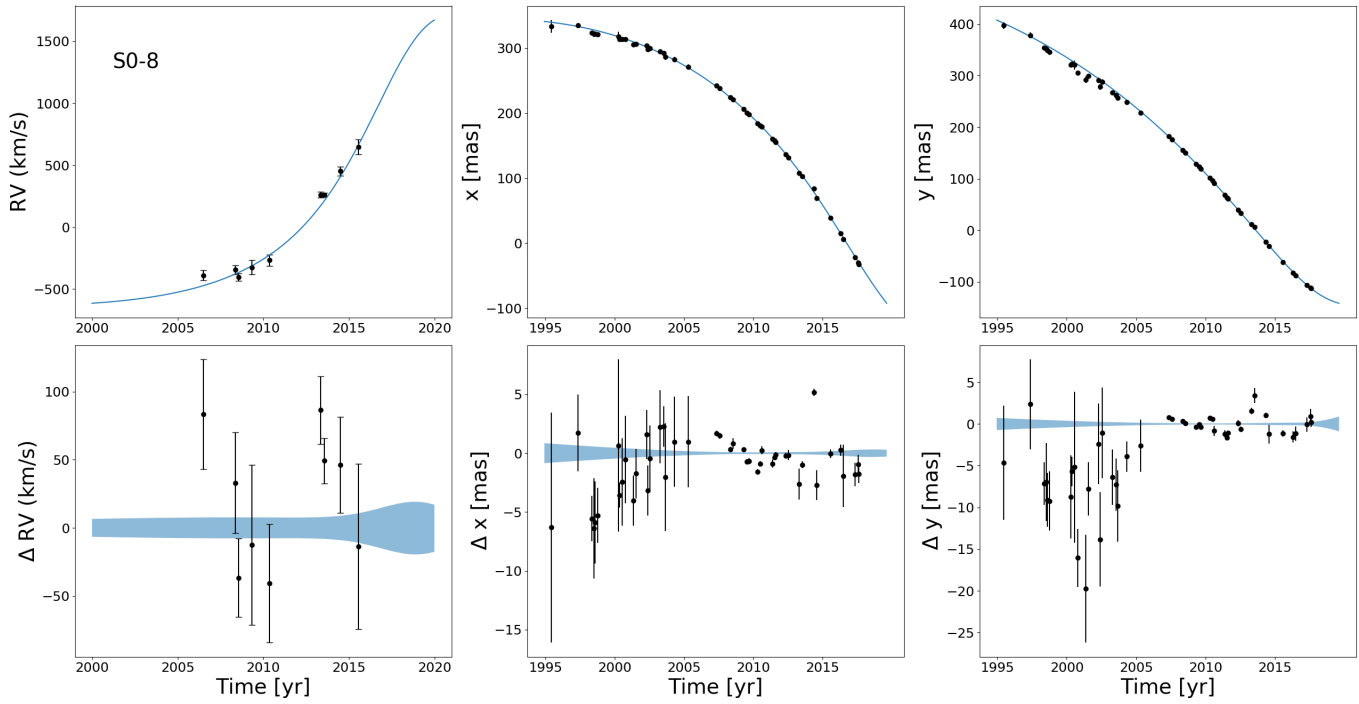


Figure 23. Examples of full Keplerian orbit analysis for S0-8.

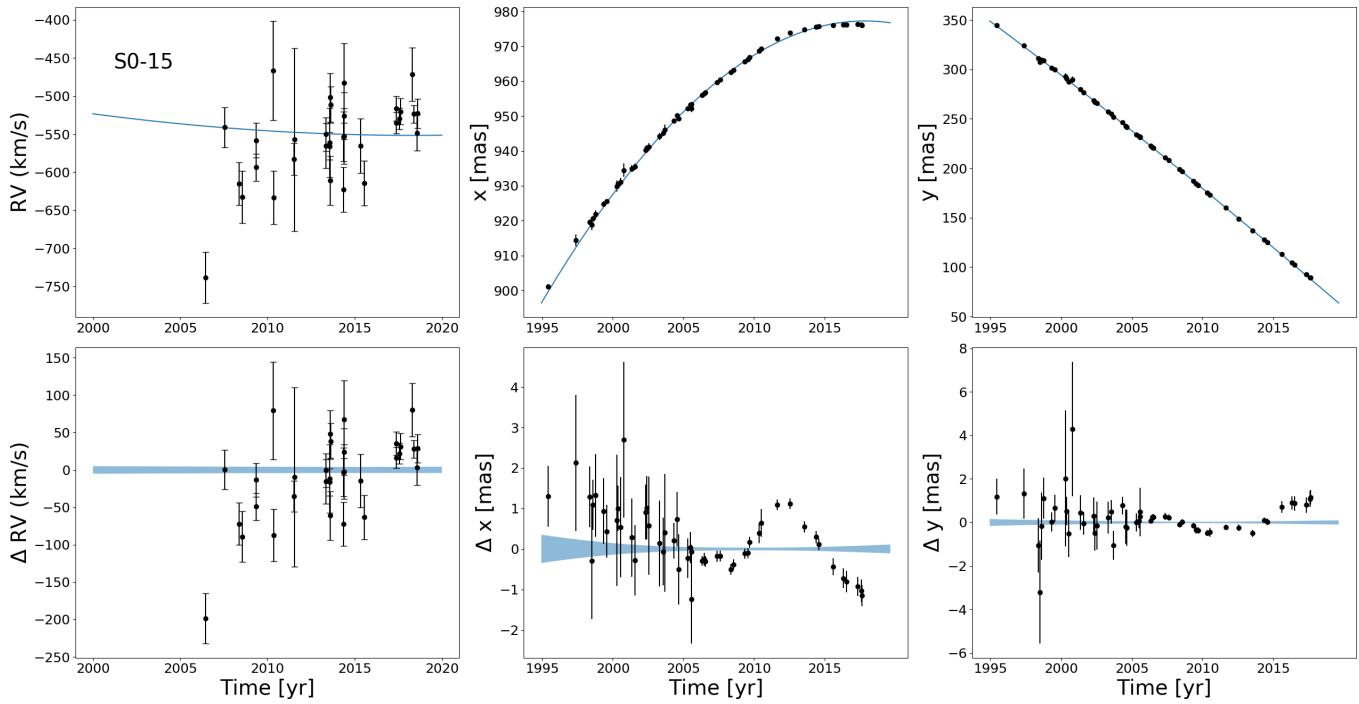


Figure 24. Examples of full Keplerian orbit analysis for S0-15.

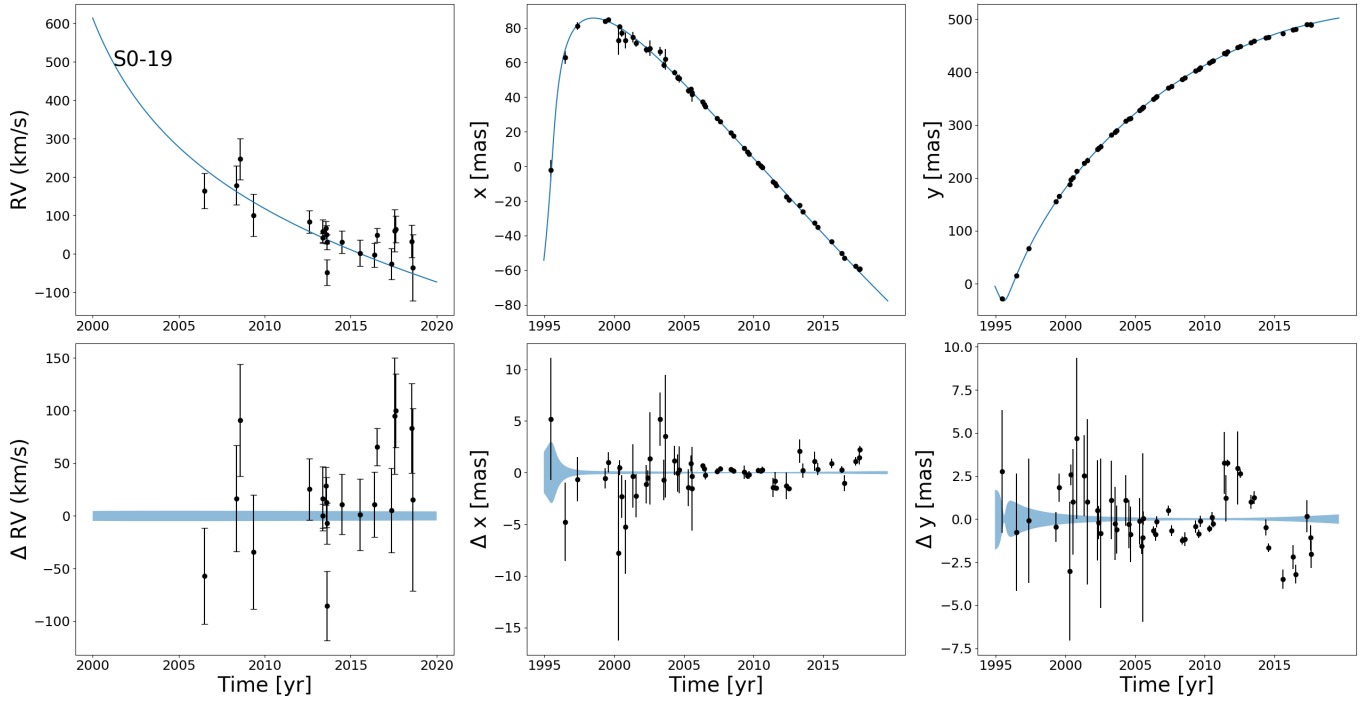


Figure 25. Examples of full Keplerian orbit analysis for S0-19.

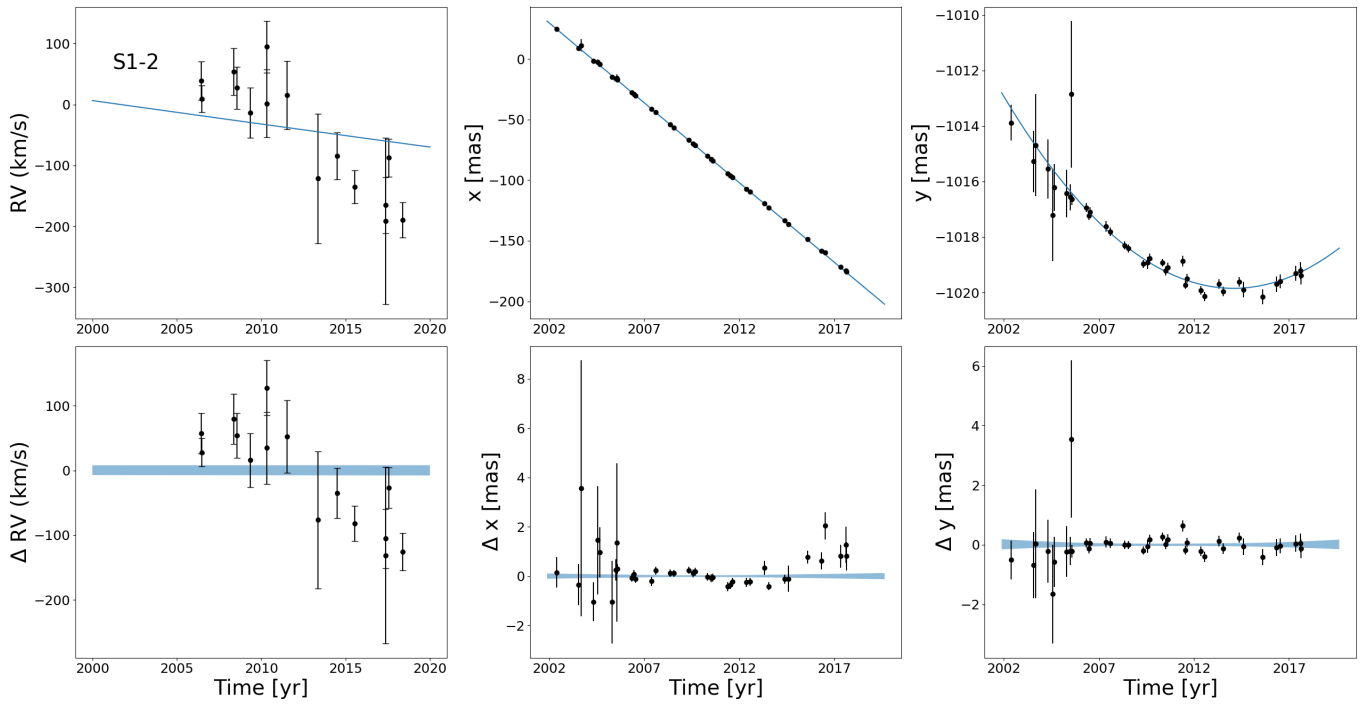


Figure 26. Examples of full Keplerian orbit analysis for S1-2.

REFERENCES

- Abarca, D., Sądowski, A., & Sironi, L. 2014, *Monthly Notices of the Royal Astronomical Society*, 440, 1125.
<https://doi.org/10.1093/mnras/stu244>
- Alexander, T. 2007, arXiv e-prints, arXiv:0708.0688
- Astropy Collaboration, Robitaille, T. P., Tollerud, E. J., et al. 2013, *A&A*, 558, A33
- Bartko, H., Martins, F., Fritz, T. K., et al. 2009, *ApJ*, 697, 1741
- Bartko, H., Martins, F., Trippe, S., et al. 2010, *ApJ*, 708, 834
- Bohlin, R. C., Mészáros, S., Fleming, S. W., et al. 2017, *AJ*, 153, 234
- Bowler, B. P., Blunt, S. C., & Nielsen, E. L. 2020, *AJ*, 159, 63
- Ciurlo, A., Campbell, R. D., Morris, M. R., et al. 2020, *Nature*, 577, 337
- Do, T., Ghez, A. M., Morris, M. R., et al. 2009, *ApJ*, 703, 1323
- Do, T., Kerzendorf, W., Konopacky, Q., et al. 2018, *ApJL*, 855, L5
- Do, T., Lu, J. R., Ghez, A. M., et al. 2013, *ApJ*, 764, 154
- Do, T., Hees, A., Ghez, A., et al. 2019, arXiv e-prints, arXiv:1907.10731
- Eckart, A., Mužić, K., Yazici, S., et al. 2013, *A&A*, 551, A18
- Eric, J., Travis, O., Pearu, P., & others. 2001–, "http://www.scipy.org/"
- Eylen, V. V., Albrecht, S., Huang, X., et al. 2019, *The Astronomical Journal*, 157, 61.
<https://doi.org/10.3847/2F1538-3881%2Faaaf22f>
- Feldmeier-Krause, A., Neumayer, N., Schödel, R., et al. 2015, *A&A*, 584, A2
- Feroz, F., Hobson, M. P., & Bridges, M. 2009, *MNRAS*, 398, 1601
- Ferrarese, L., Côté, P., Dalla Bontà, E., et al. 2006, *ApJL*, 644, L21
- Fritz, T., Gillessen, S., Trippe, S., et al. 2010, *MNRAS*, 401, 1177
- Genzel, R., Pichon, C., Eckart, A., Gerhard, O. E., & Ott, T. 2000, *MNRAS*, 317, 348
- Genzel, R., Schödel, R., Ott, T., et al. 2003, *ApJ*, 594, 812
- Gerhard, O. 2001, *ApJL*, 546, L39
- Ghez, A. M., Salim, S., Hornstein, S. D., et al. 2005, *ApJ*, 620, 744
- Gillessen, S., Eisenhauer, F., Trippe, S., et al. 2009, *ApJ*, 692, 1075
- Gillessen, S., Genzel, R., Fritz, T. K., et al. 2013, *ApJ*, 774, 44
- Gillessen, S., Plewa, P. M., Widmann, F., et al. 2019, *The Astrophysical Journal*, 871, 126.
<https://doi.org/10.3847/1538-4357/aaaf4f8>
- Goodman, J. 2003, *MNRAS*, 339, 937
- Graham, A. W., & Spitler, L. R. 2009, *MNRAS*, 397, 2148
- Higson, E., Handley, W., Hobson, M., & Lasenby, A. 2019, *Stat Comput*, 29, 891
- Hogg, D. W., Myers, A. D., & Bovy, J. 2010, *ApJ*, 725, 2166
- Hopman, C., & Alexander, T. 2006, *ApJ*, 645, 1152
- Hosek, Jr., M. W., Lu, J. R., Lam, C. Y., et al. 2020, *AJ*, 160, 143
- Hunter, J. D. 2007, *Computing in Science and Engineering*, 9, 90
- Jia, S., Lu, J. R., Sakai, S., et al. 2019, *ApJ*, 873, 9
- Kerzendorf, W., & Do, T. 2015, *Starkit: First Real Release, v0.2*, Zenodo, doi:10.5281/zenodo.28016
- Kocsis, B., & Tremaine, S. 2011, *Monthly Notices of the Royal Astronomical Society*, 412, 187.
<https://doi.org/10.1111%2Fj.1365-2966.2010.17897.x>
- Kolykhalov, P. I., & Syunyaev, R. A. 1980, *Soviet Astronomy Letters*, 6, 357
- Kormendy, J., & Ho, L. C. 2013, *ARA&A*, 51, 511
- Larkin, J., Barczys, M., Krabbe, A., et al. 2006, in *Society of Photo-Optical Instrumentation Engineers (SPIE) Conference Series*, Vol. 6269, Society of Photo-Optical Instrumentation Engineers (SPIE) Conference Series, ed. I. S. McLean & M. Iye, 62691A
- Levin, Y. 2007, *MNRAS*, 374, 515
- Levin, Y. 2022, *Resonant friction on discs in galactic nuclei*, arXiv, doi:10.48550/ARXIV.2211.12754.
<https://arxiv.org/abs/2211.12754>
- Levin, Y., & Beloborodov, A. M. 2003, *ApJL*, 590, L33
- Lin, D. N. C., & Pringle, J. E. 1987, *MNRAS*, 225, 607
- Lockhart, K. E., Do, T., Larkin, J. E., et al. 2019, *The Astronomical Journal*, 157, 75.
<https://doi.org/10.3847/2F1538-3881%2Faaaf64e>
- Lu, J. R., Do, T., Ghez, A. M., et al. 2013, *ApJ*, 764, 155
- Lu, J. R., Ghez, A. M., Hornstein, S. D., et al. 2009, *ApJ*, 690, 1463
- Lyke, J., Do, T., Boehle, A., et al. 2017, *OSIRIS Toolbox: OH-Suppressing InfraRed Imaging Spectrograph pipeline*, Astrophysics Source Code Library, record ascl:1710.021, ascl:1710.021
- Maillard, J. P., Paumard, T., Stolovy, S. R., & Rigaut, F. 2004, *A&A*, 423, 155
- Martins, F., Genzel, R., Hillier, D. J., et al. 2007, *A&A*, 468, 233

- Mignard, F., & Klioner, S. 2018, in IAU Symposium, Vol. 330, *Astrometry and Astrophysics in the Gaia Sky*, ed. A. Recio-Blanco, P. de Laverny, A. G. A. Brown, & T. Prusti, 71–74
- Morris, M., & Serabyn, E. 1996, *ARA&A*, 34, 645
- Mužić, K., Schödel, R., Eckart, A., Meyer, L., & Zensus, A. 2008, *A&A*, 482, 173.
<https://doi.org/10.1051%2F0004-6361%3A20078352>
- Naoz, S., Ghez, A. M., Hees, A., et al. 2018, *ApJL*, 853, L24
- Nayakshin, S. 2006, *MNRAS*, 372, 143
- Nayakshin, S., & Sunyaev, R. 2005, *MNRAS*, 364, L23
- Nogueras-Lara, F., Gallego-Calvente, A. T., Dong, H., et al. 2018, *A&A*, 610, A83
- O’Neil, K. K., Martinez, G. D., Hees, A., et al. 2019, *The Astronomical Journal*, 158, 4
- Paumard, T., Genzel, R., Martins, F., et al. 2006, *ApJ*, 643, 1011
- Phifer, K., Do, T., Meyer, L., et al. 2013, *ApJL*, 773, L13
- Raghavan, D., McAlister, H. A., Henry, T. J., et al. 2010, *The Astrophysical Journal Supplement Series*, 190, 1.
<https://doi.org/10.1088%2F0067-0049%2F190%2F1%2F1>
- Rauch, K. P., & Tremaine, S. 1996, *New Astronomy*, 1, 149.
[http://dx.doi.org/10.1016/S1384-1076\(96\)00012-7](http://dx.doi.org/10.1016/S1384-1076(96)00012-7)
- Sakai, S., Lu, J. R., Ghez, A., et al. 2019, arXiv e-prints, arXiv:1901.08685
- Salpeter, E. E. 1955, *ApJ*, 121, 161
- Sana, H., de Mink, S. E., de Koter, A., et al. 2012, *Science*, 337, 444. <https://doi.org/10.1126%2Fscience.1223344>
- Sanders, R. H. 1998, *MNRAS*, 294, 35
- Schödel, R., Eckart, A., Iserlohe, C., Genzel, R., & Ott, T. 2005, *ApJL*, 625, L111
- Schödel, R., Merritt, D., & Eckart, A. 2009, *A&A*, 502, 91
- Schödel, R., Najarro, F., Muzic, K., & Eckart, A. 2010, *Astronomy and Astrophysics*, 511, A18. <https://www.aanda.org/articles/aa/pdf/2010/03/aa13183-09.pdf>
- Schödel, R., Ott, T., Genzel, R., et al. 2003, *ApJ*, 596, 1015
- Shcherbakov, R. V. 2014, *ApJ*, 783, 31
- Skilling, J. 2004, in *American Institute of Physics Conference Series*, Vol. 735, *American Institute of Physics Conference Series*, ed. R. Fischer, R. Preuss, & U. V. Toussaint, 395–405
- Skilling, J. 2006, *Bayesian Anal.*, 1, 833.
<https://doi.org/10.1214/06-BA127>
- Speagle, J. S. 2020, *MNRAS*, 493, 3132
- Stephan, A. P., Naoz, S., Ghez, A. M., et al. 2016, *Monthly Notices of the Royal Astronomical Society*, 460, 3494.
<https://doi.org/10.1093%2Fmnras%2Fstw1220>
- Støstad, M., Do, T., Murray, N., et al. 2015, *ApJ*, 808, 106
- Trippe, S., Gillessen, S., Gerhard, O. E., et al. 2008, *A&A*, 492, 419
- Tsuboi, M., Tsutsumi, T., Miyazaki, A., Miyawaki, R., & Miyoshi, M. 2022, *Publications of the Astronomical Society of Japan*, 74, 738.
<https://doi.org/10.1093%2Fpasj%2Fpsac031>
- Valencia-S., M., Eckart, A., Zajaček, M., et al. 2015, *ApJ*, 800, 125
- Vollmer, B., & Duschl, W. J. 2001, *A&A*, 377, 1016
- von Fellenberg, S. D., Gillessen, S., Stadler, J., et al. 2022, *The Astrophysical Journal Letters*, 932, L6.
<https://doi.org/10.3847%2F2041-8213%2Ffac68ef>
- Wang, Q. D., Li, J., Russell, C. M. P., & Cuadra, J. 2019, *Monthly Notices of the Royal Astronomical Society*, 492, 2481. <https://doi.org/10.1093%2Fmnras%2Fstz3624>
- Witzel, G., Ghez, A. M., Morris, M. R., et al. 2014, *ApJ*, 796, L8
- Witzel, G., Sitarski, B. N., Ghez, A. M., et al. 2017, *The Astrophysical Journal*, 847, 80.
<https://doi.org/10.3847%2F1538-4357%2Faa80ea>
- Wolfgang, A., Rogers, L. A., & Ford, E. B. 2016, *The Astrophysical Journal*, 825, 19. <https://doi.org/10.3847%2F0004-637x%2F825%2F1%2F19>
- Yelda, S., Ghez, A. M., Lu, J. R., et al. 2014, *ApJ*, 783, 131
- Zhu, Z., Li, Z., Ciurlo, A., et al. 2020, arXiv e-prints, arXiv:2003.10311